PERFORMANCE INVESTIGATION
ON PLATE HEAT EXCHANGER
USING NANOFLUID AS WORKING FLUID

LER CHERK YONG

RESEARCH REPORT SUBMITTED
IN PARTIAL FULFILMENT OF THE REQUIREMENTS
FOR THE DEGREE OF MASTER OF ENGINEERING

FACULTY OF ENGINEERING
UNIVERSITY OF MALAYA
KUALA LUMPUR

2011

ABSTRACT

Plate heat exchanger (PHE) is a kind of heat transfer equipment that made up of a pack of thin corrugated metal plate that promote heat transfer between two fluids. Water as the most common heat transfer medium has low thermal conductivity that result in lower overall heat transfer coefficient. With rising interest in fluid with higher thermal conductivity offered by dispersing nanoparticles in base fluid, called "nanofluids", researchers are investigating the advantages of applying this fluid in conventional heat transfer devices. In this study the performance of an existing PHE in oil and gas industry is investigated when the alumina (Al_2O_3) and silicon dioxide (SiO_2) nanofluids of various particle size and volume fraction was introduce as the hot fluid medium. In addition, the advantages of utilizing nanofluids as the heat transfer medium in the PHE design are examined. In this study, it's found that the application of Al_2O_3 with 3% particle volume concentration nanofluids in the existing PHE system resulted the heat transfer rate increased by 1.29% and correspondingly 2.66% of the volumetric flow rate can be reduce to achieve the similar rated heat transfer rate. For SiO_2 nanofluids, it's distinguished that the highest heat transfer rate could be achieved by 1.5% particle volume concentration. In PHE design, the heat transfer area to achieve the rated PHE heat transfer rate of 460kW was reduce by 3.08% to 3.21% depending on the desired NTU when using Al_2O_3 nanofluids of 3% volume fraction. Meanwhile, it's observed that the reduction of heat transfer area is dependent on the nanoparticles size as the nanofluids with 25nm SiO_2 particles require less heat transfer area compare to the nanofluids with 100nm SiO_2 particles.

ABSTRAK

PHE ialah sejenis alat pemidahan haba yang terdiri daripada satu pek plat logam yang nipis dan beralur untuk meningkatkan kadar pemindahan haba antara dua jenis cecair. Air adalah jenis medium yang paling popular bagi tujuan pemidahan haba, tetapi ia hanya mempunyai kekonduksian terma yang rendah. Dengan adanya "bendalir-nano", sejenis bendalir yang mempunyai kekonduksian terma yang tinggi, penyelidik mula menyiasat kelebihan menggunakan bendalir-nano sebagai medium pemindahan haba di alat-alat pemindahan haba yang kini ada. Dalam kajian ini, prestasi PHE yang digunakan dalam sektor petrolium dan gas akan dikaji apabila bendalir-nano diperbuat daripada zarah-zarah nano alumina (Al_2O_3) dan silicon dioksida (SiO_2) digunakan sebagai medium sebelah panas. Tambahan pula, kelebihan daripada menggunakan bendalir-nano pada masa reka bentuk PHE akan diperiksa. Dalam kajian ini, didapati bahawa dengan menggunakan 3% kepekatan zarah Al_2O_3, kadar pemindahan haba dari PHE yang sedia ada meningkat sebanyak 1.29% atau sepadan dengan menggunakan 2.66% lebih rendah kadar aliran isipadu untuk memindahkan haba yang sedia ada. Manakala, untuk SiO_2 bendalir-nano, ia hanya menujukkan peningkatan maksima pada 1.5% kepekatan zarah. Dalam reka bentuk PHE, keluasan pemindah haba yang diperlukan untuk memindahkan 460kW haba telah dikurangkan sebanyak 3.08% hingga 3.21% bergantung kepada NTU yang diinginkan apabila bendalir-nano Al_2O_3 digunakan. Sementara itu, didapati bahawa pengurangan keluasan pemindah haba yang diperlukan juga bergantung kepada saiz zarah yang digunakan. Sebagai contoh, SiO_2 bendalir-nano diperbuat daripada 25 nm saiz zarah memerlukan keluasan yang kurang jika dibandingkan dengan keluasan yang diperlukan oleh SiO_2 bendalir-nano daripada 100 nm saiz zarah.

ACKNOWLEDGEMENTS

I, Ler Cherk Yong would like to take this opportunity to express my gratitude to my project supervisor, Assoc. Prof. Dr. Saidur Rahman for his precious guidance, discussion and encouragement throughout the process of this project.

TABLE OF CONTENTS

LIST OF TABLE

LIST OF FIGURE

NOMENCLATURE

L	Port to port vertical length, m
w	Effective width of plate, m
b	Corrugation depth, m
A_c	Channel flow cross sectional area, m^2
D_e	Equivalent diameter, m
D_{port}	Port diameter, m
β	Chevron angle, degree
ϕ	Surface enlargement factor
δ	Plate thickness, m
N	Number of channel
N	Avogadro number, 6.022×10^{23} mol^{-1}
M	Molecular weight of base fluid, kg/mol
k	Thermal conductivity, W/mK
k_b	Boltzmann constant, 1.38066×10^{-23} J/K
T	Temperature, K
T_0	Temperature at 293K
Re	Reynolds number
Pr	Prandtl number
Nu	Nusselt number
C	Heat capacity rate, W/K
CF	Correction factor
C*	Heat capacity rate ratio
d_p	Particle diameter, m
d_f	Equivalent diameter for base fluid, m
G	Mass velocity, kg/m^2s

g	Gravitational accerelation
f	Friction factor
u_m	Mean fluid velocity, m/s
U	Overall heat transfer coefficient, W/m^2K
q	Heat transfer rate, W
h	Convection heat transfer coefficient, W/m^2K
$\dot{v}$	Volumetric flow rate, m^3/s
$\dot{m}$	Mass flow rate, kg/s
c_p	Specific heat, J/kgK
μ	Dynamic viscosity, Ns/m^2
φ	Particle volume concentration/ volume fraction
ρ	Density, kg/m^3
ρ_{f0}	Density of base fluid calculated at T_0, kg/m^3
V_{port}	Mean port velocity, m/s
NTU	Number of transfer unit
ε	Effectiveness
Δ_{Ptotal}	Total pressure drop, Pa
$\Delta_{Pchannel}$	Channel pressure drop, Pa
Δ_{Pport}	Port pressure drop, Pa
$\Delta_{Pelevation}$	Pressure drop due to elevation change, Pa
$A_{required}$	Required heat transfer area
PP	Pumping power

Subscript

nf	Nanofluids
f	Base fluid
fr	Freezing point
p	Particle
i	Inlet
o	Outlet
hot	Hot fluid side
cold	Cold fluid side
avg	Average
wall	Wall condition
min	Minimum
max	Maximum

LIST OF APPENDICES

1.0 INTRODUCTION

1.1 Background

The advancement of technologies and growth of industrial processes as well as environmental and energy concern have increase the need for heat exchange system that can transfer the heat more efficiently. Apart from improving the equipment design itself, augmenting the thermal performance of the working fluids has increasingly attract the attention of scientists.

The development in heat transfer equipment design has brought to the creation of plate heat exchanger (PHE). PHE is a kind of heat exchanging device which is getting popular in industrial due to its compactness and high heat transfer coefficient together with relatively low hydraulic pressure losses compare to the shell and tube heat exchanger. Thermal plate corrugation designs that promote turbulence and increase the heat transfer surface area are the main features that provide PHE the advantages over traditional shell and tube heat exchanger. Among various corrugation designs, Wang, Sunden and Manglik (2007) commented that chevron or herringbone type design is the most successful design offer by most manufacturers. Therefore, it seems to be the development in the PHE design has almost reached its edge.

With this, working fluids has become an essential element to further improve the heat transfer performance of heat exchanger. Colloidal mixture of particles in nanometer size and traditional heat transfer fluid, usually term as nanofluids is gaining popularity as next generation heat transfer fluid due to its high heat transfer performance. Researches such as Eastman, Choi, Li, Yu and Thompson (2001), Nguyen, Roy, Gauthier and Galanis (2007), Vajjha and Das (2009a) and Wang and Mujumdar (2007) indicated that high thermal conductivity is the essential characteristic of nanofluids and

this feature is strongly dependent on particle volume concentration, size, geometry, material as well as the temperature and type of base fluid. The applications of nanofluids had been reviewed by Saidur, Leong and Mohammad (2011), although the numbers of research related to nanofluids application has been growing but these researches are mostly more towards the nanofluids application in electronics cooling and domestic cooling while only few are related to the industrial heat exchanging system.

In industrial heat exchanging system, an ideal heat exchanger must not only be able to handle a given heat duty, but it must also has energy efficient characteristics and these features may be done by using more efficient drive system and optimum heat exchanger design. Theoretically, nanofluids with its high thermal conductivity feature may help in increasing the heat transfer rate and resulting the reduction of working fluid flow rate supply to the system at a given heat duty. Consequently, energy can be conserved from reducing of pumping power required. However, it must be noted that the increase of thermal conductivity of working fluids itself is not sufficient to rise the performance of heat exchanger, the viscosity and specific heat of the fluids also play an important role in determine the thermal performance of heat exchanging system.

Therefore, in current study, the investigation on application of nanofluids as hot side working fluid in an industrial PHE will be carried out. The thermal and hydrodynamic performance of this PHE will be analyzed.

1.2 Scope of Study

The investigations in this study can be divided into major 2 sections,

1. Application of nanofluids in existing PHE system
2. Application of nanofluids in PHE design

The nanofluids use in this study is water (H_2O) base, with nanoparticles volume concentration ranging from 0% (i.e. fresh water) to 3% at 0.5% step size and it is made of:

1. Alumina (Al_2O_3) particles at 45nm diameter
2. Silicon dioxide (SiO_2) particles at 25nm, 50nm and 100nm diameter.

In each investigation, the effect of nanofluids as the hot fluid medium in PHE is thermally and hydro-dynamically analyzed.

1.3 Objectives

The objectives of this study are:

1. To compare the thermal performance of nanofluids and conventional cooling liquid (i.e. water) in a PHE.
2. To determine the pressure drop in PHE if nanofluids is use as hot side working fluid.
3. To investigate the effect of nanofluids particle volume concentration, size and material in heat transfer enhancement.
4. To determine the potential reduction in heat transfer area required and pressure drop if nanofluids is apply as hot side working fluids in PHE design.

2.0 LITERATURE REVIEW

2.1 Introduction

The literature review for this study can be divided into two main sections. In the first section, the fundamentals for PHE will be briefly discussed. In this section, types of PHE and their basic feature, the typical operating range and construction parameters, the factors that influence the performance, the characteristic of chevron plate and the common correlations for plate heat exchanger performance analysis will be discuss.

Meanwhile, the second section revealed the literature review related to nanofluids. This section summarizes the essence of previous researches regarding basics of nanofluids, the development of nanofluids thermophysical properties evaluation and nanofluids in force convective heat transfer.

2.2 Fundamentals of Plate Heat Exchanger (PHE)

2.2.1 Types of PHE

The common types of PHE are:

1. Gasketed Plate Heat Exchanger (plate and frame heat exchanger)
2. Brazed Plate Heat Exchanger
3. Semi welded and fully welded Plate Heat Exchanger

Gasketed Plate Heat Exchanger (GPHE) is the traditional plate and frame heat exchanger. The major components of this PHE are the pack of thermal plates, gasket, cover plates with ports (act as the supporting end frames with one fix and another moveable), carrying and guiding bars, and tightening bolts. The

thermal plates are made from thin and rectangular pressed metal sheet. The gaskets are placed in between the thermal plates and cover the plates peripherally to form the flow channels. The cover ring or edge gaskets prevent the mixing of fluid between two adjoining channels. The plates and gaskets are clamp in between the fixed and movable cover plates to a prescribe length with the use of tightening bolt. In order to have a perfectly aligned pack of plates, this clamping process is supported by the carrying and guiding bars. Where, the plates are hanged along the carrying bar and the guiding bar permits only linear horizontal direction movement. Figure 2.1 shows the typical plate and frame heat exchanger in exploded view.

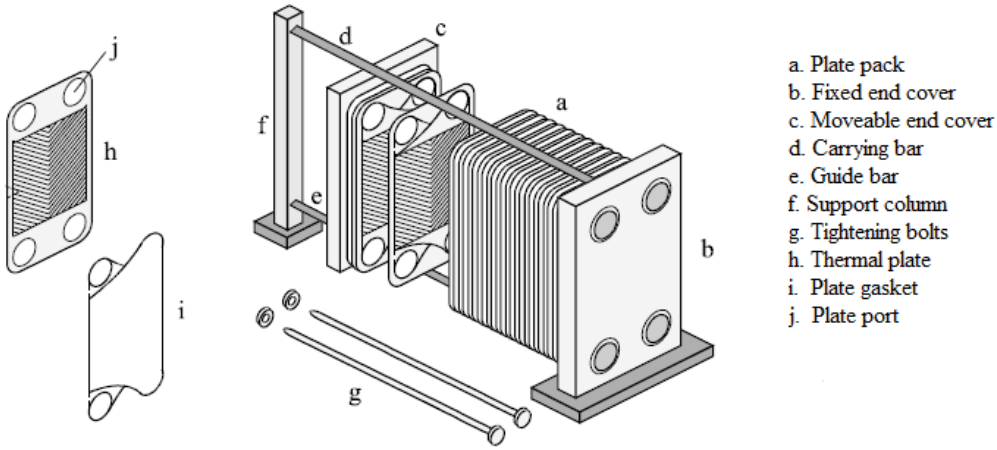

Figure 2.1: Exploded View of Gasketed Plate Heat Exchanger

(Gut & Pinto, 2004)

Brazed Plate Heat Exchanger (BPHE) offer advantages over GPHE in the sense of compactness and it can withstand higher pressure and temperature operation condition. Similar to the GPHE, BPHE consist of a pack of thermal plates and end plates. Unlike GPHE, the plates are brazed together by braze material such as copper and nickel alloy. Therefore, it omits the use of gaskets, frame and tightening bolts. The lack of gaskets as the streams and channels

confining component is the main reason that BPHE is suitable to operate at high temperature and pressure condition. However, this plate attachment method eliminate the possibility to being flexible (expandable) and easy cleaning feature as offer by GPHE.

Semi welded PHE or sometime called twin plate heat exchanger is similar to GPHE. The only distinctive feature is that two plates are weld together to form a channel for a fluid stream and the channel for another stream is made up from the gasketing between two set of twin plates. Usually, this type of PHE is used when one of the fluid streams is relatively corrosive. This corrosive media will be directed to flow into the twin plate and the only gasket connection in this stream is at the porthole. Therefore, the reliability of the system is maximized. This type of heat exchanger are commonly use in chemical process plant, petroleum refinery and refrigeration industry.

Fully weld PHE is the gasket free version of plate and frame heat exchanger. The welded pack of thermal plates is bolted between the cover plates as in GPHE. The plate pack is attached by laser weld in two spatial dimensions along the edges in the plane of the plates so that it allows the expansion and contraction of the plate packs as the pressure and temperature changes. Hence, the pack has higher fatigue resistant. Besides, due to the elimination of gaskets in the system, the structural reliability is enhanced and therefore it can operate at higher temperature and pressure compare to GPHE. The downside of this exchanger is that it only can be clean chemically and it is not possible to expand or reduce the heat transfer surface.

2.2.2 General Characteristics of PHE

Compare to traditional shell and tube heat exchanger, the PHE offer numerous of advantages as shown below:

1. High heat transfer coefficient. The thermal plates which have corrugated surface promote the swirl flow to induce turbulence at low velocity. Together with the small hydraulic diameter and high effective heat transfer area, the heat transfer coefficient is significantly higher than shell and tube heat exchanger at comparable fluid condition.
2. Due to high heat transfer coefficient, the size of the PHE is much smaller than the shell and tube heat exchanger. Wang et al. (2007) stated that, the weight of PHE is about 30% lower and the volume of the system is approximately 20% lesser than shell and tube heat exchanger at same effective heat transfer area.
3. High heat recovery rate compare to shell and tube heat exchanger. Wang et al. (2007) commended that with high heat transfer coefficient and counter flow arrangement. The PHE is able to operate at very close approach temperature. Therefore, about 90% of heat can be recovered compare to that 50% from shell and tube heat exchanger.
4. No cross contaminant problem between fluids. This is due to the streams that are separated by gaskets or by other means and each channel are vent to atmosphere.
5. Low fouling resistance. This is cause by the high turbulence flow inside the channels and surface condition of the plates which is relatively smooth.

6. Possible for high viscosity flow. Because turbulent flow can be achieved at low velocity, the fluid mediums with higher viscosity are applicable in PHE.

2.2.3 Typical Operating Range and Construction of PHE

The typical operating range and geometrical characteristic of PHE are shown in Table 2.1.

Table 2.1 General Operating Range and Typical Geometrical Characteristic of PHE (Wang et al., 2007)

Descriptions	
Maximum operating pressure	25 bar
Maximum operating temperature	160 ℃
Maximum flow rate	3600 m^3/h
Heat transfer coefficient	up to 7500 W/m^2K
Heat transfer area	0.1 - 2200 m^2
Approach temperature difference	As low as 1 ℃
Heat recovery	As high as 93%
NTU	0.3 - 6
Pressure drop	Up to 100 kPa per channel length
Number of plates	Up to 700
Ports size	Up to 435 mm
Plate thickness	0.4 - 1.2 mm
Plate size	0.3 - 3.5 m in length
Plate spacing	1.5 - 5.4 mm
Corrugation depth	1.5 - 5.4 mm

2.2.4 Factors That Influence the Performance of PHE

The performance of PHE is directly influence by several factors such as end plate effect, number of transfer unit (NTU), fouling effect, and heat capacity rate ratio as well as passes arrangement.

2.2.4 (a) End Plate Effect

Typically, the end plates or the two outer plates surface of the PHE do not have fluid flow, hence ideally there are no heat transfer on these plate. Therefore, the outer most channels in the PHE are heated or cold from one side only. This end plates effect will have significant influence on the overall heat transfer coefficient; consequently the thermal performance of the PHE will drop. It is know that, the best heat transfer will occur at a true counterflow arrangement. In order for the PHE to operate approximately to a true counterflow heat exchanger, there are only two methods. The first one, which is likely to be unrealistic, is operating the PHE with a single plate i.e. two channels with one hot fluid and one cold fluid flowing in opposite direction. Secondly, the PHE must have sufficiently large number of channels or plates that the end plate effect can be neglected.

There are several literatures recommended the minimum number of plates or channels in order for the PHE to be modeled as a true counterflow heat exchanger. Among them, Zaleski and Klepacka (1992) found that if the number of channels is more than 24 the effectiveness of PHE approach a true counterflow heat exchanger. Kandlikar and Shah (1989) concluded that in most operating range, the end plates effect can be neglected when the thermal plates is more than 40. Wang et al. (2007) recommended that to achieve inaccuracy of 1% compare to the effectiveness of true counterflow heat exchanger, the PHE should have at least 39 thermal plates. Figure 2.2 shows the effectiveness of 1-1 pass counterflow PHE with respect to NTU and number of thermal plates.

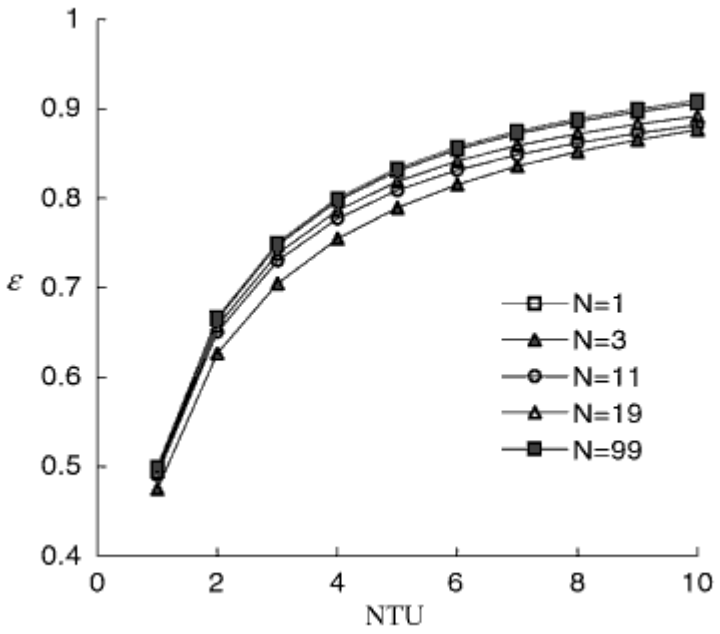

Figure 2.2: Effectiveness of 1-1 Pass Counterflow PHE (Wang et al. 2007)

2.2.4 (b) Number of Transfer Unit (NTU)

NTU is a measure of how near the heat exchanger operates as a true counterflow heat exchanger. The higher the NTU, the closer the heat exchanger approximates the effectiveness of true counterflow heat exchanger. The phenomenon is shown in Figure 2.2. From that figure, the effectiveness of the PHE increases sharply at low NTU. When the NTU goes higher, the effectiveness approaches an asymptotic value to 1.

2.2.4 (c) Fouling Effect

Every heat exchanger is subjected to fouling effect. The collection of unwanted material i.e. dirt, metal dust, etc. on the surface of heat transfer will decrease the heat transfer rate. However, due to its high turbulence, PHE are less prone to this particulate fouling. Meanwhile, the consideration on the fouling effect in the design will result the increase of required heat transfer area. For PHE, the

fouling resistance was only 25% of what shell and tube heat exchanger has as commended by Schlunder (1983). It is also recommended that in PHE design, less than one fifth of the publish value for shell and tubes heat exchanger should be use.

2.2.4 (d) Heat Capacity Flow Rate Ratio

Take the effectiveness NTU relation of the true counterflow heat exchanger in consideration. At a given NTU, the smaller heat capacity rate ratio will give the higher effectiveness to the heat exchanger. The effectiveness is lowest when the heat capacity rate ratio is equal to 1. Figure 2.3 shows the relationship between the effectiveness and heat capacity rate ratio of a counterflow heat exchanger. As for PHE, the heat capacity rate ratio is usually given in the design and it is a fix value.

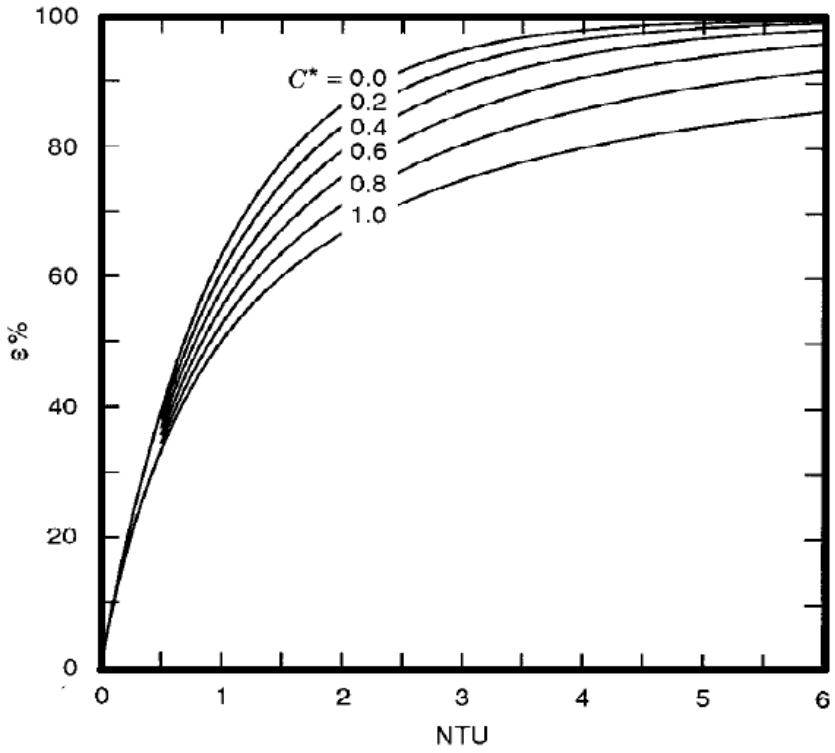

Figure 2.3: Effectiveness-NTU Chart for Counterflow Heat Exchanger

(Shah & Sekulic, 2003)

2.2.4 (e) Pass Arrangement

The PHE can be design in such a way that it has different number of passes in each fluid. Normally, for 1-1 pass (one pass at hot side and one pass at cold side) the flow arrangement will be in counterflow because it has higher effectiveness and heat transfer rate than parallel flow system. Therefore, in the design, the pass arrangement must be carefully selected to yield the highest possible thermal performance. For ease of comparison, the correction factor is use where correction factor equal to 1 for true counterflow heat exchanger. The types of arrangement for 1-1 pass system are shown in Figure 2.4 and the correction factor with respect to the arrangement is shown in Figure 2.5. With reference to Figure 2.4, the type of arrangement also depends on the numbers of thermal plate i.e. odd or even number. From Figure 2.5, at low thermal plates number, the arrangement with even number of plate posses higher performance. This phenomenon was also observed by Shah and Kandlikar (1988)

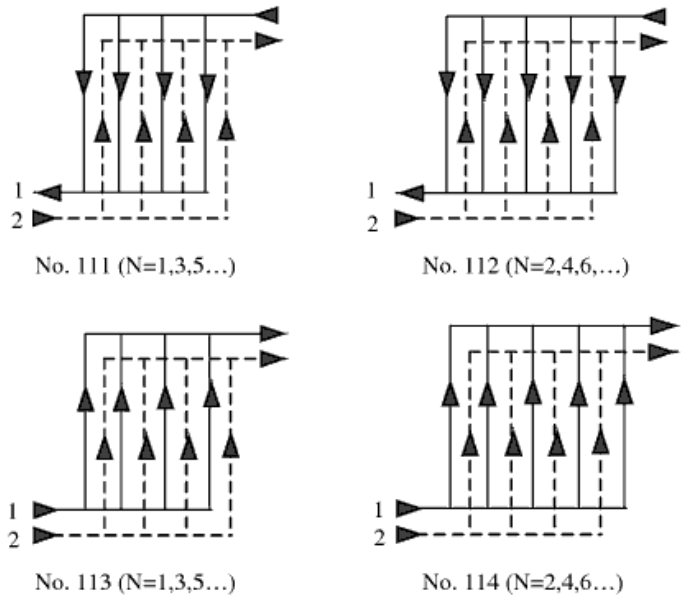

Figure 2.4: Type of 1-1 pass PHE Arrangement (Wang et al., 2007)

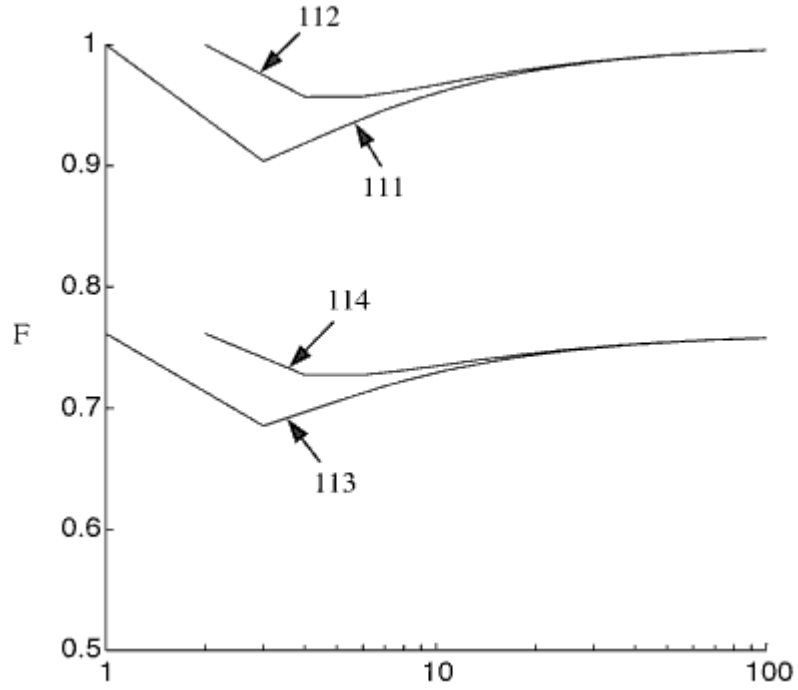

Figure 2.5: Correction Factor for 1-1 Pass Arrangement at Heat Capacity Rate Ratio Equal to 1 and NTU Equal to 1 (Wang et al., 2007)

2.3 Single Phase Flow on Chevron Plate

The corrugation pattern on the thermal plates serves two main purposes, that is, induce turbulence and increase the heat transfer surface area. Generally, there are two types of corrugation pattern for thermal plate as shown in Figure 2.6. The most common corrugation pattern use in the industry is in chevron or herringbone type. Since the PHE in this study uses chevron type corrugation and the heat transfer process is from liquid to liquid, the literature only focus on the single phase flow on chevron plate.

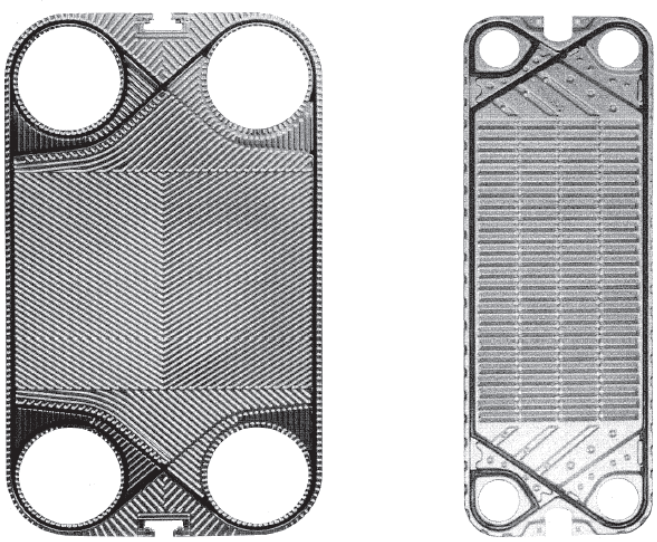

Figure 2.6: Types of Thermal Plate (DHP Engineering)

2.3.1 Characteristic of Chevron Plate

Chevron plate is distinctive from its V-shape corrugation pattern. The most important parameter for chevron plate is the chevron angle β, this parameter directly related to the thermal and hydrodynamic performance of PHE. Khan, Khan, Chyu and Ayub (2010) in their experiment found that at a given Reynolds number, the Nusselt number increase by 4 to 9 times at various β compare to flat plate. Plate with low chevron angle will have lower heat transfer coefficient but flow frictional losses is lower. Conversely, high chevron angle has higher heat transfer coefficient and correspondingly higher frictional loss. The low and high chevron angle plates can be stacked symmetrically i.e. low-low and high-high, or mixing between high and low plate depending on the desire thermal and hydrodynamic output. Figure 2.7 shows the basic geometrical characteristic of chevron plate while Table 2.2 listed the description of these important geometric characteristic.

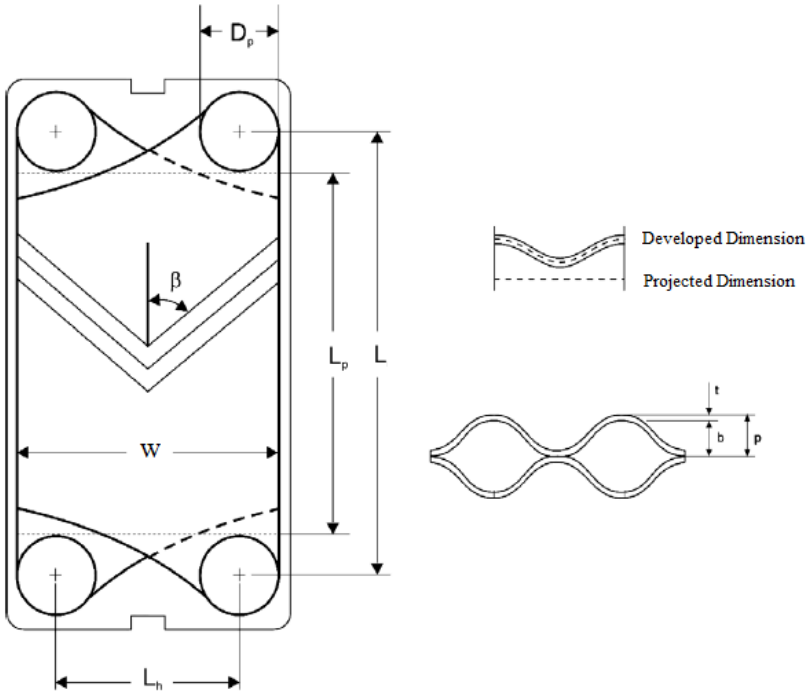

Figure 2.7: Geometrical Characteristic of Chevron Plate (Khan et al., 2010)

Table 2.2: Important Geometrical Characteristic of Chevron Plate

Characteristic	Description
Chevron angle, β	Induce turbulence flow. As a basic measurement for thermal performance of the plate. High β, greater thermal efficiency. Low β has lower heat transfer coefficient.
Effective width of plate, w	Width of plate inside the boundary of gasket. $w = L_h + D_p$
Port to port vertical length, L	Distance between center of top and bottom ports. Important parameters in pressure drop calculation
Surface enlargement factor, ϕ	The ratio of actual (developed) heat transfer area to projected area ($A_{projected} = L_p \times w$)
Corrugation depth, b	Difference between plate pitch and plate thickness
Equivalent diameter, D_e	Important in Reynolds number, heat transfer coefficient and channel frictional losses calculation, $D_e = 2b$
Channel flow cross sectional area, A_c	Important for Reynold number and channel frictional losses calculation, $A_c = w \times b$

2.3.2 Heat Transfer and Pressure Drop Correlations

2.3.2 (a) Heat Transfer Correlation

Generally, empirical correlations for single phase flow heat transfer are in the form of

$$Nu = CRe^{m}Pr^{n} \cdots\cdots\cdots\cdots\cdots (2.1)$$

The specific value for coefficient C and exponent of m and n vary with the nature of the surface geometry and type of flow but often independent of the nature of the fluid. Khan et al. (2010), in their experimental study on commercial PHE with symmetry (30°/30° & 60°/60°) and mix (30°/60°) chevron plate configuration found that the Nusselt number was increase as the Reynolds number and chevron angle increase. Therefore, they proposed a heat transfer correlation that accounting the effect of various chevron angles. This correlation is valid on Reynolds number from 500 to 2500, Prandtl number from 3.5 to 6.5, chevron angle from 30° to 60° and surface enlargement factor of 1.117.

Muley and Manglik (1999) carried out an experiment for single phase flow in a single pass U-type counterflow PHE using water as heat transfer medium. In this study, two symmetry chevron plate arrangements namely (30°/30° & 60°/60°) and mix plates arrangement (30°/60°) was consider. They observed that compare to flat plate, 2 to 5 times higher Nusselt number can be obtained from different chevron angle and the increase in surface enlargement factor also poses similar trend but smaller effect. They also found that at constant pumping power, the heat transfer can be enhanced by a factor of 2.8 compare to equivalent flat plate depending on Reynolds number, chevron angle and surface enlargement factor. Base on the experimental data, they came out

with a correlation to predict the Nusselt number that is valid for chevron plate with sinusoidal corrugation, Reynolds number range from 600 to 10000, Prandtl number of 2 to 6, chevron angle from 30° to 60°, and surface enlargement factor from 1 to 1.5.

In the same year, Muley, Manglik and Metwally (1999) used similar experimental set up to study the viscous fluid flow in PHE. They found that the chevron plate achieved 2.9 times higher heat transfer rate as compare to flat plate at constant pumping power and required 48% less surface area to achieve a given heat transfer rate at a predetermined pressure drop limit. Similarly, a correlation to predict the heat transfer performance was developed and this correlation is valid for viscous laminar flow at Reynolds number from 2 to 400, Prandtl number in between 130 and 290, chevron angle from 30° to 60°, surface enlargement factor of 1.29 and corrugation profile aspect ratio of 0.56.

Among other earlier researches, Okada et al. (1972) in their research, proposed heat transfer correlations for different symmetric plate arrangement. These correlations are valid for water at Reynolds number from 700 to 25,000. Focke, Zachariades and Olivier (1985) constructed several set of correlations for different chevron angle at different range of Reynold number. Chrisholm and Wanniarachchi (1992) correlated their experimental data for both symmetric and mix plate arrangement for chevron angle 30° to 80° at Reynold number in between 1000 and 40,000. Heavner, Kumar and Wanniarachchi (1993) studied turbulent flow of water in symmetric and mixed chevron plate arrangement at chevron angle 23° 45° and 90°, they developed correlations that valid for Reynolds number in between 400 and 10,000. For summary, all the correlations mentioned above and their validity ranges are tabulated in Table 2.3.

2.3.2 (b) Pressure Drop Correlations

Friction factor is the key parameter in pressure drop calculation. In hydrodynamic performance analysis, researchers use the experimental data to find the factor that represent the shear losses within the PHE channels. Muley and Manglik (1999) found that the increase in chevron angle leads to 13 to 44 times higher friction factor within the flow passages. They proposed a friction factor correlation that valid in same range as the heat transfer correlation mentioned above. Similarly, Muley et al. (1999) found that the friction factor is 6.6 times higher than the equivalent flat plate at same flow condition. In their study a friction factor correlation was constructed for viscous flow in PHE.

The friction factor for both aforementioned studies and other researches namely (Chrisholm & Wanniarachchi, 1992; Focke et al., 1985; Heavner et al., 1993) are presented in Table 2.4.

Table 2.3: Heat Transfer Correlation and Their Validity Range.

Reference	Chevron angle	Reynolds number	Prandtl number	Surface enlargement factor	Correlation
(Okada et al., 1972)	30, 45, 60, 75	700 – 25,000	water	-	$\mathrm{Nu} = CRe^{m}Pr^{0.4}$ (2.2)
(Focke et al., 1985)	30, 45, 60	20 – 50,000	-	-	$\mathrm{Nu} = CRe^{m}Pr^{0.5}$ (2.3)
(Chrisholm & Wanniarachchi, 1992)	30 - 80	1000 - 4000	-	-	$\mathrm{Nu} = 0.72Re^{0.59}Pr^{0.4}\phi^{0.41}\left({}^{\beta}/_{30}\right)^{0.66}Pr^{0.5}$ (2.4)
(Heavner et al., 1993)	23, 45, 90	400 – 10,000	-	-	$\mathrm{Nu} = C\phi^{1-m}Re^{m}Pr^{0.5}\left({}^{\mu}/_{\mu_{wall}}\right)^{0.17}$ (2.5)
(Muley & Manglik, 1999)	30 - 60	600 – 10,000	2 - 6	1 - 1.5	$\mathrm{Nu} = [0.2668 - 0.006967\beta + 7.244\times10^{-5}\beta^{2}] \times [20.78 - 50.94\phi + 41.16\phi^{2} - 10.51\phi^{3}] \times Re^{\left[0.728+0.0543sin\left[\left({}^{\pi\beta}/_{45}\right)+3.7\right]\right]}Pr^{1/3}\left({}^{\mu}/_{\mu_{wall}}\right)^{0.14}$ (2.6)
(Muley et al., 1999)	30 - 60	30 - 400	130 - 290	1.29	$\mathrm{Nu} = 1.6774(D_e/L)^{1/3}\times Re^{0.5}Pr^{1/3}(\beta/30°)^{0.38}\left({}^{\mu}/_{\mu_{wall}}\right)^{0.17}$ (2.7)
(Khan et al., 2010)	30 - 60	500 - 2500	3.5 - 6.5	1.117	$\mathrm{Nu} = (0.0161\beta/\beta_{max} + 0.1298)Re^{\left[\frac{0.198\beta}{\beta_{max}}+0.6398\right]}Pr^{0.35}(\mu/\mu_{wall})^{0.14}$ (2.8)

Table 2.4: Friction Factor Correlations

Reference	Chevron angle	Reynolds number	Prandtl number	Surface enlargement factor	Correlation
(Focke et al., 1985)	30, 45, 60	90 – 50,000	-	-	For β = 30° $f = \begin{cases} 0.0925 + {}^{57.5}/_{Re}; 260 < Re < 3000 \\ 0.8975Re^{-0.263}; 3000 < Re < 50{,}000 \end{cases}$ For β = 45° $f = \begin{cases} 0.3025 + {}^{91.75}/_{Re}; 150 < Re < 1800 \\ 1.46Re^{-0.177}; 1800 < Re < 30{,}000 \end{cases}$ For β = 60° $f = \begin{cases} 1.2575 + {}^{188.75}/_{Re}; 90 < Re < 400 \\ 6.7Re^{-0.209}; 400 < Re < 16{,}000 \end{cases}$ (2.9)
(Chrisholm & Wanniarachchi, 1992)	30 - 80	1000 - 4000	-	-	$f = 0.8Re^{-0.25}\phi^{1.25}\left({}^{\beta}/_{30}\right)^{3.6}$ (2.10)
(Heavner et al., 1993)	23, 45, 90	400 – 10,000	-	-	$f = C\phi^{1+m}Re^{-m}$ (2.11)
(Muley & Manglik, 1999)	30 - 60	600 – 10,000	2 - 6	1 - 1.5	$f = [2.917 - 0.1277\beta + 2.016 \times 10^{-3}\beta^2] \times [5.474 - 19.02\phi + 18.93\phi^2 - 5.341\phi^3] \times Re^{-\left[0.2+0.0577sin\left[\left({}^{\pi\beta}/_{45}\right)+2.1\right]\right]}$ (2.12)
(Muley et al., 1999)	30 - 60	2 - 300	130 - 290	1.29	$f = \left[\left(\frac{30.2}{Re}\right)^5 + \left(\frac{6.28}{Re^{0.5}}\right)^5\right]^{0.2} (\beta/30°)^{0.83}$ (2.13)

2.4 Nanofluids

The term “nanofluids” was first introduced by Choi and Eastman (1995) to describe a colloidal mixture of nanoparticle with size from 1 to 100 nm and a base fluid. These heat transfer fluids exhibit superior thermal properties compare to the base fluid i.e. water and ethylene glycol (EG). For example, Eastman et al. (2001) found that the effective thermal conductivity of copper oxide CuO-EG nanofluids is 40% higher compare to the base fluid at 0.3% particle volume concentration. This enhancement on thermal conductivity means there are chances to further improve the heat transfer on commercial system nowadays. Hence, there is growth in research activities related to this field.

Literatures indicated that the enhancement in thermal conductivity is strongly dependent on the nanoparticle size, volume fraction, geometry, material, temperature of fluid and properties of base fluid. Among them, Nguyen et al. (2007) investigated the heat transfer behaviour of a water block cooled by alumina (Al_2O_3) water nanofluids with two different particles average diameter (36nm and 47nm) and various volume concentrations (1%, 3.1% and 6.8%). They noticed at a given flow rate, the thermal conductivity of water block increased by 12%, 18% and 38% for nanofluids with particle volume concentration of 1%, 3.1% and 6.8% respectively compare to water block cooled by water. They also found that, for a given Reynolds number and particle volume concentration, the value of Nusselt number obtained for 36 nm particle nanofluids is higher than 47 nm particles, hence they commented that nanofluids with smaller particle size will have greater number of particles in the fluid that lead to the rise in total contact area that provide a more effective heat exchange between the particles and the continuous liquid phase. Meanwhile, they also noticed that the corresponding increase of Nusselt number due to Reynolds number appears generally less significant than that due to an increase of particle volume concentration. The

similar trend on the effect of particle volume fraction and size were observed by Li and Peterson (2007), Teng, Hung, Teng, Mo and Hsu (2010), Vajjha and Das (2009a) and Zamzamian, Oskouie, Doosthoseini, Joneidi and Pazouki (2011).

The effect of particle geometry to the thermal conductivity can be shown by study of Liu, Wang, Zhang, Zhang and Liu (2008). In the study they found that multi wall carbon nano tube (MWCNT) poses greater thermal enhancement than CuO and silicon dioxide (SiO_2) at same volume fraction. This result can be link to the geometry (aspect ratio) of the MWCNT which is larger than oxide particle normally assume to be in spherical shape with aspect ratio equal to 1. Similarly, Wang and Mujumdar (2007) in their study commended that the particle shape or aspect ratio of the particle is a significant parameter to affect the thermal performance of nanofluids.

Meanwhile, the effect of temperature to the thermal conductivity of nanofluids is shown in (Vajjha & Das, 2009a). In the study, they found that for Al_2O_3 nanofluids, the thermal conductivity increase as the square of the temperature. Take for example, at 6% particle volume concentration; a rise of 21% to the thermal conductivity ratio was observed when the temperature increased from 298K to 363K. Das, Putra, Thiesen and Roetzel (2003) used temperature oscillating technique to measure the thermal diffusivity of nanofluids and calculated the thermal conductivity; they found that 2 to 4 fold increase in thermal conductivity enhancement is obtained from temperature range of 294 K to 324 K. Yu, Xie, Chen and Li (2010) in their investigation on thermal transport properties of EG base nanofluids containing copper nanoparticles concluded that the thermal conductivity strongly dependant on the temperature of the fluid and it is due to the higher degree of Brownian motion when temperature of fluid increase.

For the effect of particle material wise, Godson, Raja, Lal and Wongwises (2010) reviewed that the enhancement of thermal conductivity using metal particles nanofluids is higher compare to the metal oxide nanofluids, for example, metal oxide nanofluids with volume concentration at 5% typically has thermal conductivity enhancement up to 30%, while metal nanofluids with just less than 1.5% volume concentration can enhance the thermal conductivity up to 40%.

Finally, the effect of base fluid properties can best shown by study of Lee, Choi, Li and Eastman (1999). In their experiment, thermal conductivity of four types of nanofluids namely Al_2O_3-water, Al_2O_3-EG, CuO-water and CuO-EG are measured by transient hot wire method, they observed that for nanofluids using the same nanoparticle, the thermal conductivity ratio of nanofluids for EG based systems are always higher than that of water based one.

2.4.1 Nanofluids Thermophysical Properties Correlations

2.4.1 (a) Thermal Conductivity

The earliest model to estimate the effective thermal conductivity of solid-liquid mixture is from (Maxwell, 1904) commented by Vajjha and Das (2009a). This model assumed particles are in spherical shape and the parameters involve are only particles volume concentration and thermal conductivity of particles and base fluid. Hamilton and Crosser (1962) modified Maxwell's model to include the shape factor in the thermal conductivity prediction to account for the effect of the shape of particles. However, these theoretical equations are not suitable for the prediction on the thermal conductivity of nanofluids as noted by Hwang et al. (2006), Jang and Choi (2007) and Vajjha and Das (2009a). Since the thermal conductivity of nanofluids is related to the parameters mentioned in

previous section, numerous new correlations have been constructed experimentally or theoretically. Among them, Koo and Kleinstreuer (2004) took account of Brownian motion of particle in the thermal conductivity prediction. Vajjha and Das (2009a) used larger experimental data to improve Koo and Kleinstreuer (2004) correlation. Recently, Corcione (2011) constructed a correlation to predict the thermal conductivity of nanofluids base on large number of experimental data available in literature. With only 1.86% standard deviation of error, this correlation can predict nanofluids made from Al_2O_3, CuO, titania (TiO_2) and other material with base fluid of water or EG. This correlation is applicable to nanoparticle range from 10 nm to 150 nm diameter, particle volume fraction from 0.2% to 9% and temperature from 294K to 324K.

As summary, the correlations mentioned above are shown in Table 2.5.

Table 2.5: Correlations for Prediction of Thermal Conductivity

References	Correlation	Note
(Maxwell, 1904)	$k_{eff} = k_f \frac{k_p + 2k_f + 2(k_p - k_f)\varphi}{k_p + 2k_f - (k_p - k_f)\varphi}$ (2.14)	
(Hamilton & Crosser, 1962)	$k_{eff} = k_f \frac{k_p + (n-1)k_f - (n-1)(k_f - k_p)\varphi}{k_p + (n-1)k_f + (k_f - k_p)\varphi}$ (2.15)	
(Koo & Kleinstreuer, 2004)	$k_{nf} = k_f \frac{k_p + 2k_f - 2(k_f - k_p)\varphi}{k_p + 2k_f + (k_f - k_p)\varphi} + 50000\beta\varphi\rho_f c_{p,f} \times \sqrt{\frac{k_b T}{\rho_p d_p}} f(T,\varphi)$ $f(T,\varphi) = (-6.04\varphi + 0.4705)T + (1722.3\varphi - 134.63)$ (2.16)	β is the curve-fit relations obtained in their experiment
(Vajjha & Das, 2009a)	$k_{nf} = k_f \frac{k_p + 2k_f - 2(k_f - k_p)\varphi}{k_p + 2k_f + (k_f - k_p)\varphi} + 50000\beta\varphi\rho_f c_{p,f} \times \sqrt{\frac{k_b T}{\rho_p d_p}} f(T,\varphi)$ $f(T,\varphi) = (0.028217\varphi + 0.003917)\frac{T}{T_0} + (-0.030669\varphi - 0.00391123)$ (2.17)	β is the curve-fit relations obtained in their experiment
(Corcione, 2011)	$k_{nf} = \left[1 + 4.4Re^{0.4}Pr^{0.66}\left(\frac{T}{T_{fr}}\right)^{10}\left(\frac{k_p}{k_f}\right)^{0.03}\varphi^{0.66}\right]k_f$ $Re = \frac{2\rho_f k_b T}{\pi\mu_f^2 d_p}$ (2.18)	

2.4.1 (b) Viscosity

For heat transfer systems that employ fluid flow, viscosity of the working fluid is as crucial as its thermal conductivity. Fluid viscosity is the main reason for exists of frictional losses in the flow system and ultimately causing increase of needed pumping power. For nanofluids, the viscosity also affects the thermal conductivity in the sense of Brownian motion. At increase of temperature, the nanofluids viscosity will decrease and causing an increase in the average velocity of Brownian motion of the nanoparticles. In open literatures, there are significantly less researches on the nanofluids viscosity compare to its thermal conductivity. Hence, there are only a few correlations to predict the nanofluids viscosity.

The widely use theoretical model is from (Brinkman, 1952), this equation was develop to relate the viscosity to the function of particle volume fraction. However, Corcione (2011), Hosseini, Mohebbi and Ghader (2011) and Nguyen et al. (2008) observed that the prediction of viscosity by Brinkman's equation underestimated the actual viscosity of nanofluids.

Namburu, Kulkarni, Misra and Das (2007) found that the viscosity of CuO-60:40 EG/water nanofluids reduced as the temperature increased and the viscosity increased as the particle volume fraction increased. Therefore, they constructed a correlation for nanofluids viscosity that accounted the effect of temperature and particle volume fraction. Nguyen et al. (2008) found that Al_2O_3-water nanofluids viscosity calculated by Brinkman's equation underestimate their experimental data, except for nanofluids with particle volume concentration less than 1%. Furthermore, they observed that the viscosity of nanofluids depends strongly on both temperature and volume concentration; while effect of

particle size only significant at high volume concentration. In this study, they proposed two set of correlations, the first one is due to particle size while the second one is temperature dependent. However, these correlations are only applicable only to Al_2O_3-water nanofluids.

Corcione (2011) derived a new correlation to predict the nanofluids effective viscosity from a wide selection of experimental data. This correlation is applicable to nanofluids made from Al_2O_3, TiO_2, SiO_2 and Cu nanoparticles with size ranging from 25nm to 200nm that are disperse water, EG, propylene glycol (PG) or ethanol. At 1.84% standard deviation of error, this correlation is good in predicting the nanofluids lies between 293K to 333K and particle volume fraction range from 0.01% to 7.1%. Table 2.6 listed the aforementioned correlations.

Table 2.6: Correlations for Prediction of Viscosity

References	Correlation
(Brinkman, 1952)	$\mu_{nf} = \frac{1}{(1-\varphi)^{2.5}}\mu_f$ (2.19)
(Namburu et al., 2007)	$Log(\mu_{nf}) = Ae^{-BT};\ \mu_{nf}\ in\ centipoise\ (cP)$ $A = 1.8375(\varphi)^2 - 29.643(\varphi) + 165.56$ $B = 4 \times 10^{-6}(\varphi)^2 - 0.001(\varphi) + 0.0186$ (2.20)
(Nguyen et al., 2008)	$\mu_{nf} = \mu_f(0.904e^{0.1483\varphi}); for\ d_p = 47nm$ $\mu_{nf} = \mu_f(1 + 0.025\varphi + 0.015\varphi^2); for\ d_p = 36nm$ $\mu_{nf} = \mu_f(1.125 - 0.0007T); for\ \varphi = 1\%$ $\mu_{nf} = \mu_f(2.1275 - 0.0215T + 0.0002T^2); for\ \varphi = 4\%$ (2.21)
(Corcione, 2011)	$\mu_{nf} = \mu_f\left[\frac{1}{1 - 34.87\left(\frac{d_p}{d_f}\right)^{-0.3}\varphi^{1.03}}\right];$ $d_f = 0.1\left(\frac{6M}{N\pi\rho_{f0}}\right)^{\frac{1}{3}}$ (2.22)

2.4.1 (c) Specific Heat

Dispersing nanoparticle in the base fluid may enhance the thermal conductivity of the fluid but the thermal enhancement might be offset by the increased of viscosity and specific heat of nanofluids. Therefore, specific heat of nanofluids plays an important role in thermal enhancement. However, the investigation on nanofluids specific heat seems to be not as attractive as thermal conductivity of nanofluids. In open literatures, the first theoretical equation to predict nanofluids specific heat is the one used by Pak and Cho (1998), this equation calculate the specific heat of nanofluids by considering only the particle volume concentration. Later on, Xuan and Roetzel (2000) modified this equation to involve the density of nanofluids with assumption that thermal equilibrium can be achieve in between the solid particle and base fluid. This equation was widely use by researchers in estimating the specific heat of nanofluids. Vajjha and Das (2009b) experimentally investigate the specific heat of Al_2O_3, SiO_2 and ZnO nanofluids and found that equation proposed by Pak and Cho (1998) overestimated the actual specific heat of nanofluids while equation by Xuan and Roetzel (2000) underestimated them. Hence, they proposed a correlation to predict specific heat of all three above-mentioned nanofluids. Table 2.7 listed the correlations for predicting specific heat of nanofluids.

Table 2.7: Correlations for Prediction of Specific Heat

Reference	Correlation	Note
(Pak & Cho, 1998)	$c_{p,nf} = c_{p,f}(1-\varphi) + \varphi c_{p,p}$ (2.23)	
(Xuan & Roetzel, 2000)	$c_{p,nf} = \frac{\varphi\rho_p c_{p,p} + \rho_f c_{p,f}(1-\varphi)}{\rho_{nf}}$ (2.24)	
(Vajjha & Das, 2009b)	$c_{p,nf} = c_{p,f}\frac{\left((AT) + B\left(\frac{c_{p,p}}{c_{p,f}}\right)\right)}{(C+\varphi)}$ (2.25)	A,B and C are curve fit coefficient obtained from their experiment

2.4.1 (d) Density

The broadly use equation in calculating density of nanofluids is from (Pak & Cho, 1998), this equation accounting only the effect of particle volume concentration to the density. Vajjha, Das and Mahagaonkar (2009) found that density calculated by this equation provide very good agreement to their experimental results for Al_2O_3 and antimony-tin oxide (Sb_2O_5:SnO_2) nanofluids, while for ZnO nanofluids the calculated result has an absolute average deviation of 3.29% compare to measured data. Hence, for ZnO nanofluids, they introduced a correction factor that must be subtracted from density calculated by Pak and Cho (1998) equation.

Table 2.8: Equations for Prediction of Density

Reference	Correlation
(Pak & Cho, 1998)	$\rho_{nf} = \rho_p\varphi + \rho_f(1 - \varphi)$ (2.26)
(Vajjha, et al., 2009)	$\rho_{nf} = \left[\rho_p\varphi + \rho_f(1 - \varphi)\right] - CF$ $CF = \frac{0.9848\varphi + 0.7382}{100}$ (2.27)

2.4.2 Force Convective Heat Transfer of Nanofluids

Due to its high thermal conductivity, nanofluids show its potential as working fluid in heat transfer devices. There are a lot of researches been carried out to investigate the usefulness of nanofluids as heat transfer fluids and the potential applications of nanofluids has been summarized by Saidur et al. (2011).

Force convective heat transfer systems involve the heat transfer fluid flow by pump, application of nanofluids might increase the heat transfer rate and consequently decrease the volumetric flow rate supply by pump to achieve the

required heat transfer rate. Conversely, the increase in viscosity of nanofluids may also cause increase of frictional losses that lead the higher pressure drop within the system. Therefore in energy conservation point of view, the aim of using nanofluids to replace conventional heat transfer fluid is to maintain the same amount of existing heat transfer rate by using less fluid and at the same time reduce or maintain the same amount of pumping power.

Contrary to this, Pantzali, Mouza and Paras (2009) in their experimental study on nanofluids as working fluid in welded plate heat exchanger found that for a given Reynolds number, the nanofluids helps to increase the heat transfer rate but at the same time the flow rate is higher compare to that of water. Detail investigation revealed that for a given heat duty, there are no difference between the volumetric flow rate of water and nanofluids. However, the required pumping power of nanofluids is twice for the water.

Other than that, nanofluids may also helps in reduction of heat transfer area by increasing the heat transfer rate. Leong, Saidur, Kazi and Mamun (2010) found that by applying nanofluids as the coolant of car radiator, the heat transfer was enhanced by 3.8%. This helps in reduction of air frontal area of about 18.7%.

3.0 RESEARCH METHODOLOGY

3.1 Introduction

In this chapter, the procedure to carry out the research will be briefly explained. At the same time, the basic information of the PHE in this study such as the geometrical characteristics, operating and rated condition is stated. Furthermore, the general assumptions or idealizations involved in the thermal and hydrodynamic performance analysis are also listed.

Then, the mathematical formulation to estimate the thermal and hydrodynamic performance of PHE are shown and explained systematically. In addition, the important correlations and equations chosen in the study such as correlation to estimate the thermophysical properties of nanofluids, Nusselt number and friction factor are briefly explained.

Thereafter, to validate the consistency of correlation used in the estimation of nanofluids thermal conductivity, the calculated results are compared with the values estimated by presently discovered experimental correlation. Similarly, to identify whether the formulated mathematical steps are appropriate and reliable, they are validated by comparing the calculated results with the actual rated condition given by PHE manufacturer.

3.2 Research Procedure

To make this study successful, the foremost step is to determine the objectives for the study. After that, literature review is carried out to observe the current trend of research and to obtain the needed information such as experimental correlations, input data etc.

Then, calculation steps is constructed to obtain the require results corresponding to the specify objective. At the same time, the mathematical formulation is validated by comparing the result with rated value. After the mathematical model is validated, the calculated results are analyzed. Finally, the research ended with the conclusions made with respect to the analyzed results and findings. In brief, the research procedure is illustrated in flow chat as shown in Figure 3.1.

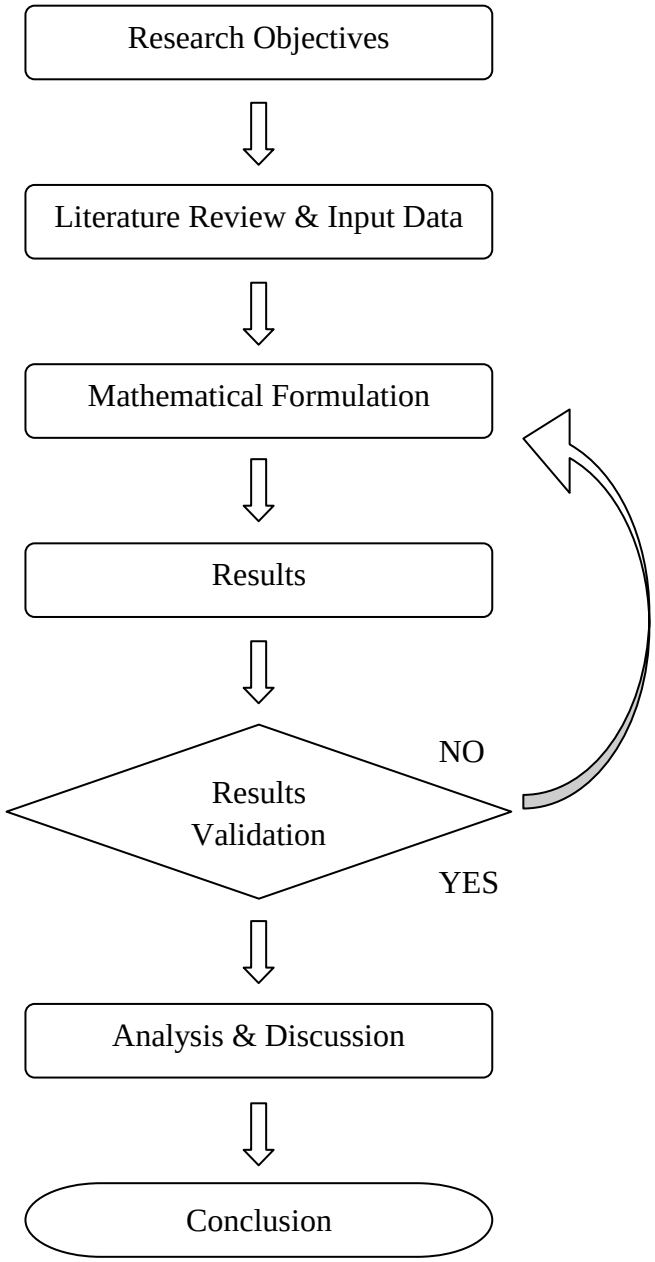

Figure 3.1: Research Flow Chart

3.3 Input Data

In this study, the selected PHE is a gasketed PHE from DHP Engineering Co. Ltd. It is used as centralize cooling system in oil and gas industries to cool the appliances in offshore platform. Schematic diagram for the system is shown in Figure 3.2 and the direction of flow for hot and cold side is schematically shown in Figure 3.3. In this PHE system, fresh water is use as the medium to carry heat from the appliances and the cooling fluid is sea water with 4% salinity. The thermal plates of this PHE are made of titanium with chevron (herringbone) type corrugation. The geometrical characteristics and the operating conditions of this PHE are listed in Table 3.1 and Table 3.2 respectively.

In the calculations, required properties of water and nanoparticles are obtained from (Incropera & DeWitt, 2002) and are listed in Table 3.3 and Table 3.4 respectively. Meanwhile, the properties of sea water shown in Table 3.5 are acquired from (Sharqawy, Lienhard, & Zubair, 2010). For the hot and cold working fluid, interpolation is made to obtain the values corresponding to the average of inlet and outlet temperature. While, the particles properties are taken at 300K.

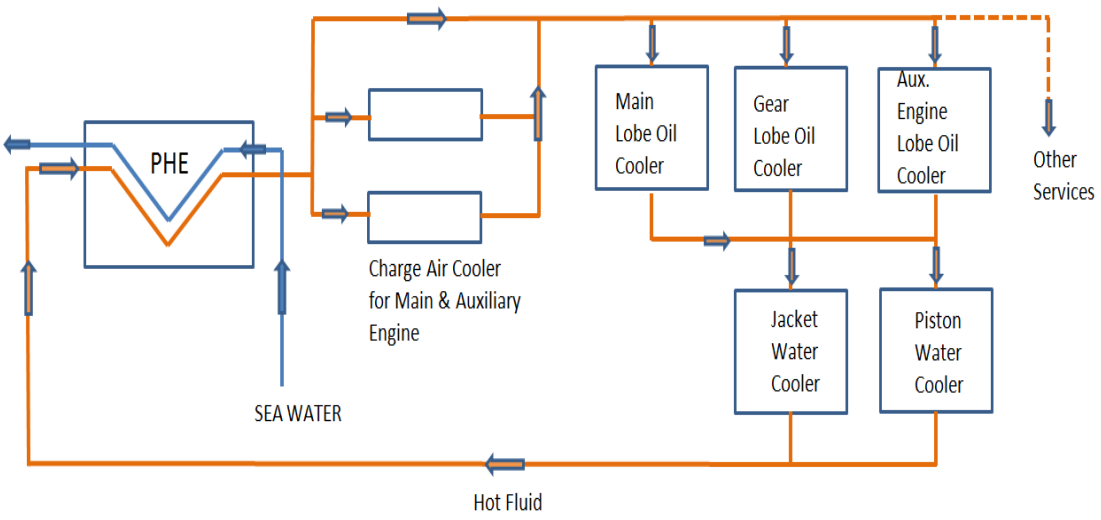

Figure 3.2 Schematic Diagram of PHE System (DHP Engineering)

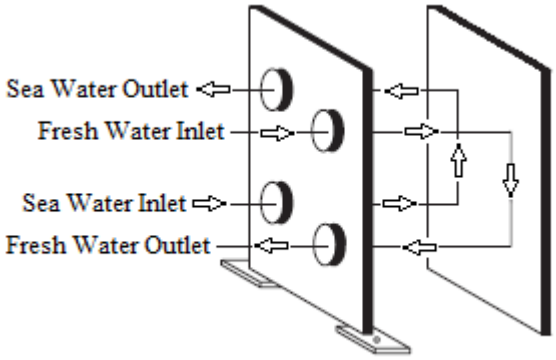

Figure 3.3: Flow Direction of Working Fluids (DHP Engineering)

Table 3.1: Characteristics of PHE (DHP Engineering)

Description			
Thermal plate material		Titanium	
Number of plates	N_{plate}	51	
Number of channels	N	25	
Number of passes	N_{pass}	1-1	
Plate thermal conductivty	k_{plate}	21.9	W/mK
Plate thickness	δ_{plate}	0.0005	m
Surface enlargement factor	ϕ	1.1530	
Effictive plate area	A_{plate}	0.39	m^2
Total effective plate area	A_{total}	19.11	m^2
Corrugation depth	b	0.0030	m
Effective diameter	D_e	0.0060	m
Effective width of plate	w	0.4088	m
Channel flow cross section area	A_c	0.00123	m^2
Chevron angle	β	60	degree
Port to port Length	L	0.9360	m

Table 3.2: Operating Condition (DHP Engineering)

Description		Hot Side		Cold Side	
Heat transfer medium		Fresh water		Sea Water 4% salinity	
Inlet temperature	T_i	314	K	305	K
Outlet temperature	T_o	309	K	309	K
Mean temperature	T_{avg}	311.5	K	307	K
Mass flow rate	$\dot{m}_{total}$	22.22	kg/s	28.34	kg/s
Total pressure drop	Δp_{total}	34,548	Pa	53,701	Pa
Heat transfer rate	q	460	kW		
Overall heat transfer coefficient	U	5475	W/m^2K		

Table 3.3: Thermophysical Properties of Water at 311.5K (Incropera & DeWitt, 2002)

Properties			
Specific Heat	c_p	4178.30	J/kgK
Dynamic Viscosity	μ	0.0006758	Ns/m^2
Density	ρ	992.46	kg/m^3
Thermal Conductivity	k	0.6298	W/mK
Prandlt Number	Pr	4.482	

Table 3.4: Thermophysical Properties of Nanoparticles at 300K (Incropera & DeWitt, 2002)

Particles Properties		Al_2O_3		SiO_2	
Thermal Conductivity	k	36	W/mK	1.38	W/mK
Density	ρ	3970	kg/m^3	2220	kg/m^3
Specific Heat	c_p	765	J/kgK	745	J/kgK

Table 3.5: Thermophysical Properties of Sea Water (4% salinity) at 307K (Sharqawy et al., 2010)

Properties			
Specific Heat	c_p	3980.32	J/kgK
Dynamic Viscosity	μ	0.0008090	Ns/m^2
Density	ρ	1024.32	kg/m^3
Thermal Conductivity	k	0.6202	W/mK
Prandlt Number	Pr	5.194	

3.4 General Assumptions in Thermal and Hydrodynamic Analysis of PHE

3.4.1 General Assumptions in Thermal Analysis of PHE

In order to analyze the thermal performance of PHE which use nanofluids as the hot fluid medium, some conditions within the system are idealized. The idealizations/ assumptions made to simplify the thermal analysis in this study are:

1. The heat exchanger operates under steady state condition. Where, the fluids flow rates and temperature within the heat exchanger and at the inlet are independent of time.
2. There are negligible heat losses to the surrounding i.e. adiabatic walls at outside of the exchanger. Kandlikar and Shah (1989) quoted that this idealization is reasonable since there is an air gap between the end plate and cover plate of the heat exchanger.
3. The individual and overall heat transfer coefficient is constant and uniform throughout the heat exchanger.
4. The flow inside the channel is thermally fully developed.

5. The velocity of the fluid is assumed to be constant across the cross section of the channel perpendicular to the axis of flow.
6. There are no misdistributions of fluid flow for every channel. Therefore, the fluid flow is uniformly distributed to every channel on each side and the fluid is perfectly mixed across the flow channels.
7. The heat transfer is assumed to be one dimensional only between the channels and there is no heat exchange in the direction of the fluid flow either by the fluid itself or by the channel wall.
8. The specific heat of fluid at each side is constant throughout the heat exchanger. Hence, the heat capacity rate and number of transfer unit is treated as constant throughout the heat exchanger.

3.4.2 General Assumptions in Pressure Drop Analysis of PHE

1. The fluid flow is hydro dynamically fully develop
2. The fluid flow is uniformly distributed to each flow channel. Therefore, every channel has the equal mass flow rate.
3. The fluid flow is steady and isothermal; hence the fluid properties are independent of time.
4. The friction factor along the flow length is assumed to be constant and equal for every channel.
5. The flow inside the heat exchanger is assumed to be single phase flow. Therefore, the pressure drop due to the flow acceleration is considered negligible.

3.5 Nanofluids Thermophysical Properties Estimation

3.5.1 Nanofluids Thermal Conductivity

The calculation for effective thermal conductivity (k_{nf}) of the nanofluids is base on correlation given by Corcione (2011).

$$k_{nf} = k_f \left[1 + 4.4 Re^{0.4} Pr^{0.66} \left(\frac{T}{T_{fr}} \right)^{10} \left(\frac{k_p}{k_f} \right)^{0.03} \varphi^{0.66} \right] \dots\dots\dots\dots (3.1)$$

Where *Re* is the nanoparticles Reynolds number calculated by

$$Re = \frac{2\rho_f k_b T}{\pi \mu_f^2 d_p} \dots\dots\dots\dots (3.2)$$

In which, ρ_f , μ_f, k_f, Pr and T_{fr} is the density, dynamic viscosity, thermal conductivity, Prandtl number and freezing point of the base fluid respectively. T is the nanofluids temperature; k_p is the thermal conductivity of nanoparticles; φ is the nanoparticles volume fraction; d_p is the nanoparticles diameter and k_b is the Boltmann's constant. This equation is constructed base on the assumption that the nanoparticles are well disperse into the base fluid and the nanoparticles Brownian velocity is calculated base on the ratio between the particle diameter and the time required for a particle to move by a distance equal to its diameter according to (Keblinski, Phillpot, Choi, & Eastman, 2002).

3.5.2 Nanofluids Dynamic Viscosity

Similar to thermal conductivity, the effective dynamic viscosity of nanofluids is estimated base on the correlation given in (Corcione, 2011).

$$\mu_{nf} = \mu_f \left[\frac{1}{1 - 34.87 \left(\frac{d_p}{d_f} \right)^{-0.3} \varphi^{1.03}} \right] \ldots\ldots\ldots\ldots\ldots (3.3)$$

Where d_f is the equivalent diameter of base fluid molecule estimated by

$$d_f = 0.1 \left(\frac{6M}{N\pi\rho_{f0}} \right)^{\frac{1}{3}} \ldots\ldots\ldots\ldots\ldots (3.4)$$

For the equation above, N is the Avogadro number, ρ_{f0} is the density of base fluid at temperature T_0 = 293 K and M is the molecular weight of base fluid.

3.5.3 Nanofluids Density

The nanofluids density ρ_{nf} is calculated base on equation obtained from (Pak & Cho, 1998)

$$\rho_{nf} = \rho_p \varphi + \rho_f (1 - \varphi) \ldots\ldots\ldots\ldots\ldots (3.5)$$

Where ρ_p is the nanoparticle density.

Base on Vajjha et al. (2009), the result of density calculated by this equation presented good agreement with their experimental value and its use in (Vajjha, Das, & Kulkarni, 2010). The same equation was also used by Tsai and Chein (2007), Leong et al. (2010) and Lotfi, Saboohi and Rashidi (2010), in their prediction of nanofluids density.

3.5.4 Nanofluids Specific Heat

In this study, correlation proposed by Xuan and Roetzel (2000) was adopted since it was widely use by researchers to calculate the specific heat.

$$c_{p,nf} = \frac{\varphi \rho_p c_{p,p} + \rho_f c_{p,f}(1-\varphi)}{\rho_{nf}} \ldots\ldots\ldots\ldots\ldots (3.6)$$

Where $c_{p,p}$ and $c_{p,f}$ is the specific heat of nanoparticle and base fluid respectively.

This correlation was use by Tsai and Chein (2007), Duangthongsuk and Wongwises (2008), Vajjha et al. (2010) and Leong et al. (2010).

3.5.5 Nanofluids Prandtl Number

The nanofluids Prandtl number was calculated using equation as below

$$Pr_{nf} = \frac{\mu_{nf} c_{p,nf}}{k_{nf}} \ldots\ldots\ldots\ldots\ldots (3.7)$$

It should be noted that, all the base fluid properties is taken with respect to the average value of inlet and outlet temperature of the hot fluid side.

$$T_{hot,avg} = \frac{T_{hot,i} - T_{hot,o}}{2} \ldots\ldots\ldots\ldots\ldots (3.8)$$

3.6 Performance Analysis of Existing PHE System Uses Nanofluids as Hot Side Working Fluid

In this section, the operating condition of the PHE is maintained and the only thing changing is the hot fluid medium. The hot fluid was changed from fresh water to nanofluids with different particle volume concentration up to 3%.

The thermal and hydrodynamic performances of the PHE are estimated and analyzed base on nanoparticle material, sizes and volume concentration.

3.6.1 Thermal Analysis

3.6.1 (a) Heat Transfer Coefficient of Both Fluid Sides

Since the PHE is operating at its existing conditions. The volumetric flow rate supply to the PHE is assumed to be constant. Therefore, the existing volumetric flow rate can be calculated from the given total mass flow rate of water at hot fluid side base on Equation 3.9,

$$\dot{v} = \frac{\dot{m}_{total}}{\rho_{water}} \cdots\cdots\cdots\cdots (3.9)$$

Base on the constant volumetric flow rate, the total mass flow rate of nanofluid at each nanoparticles volume fraction supplied to the heat exchanger can be estimated by,

$$\dot{m}_{total,nf} = \dot{v} \times \rho_{nf} \cdots\cdots\cdots\cdots (3.10)$$

Then Reynolds number at each channel can be calculated base on equation

$$Re = \frac{\rho u_m D_e}{\mu} \cdots\cdots\cdots\cdots (3.11)$$

Given that

$$\dot{m}_{channel} = \rho u_m A_c \ldots\ldots\ldots\ldots\ldots (3.12)$$

And

$$\dot{m}_{channel} = \frac{\dot{m}_{total}}{N} \ldots\ldots\ldots\ldots\ldots (3.13)$$

Substitute Equation 3.12 into Equation 3.11 it becomes

$$Re = \frac{\dot{m}_{total} \times D_e}{N \times A_c \times \mu} \ldots\ldots\ldots\ldots\ldots (3.14)$$

Where D_e is the equivalent diameter of the channel, N is the number of channels, A_c is the cross sectional area of channel.

The selected correlation to calculate the Nusselt number in this study is from (Muley & Manglik, 1999) since it is able to represent much of the available literature data very well as commended by Wang et al. (2007) and the geometry of the PHE in this study is within the valid range of the equation.

$$Nu = [0.2668 - 0.006967\beta + 7.244 \times 10^{-5}\beta^2] \times [20.78 - 50.94\phi + 41.16\phi^2 - 10.51\phi^3] \times Re^{\left[0.728+0.0543sin\left[\left(\pi\beta/45\right)+3.7\right]\right]} Pr^{1/3} \left(\frac{\mu}{\mu_{wall}}\right)^{0.14} \ldots\ldots (3.15)$$

In the equation above, β represent the plate chevron angle, ϕ is the surface enlargement factor, Pr and μ is the Prandtl number and dynamic viscosity of the fluid and μ_{wall} is the viscosity of the fluid measure at mean wall temperature.

$$T_{wall} = \left(\frac{T_{hot,avg} + T_{cold,avg}}{2}\right) \ldots\ldots\ldots\ldots\ldots (3.16)$$

With the availability of the Nusselt number the heat transfer coefficient is then calculated by equation as below.

$$h = \frac{Nuk}{D_e} \cdots\cdots\cdots\cdots (3.17)$$

3.6.1 (b) Overall Heat Transfer Coefficient

Assuming that the fouling resistance for PHE is negligible (cause by the high degree of turbulence flow in PHE, smooth plate surface and corrosion resistance material use). The overall heat transfer coefficient is estimated by

$$U = \frac{1}{\left(\frac{1}{h_{cold}} + \frac{1}{h_{hot}} + \frac{\delta_{plate}}{k_{plate}}\right)} \cdots\cdots\cdots\cdots (3.18)$$

3.6.1 (c) Heat Capacity Rate and Heat Capacity Rate Ratio

Heat capacity rate of hot and cold side is calculated by equations as below

$$C_{hot} = c_{p,nf} \times \dot{m}_{total,nf} \cdots\cdots\cdots\cdots (3.19)$$

$$C_{cold} = c_{p,cold} \times \dot{m}_{total,cold} \cdots\cdots\cdots\cdots (3.20)$$

Heat capacity rate ratio is calculated by

$$C^* = \frac{C_{min}}{C_{max}} \cdots\cdots\cdots\cdots (3.21)$$

C_{min} is the smaller value of C_{hot} or C_{cold}, while the C_{max} is the larger value of them.

3.6.1 (d) Number of Transfer Unit (NTU)

The NTU of the PHE is estimated by

$$NTU = \frac{UA_{total}}{C_{min}} \cdots\cdots\cdots\cdots (3.22)$$

Where A_{total} is the total effective heat transfer area

$$A_{total} = A_{plate} \times (N_{plate} - 2) \cdots\cdots\cdots\cdots (3.23)$$

A_{plate} is the effective heat transfer area of a thermal plate and N_{plate} is the total number of thermal plates.

3.6.1 (e) Effectiveness of PHE

Since the total number of channels in the current PHE is 25 on each side and the total number of thermal plates is 51. It has greater value compare to the minimum number of channels specified by Zaleski and Klepacka (1992) and minimum number of thermal plates recommended by Kandlikar and Shah (1989).

Therefore, the end plate effect of the current PHE is considered negligible and the PHE can be modeled as a true counterflow heat exchanger. The effectiveness of the PHE is then estimated by the ε-NTU relation for counterflow heat exchanger from (Kays & London, 1984).

$$\varepsilon = \frac{1 - \exp[-NTU(1 - C^*)]}{1 - C^* \exp[-NTU(1 - C^*)]} \qquad for\ (C^* < 1) \cdots\cdots\cdots\cdots (3.24)$$

$$\varepsilon = \frac{NTU}{1 + NTU} \qquad for\ (C^* = 1) \cdots\cdots\cdots\cdots (3.25)$$

3.6.1 (f) Maximum Heat Transfer Rate

From (Incropera & DeWitt, 2002) the maximum heat transfer rate can be achieved when one of the fluids experiences the maximum possible temperature difference. Hence, a general expression as below was made

$$q_{max} = C_{min}\left(T_{hot,i} - T_{cold,i}\right) \cdots\cdots\cdots\cdots (3.26)$$

3.6.1 (g) Actual Heat Transfer Rate of PHE

The actual heat transfer rate of the PHE is computed from equation below

$$q = \varepsilon q_{max} \cdots\cdots\cdots\cdots (3.27)$$

3.6.2 Pressure Drop Analysis

The total pressure drop of PHE consists of;

1. Pressure drop within the flow channel due to frictional losses,
2. Pressure drop associate with the inlet and outlet manifolds and ports
3. Pressure drop due to elevation change of the flow.

The total pressure drop of the system can be calculated by the equation as below.

$$\Delta p_{total} = \Delta p_{channel} + \Delta p_{port} + \Delta p_{elevation} \cdots\cdots\cdots\cdots (3.28)$$

3.6.2 (a) Channels Pressure Drop

The frictional pressure drop is estimated from equation stated in (White, 1999)

$$\Delta p_{channel} = \frac{2fLG^2}{D_e\rho} = \frac{2fL\left(\frac{\dot{m}_{total}}{NA_c}\right)^2}{D_e\rho} \ldots\ldots\ldots\ldots (3.29)$$

Where, L is the vertical distance between 2 ports center, G is the mass velocity and f is the friction factor calculated by correlation recommended by Muley and Manglik (1999).

$$f = [2.917 - 0.1277\beta + 2.016 \times 10^{-3}\beta^2] \times [5.474 - 19.02\phi + 18.93\phi^2 - 5.341\phi^3] \times Re^{-\left[0.2+0.0577sin\left[\left(\pi\beta/45\right)+2.1\right]\right]} \ldots\ldots\ldots\ldots (3.30)$$

3.6.2 (b) Ports and Manifolds Pressure Drop

Base on (Kays, 1950; Kays & London, 1984; Shah & Focke, 1988); Muley and Manglik (1999) used equation below to estimate the port losses in his study.

$$\Delta p_{port} = 1.5\left(\frac{\rho V_{port}^2}{2}\right) \ldots\ldots\ldots\ldots (3.31)$$

Where V_{port} = mean port velocity. With Equation 3.12 and 3.13, the port pressure drop become

$$\Delta p_{port} = \frac{1.5\rho\left(\frac{\dot{m}_{total}}{\rho A_{port}}\right)^2}{2} = \frac{1.5\left(\frac{4\dot{m}_{total}}{\pi D_{port}^2}\right)^2}{2\rho} \ldots\ldots\ldots\ldots (3.32)$$

Where D_{port} is the internal diameter of port

3.6.2 (c) Pressure Drop due to Elevation Change

Elevation pressure drop can be calculated by

$$\Delta p_{elevation} = \pm \rho g L \cdots\cdots\cdots\cdots (3.33)$$

Here, the positive value of the pressure drop is use when the flow in the channel is vertical up flow and negative value is taken when the flow is vertically downward. In this study, since the direction of flow is downward. Therefore, the negative value of elevation pressure drop is taken.

3.7 Application of Nanofluids in PHE Design

3.7.1 Heat Transfer Area Reduction Estimation

Here, the heat transfer area require in achieving the given heat transfer rate (460kW) at desired NTU value and corresponding pressure drop are calculated. The effects from the nanoparticle material, sizes and volume concentration are also examined.

Apart from the general assumptions for thermal analysis shown in previous section, the area reduction calculation is based on assumptions as below;

1. The PHE design is base on equal heat capacity for both side i.e.

$$C_{hot} = C_{cold} = C_{min} = C_{max};\ C^* = 1 \cdots\cdots\cdots\cdots (3.34)$$

2. The flow rate at cold side is fixed at the value given. While the flow rate at hot side is adjusted to match the heat capacity rate of cold side when the nanoparticles volume concentration is increase.
3. The effectiveness of the PHE is estimated base on ε-NTU relation for a true counterflow heat exchanger.

4. The PHE design is base on the heat transfer rate required by the existing PHE and desire value of NTU from 1 to 5.
5. The working temperature of the PHE is maintained and therefore the thermophysical properties of the nanofluids from previous section can be applied.
6. The general geometry of the PHE is similar to the existing one except the dimension related to the effective plate area. In order to have the same channel cross sectional area, the effective width of the plate is remains, which mean only the port length of the PHE is changing.

To calculate required heat transfer area at desire NTU

Step 1: Estimation of PHE effectiveness

The effectiveness of the PHE base on desire NTU is calculated base on Equation 3.25 from previous section.

Step 2: Estimation of required heat capacity rate

The heat capacity rate of the fluid is calculated by

$$C_{min} = \frac{q}{\varepsilon\left(T_{hot,i} - T_{cold,i}\right)} \dots\dots\dots\dots (3.35)$$

Step 3: Estimation of required mass flow rate and mass flow rate at each channel

Required mass flow rate to achieve desire C_{min} is calculated from

$$\dot{m}_{total} = \frac{C_{min}}{c_p} \dots\dots\dots\dots (3.36)$$

And the mass flow rate at each channel is calculated from Equation 3.13

Step 4: Estimation of Reynolds number

The Reynolds number is estimated from equation as below

$$Re = \frac{\dot{m}_{channel} \times D_e}{A_c \times \mu} \ldots\ldots\ldots\ldots (3.37)$$

Step 5: Estimation of Nusselt number and convective heat transfer coefficient of working fluids

The calculation of the Nusselt number is done with using Equation 3.15. While the convective heat transfer coefficient is calculated by Equation 3.17.

Step 6: Overall heat transfer coefficient

After the values of convective heat transfer coefficient for both side of fluid is calculated. The overall heat transfer coefficient is then estimated from Equation 3.18.

Step 7: Required Heat transfer area for respected NTU

The heat transfer area required to achieve the rated heat transfer rate of 460kW with respect to the desire NTU value is estimated from

$$A_{required} = \frac{NTU \times C_{min}}{U} \ldots\ldots\ldots\ldots (3.38)$$

3.7.2 Pressure Drop Estimation from Desire NTU

The value of NTU is directly associated with the pressure drop due to the larger the NTU desire, the more heat transfer area is require and the thermal plate area is directly related to the frictional losses in the flow channel.

With the available of channel Reynolds number calculated from Equation 3.37 the pressure drop can be estimated from using equations shown in previous section. However, from the assumptions that the numbers and the effective width of thermal plate is same as the existing PHE, the value of L in Equation 3.29 and 3.33 should be calculated from

$$L = \frac{A_{required}}{\left(N_{plate} - 2\right) \times w} \cdots\cdots\cdots\cdots (3.39)$$

Where w is the effective width of thermal plates

3.8 Validation of Correlations and Mathematical Formulation

In this study, the most important parameter of the nanofluids is the effective thermal conductivity. Correlation selected to predict the nanofluids thermal conductivity is from (Corcione, 2011). Since this correlation is constructed base on various numbers of experimental data from year 1993 to 2009, it raises concern that those experimental devices and setups in the earlier date are not technologically advance enough to have a more accurate measurement. Therefore, to validate this correlation, nanofluids thermal conductivity estimated from correlation by Vajjha and Das (2009a) which is not considered in Corcione (2011) study was use to make comparison.

For comparison, the Al_2O_3 nanofluids thermal conductivity is estimated base on mean temperature of the hot side fluid in the existing PHE and it is plotted in graph as shown in Figure 3.4.

The maximum deviation from them is about 5% at particle volume concentration of 0.5%. Therefore, it shows that both correlation posses good agreement to each other in the estimation of nanofluids thermal conductivity.

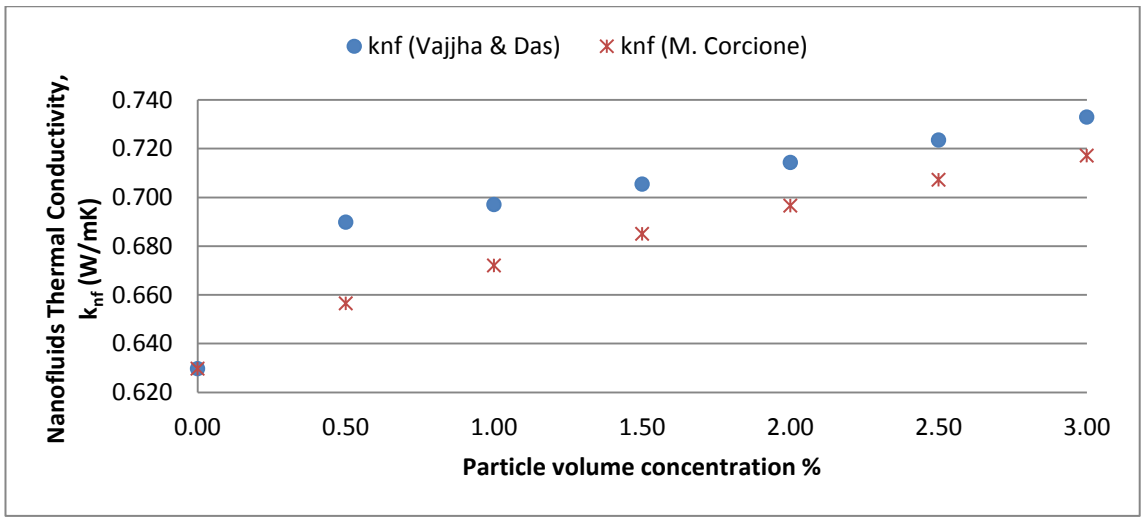

Figure 3.4: Comparison of k_{nf} from (Corcione, 2011; Vajjha & Das, 2009a)

To validate the mathematical formulation shown in above section, the calculated performance details of PHE are compared to the value rated by the manufacturer and they are shown in Table 3.6

Table 3.6: Comparison of Performance Details

PHE Performance Detail	Rated	Calculated	Deviation
Overall heat transfer coefficient, U (W/m^2K)	5475	5403.41	1.31%
Heat transfer rate, q (W)	460,000	460,743.57	0.16%
Total pressure drop, Δp_{total} (Pa)	34,548	31,587.65	8.57%

The comparison shows that the calculated overall heat transfer coefficient and heat transfer rate is well agreed to the rated value. Both have only 1.31% and 0.16% deviation respectively. Therefore, it can be concluded that the selected correlation to calculate the Nusselt number, the assumptions in thermal analysis, the use of ε-NTU relation for counterflow heat exchanger and the calculation steps are valid.

Meanwhile, for pressure drop, the difference is larger but it is still below 10%. This might be caused by; (1) the different parameters used in the calculation i.e. the friction factor, manufacturers always uses their own correlations based on the testing of their product. The correlation used in this study is valid for general geometry of PHE and it is not a specific one for the existing PHE. (2) The calculated value is base on idealized situation. In actual case, there might have flow recirculation at the edge of ports and manifold that increases the pressure drop.

Since the percent difference of rated and calculated pressure drop is only 8.57% and together with the reasons discuss above. It can be concluded that the assumptions and mathematical formulation for pressure drop calculation are applicable.

4.0 RESULTS AND DISCUSSION

4.1 Introduction

In this chapter, the calculated results will be shown and analyzed. In first section, the calculated thermophysical properties will be analyzed based on particle volume concentration and size. In addition, the comparison will be made between Al_2O_3-H_2O and SiO_2-H_2O nanofluids. After that, the thermal and hydrodynamic performance of existing PHE system operating with nanofluids as hot side working fluid instead of water will be discussed. Comparison of performance between nanofluids and the original heat transfer fluid as well as different type of nanofluids will be revealed. The efficacy of using nanofluids as working fluid in the designing stage of the PHE system will be analyzed in third section. In this section, the heat transfer area reduction with respect to desire NTU value will be estimated and corresponding pressure drop will be investigated.

4.2 Thermophysical Properties of Nanofluids

4.2.1 Thermal Conductivity

Effective thermal conductivity of nanofluids are plotted in Figure 4.1. It is found that at mean hot side working temperature T = 311.5K, the thermal conductivity of nanofluids increase as particle volume concentration increase and as the particle size decrease. Comparing to the base fluid, the thermal conductivity at 3% particle volume concentration is 13.88% higher for Al_2O_3 nanofluids, while for SiO_2 nanofluids an enhancement of 9.15%, 12.07% and 15.93% is observed for nanoparticles size of 100 nm, 50 nm and 25 nm respectively. Figure 4.1 clearly shows that the thermal conductivity of Al_2O_3 nanofluids at every particle volume

concentration is lower than SiO_2 nanofluids with 25 nm particle size although the thermal conductivity of Al_2O_3 particle is 26 times higher than SiO_2 particle. The effect of particle material only can be notice when comparing the Al_2O_3 nanofluids to SiO_2 nanofluids with 50 nm, noting that particle size for Al_2O_3 is 45 nm. This phenomenon indicates that at a fix temperature, the thermal conductivity of nanofluids is strongly dependent on the particle volume concentration and particle size while the effect of the thermal conductivity of particles is minimal. Similar observation was revealed by Jang and Choi (2007), they found that the thermal conductivity of nanofluids depends strongly on temperature, particle size and volume fraction while the effect of ratio between particle and base fluid thermal conductivity is small, which also means that the effect of particle thermal conductivity is weak.

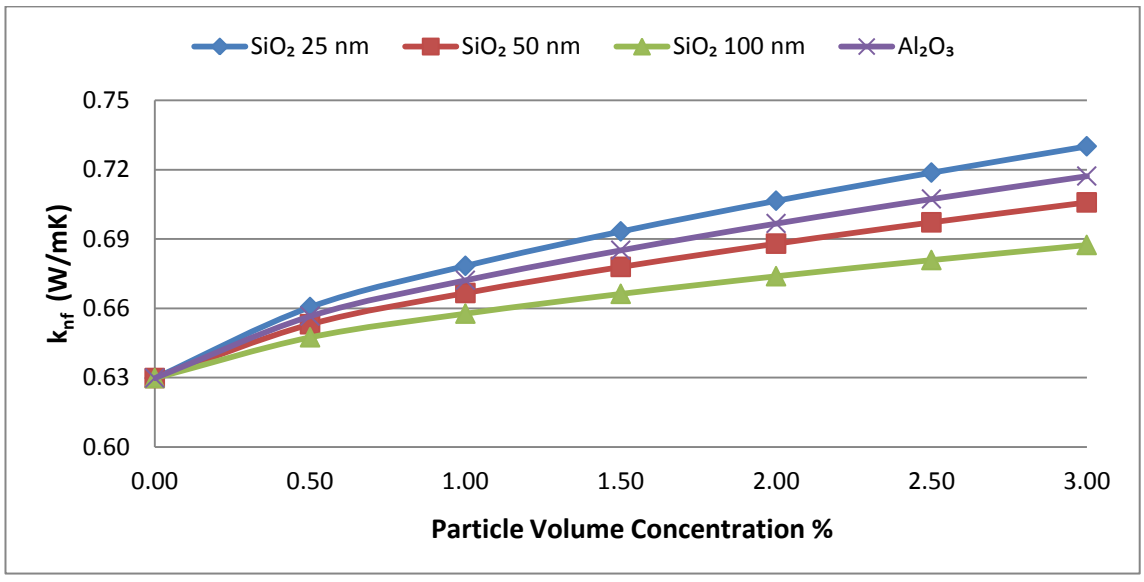

Figure 4.1: Thermal Conductivity of Nanofluids at Different Particle Volume Concentration.

The explanations for this occurrence are; (1) the thermal conductivity of nanofluids not only depends on the static part of thermal conductivity i.e. thermal conductivity of particle and base fluid and particle volume fraction. Particle Brownian motion also plays an important part in thermal conductivity enhancement; there will be more collision of particles due to Brownian motions at a given volumetric concentration for smaller particle size because the amount of nanoparticles is greater. The collisions provide thermal diffusion of nanoparticles that indicate heat transfer between particles. (2) At the same particle volume concentration, nanofluids with smaller particles size will have larger amount of particles and hence there will be more surface area for transfer of thermal energy. (3) Collision of particles and fluid molecules due to Brownian motion with short wavelength by thermal induce fluctuation or termed as nanoconvection (Jang & Choi, 2007). As the particles size decrease the Brownian motion is greater and hence the nanoconvection become dominant. Consequently, the nanofluids thermal conductivity increase.

4.2.2 Viscosity

The calculated effective dynamic viscosity for each nanofluids are plotted in Figure 4.2. It shows that the viscosity of nanofluids increased as the particle volume concentration increase. Results shows that at 3% particle volume concentration, Al_2O_3 nanofluids and SiO_2 nanofluids with particle size 25, 50 and 100 nm respectively exhibits 12.77%, 15.61%, 12.32% and 9.78% increment over base fluids. From the figure, it is also notice that the effect of particle size to viscosity is dependent on particle volume concentration. At high particle volume concentration, the smaller the particle size the higher the

viscosity will be. This is due to when particle size is small, there will be larger amount of particles in the nanofluids at a given volume fraction compare to nanofluids with bigger particle size. Therefore, the total particle surface area interacting with the base fluid is larger. However, at low particle volume concentration, the effect of particle size is not significant. This might be due to the fact that the amount of nanoparticles is not significant enough to provide the aforementioned effect.

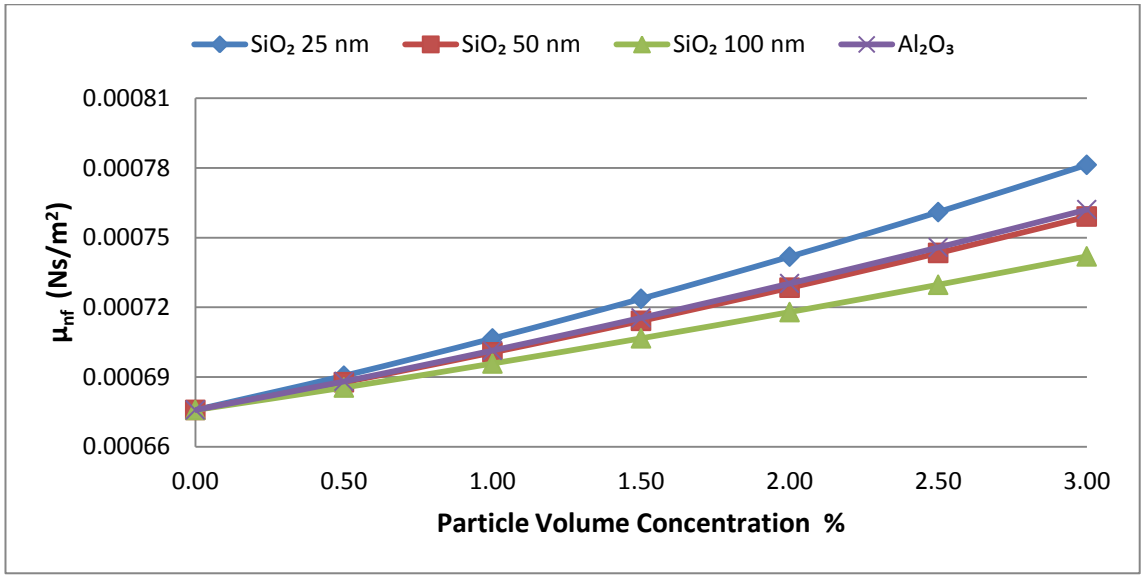

Figure 4.2: Viscosity of Nanofluids at Different Particle Volume Concentration

4.2.3 Density

The calculated results show that density of nanofluids increased with increase of particle volume concentration. For Al_2O_3 nanofluids at 3% volume fraction, the density increased by 9% compare to the base fluid. Meanwhile, at the same particle volume concentration, SiO_2 particles with lower density compare to Al_2O_3 exhibit 3.71% increase on viscosity compare to base fluid. The relation of

nanofluids density to the particle volume concentration and density of nanoparticles are shown in Figure 4.3.

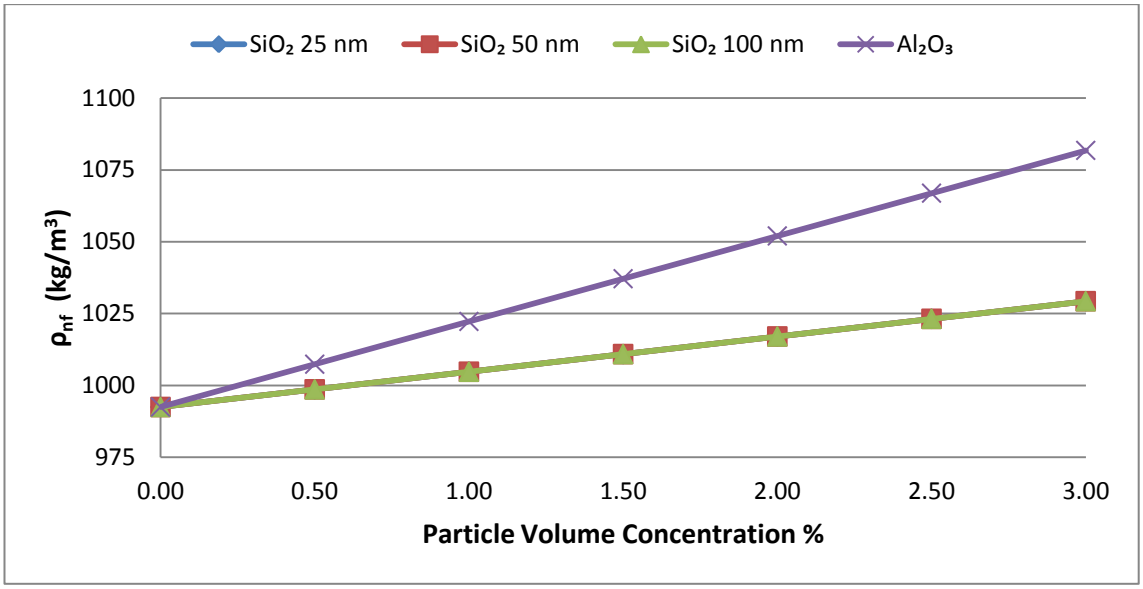

Figure 4.3: Density of Nanofluids at Different Particle Volume Concentration

4.2.4 Specific Heat

The calculated results are plotted in graph as shown in Figure 4.4. It is observed that the specific heat decreased as particle volume concentration increase. At 3% particle volume concentration, the Al_2O_3 nanofluids posses 8.99% lower specific heat compare to the base fluid while SiO_2 exhibits 5.32% lower specific heat. Similar to that of density, the specific heat of nanofluids depends on the volume fraction and the specific heat as well as density of nanoparticle.

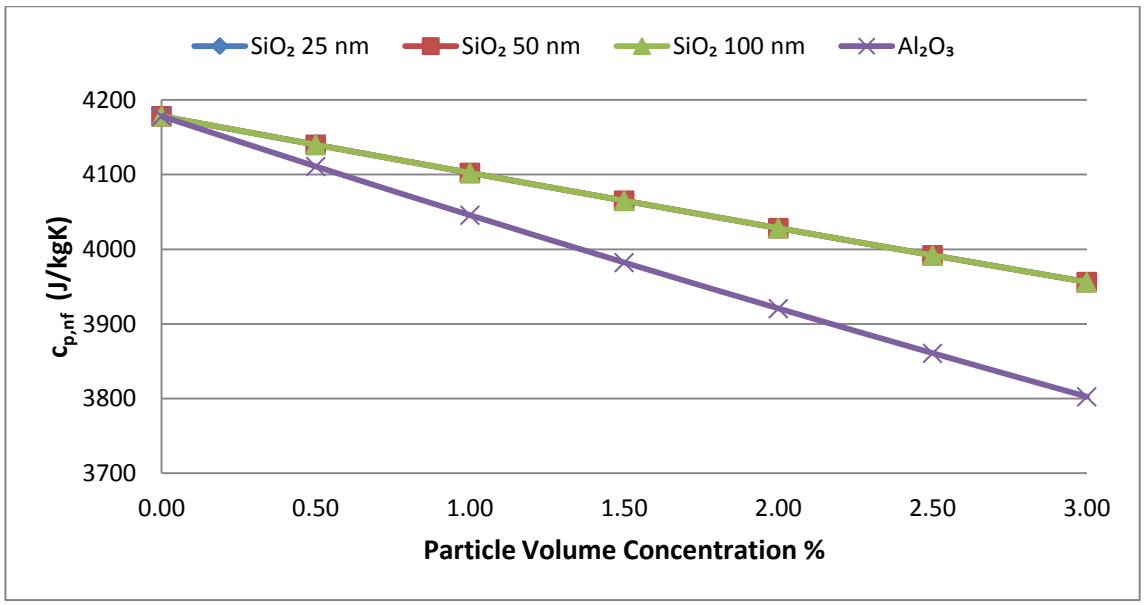

Figure 4.4: Specific Heat of Nanofluids at Different Particle Volume Concentration

4.2.5 Prandtl Number

Prandtl number is a function of thermal conductivity, viscosity and specific heat. Figure 4.5 shows the Prandtl number with respect to particle volume concentration. It shows that the Prandtl number of Al_2O_3 nanofluids is more sensitive to increase of particle volume concentration. Comparing to base fluid the Al_2O_3 nanofluids at 3% particle volume concentration exhibit 9.89% drop in Prandtl number. At the same volume fraction, SiO_2 nanofluids posses 4.48%, 5.11% and 5.57% drop in Prandtl number for particle size of 100 nm, 50 nm and 25 nm respectively.

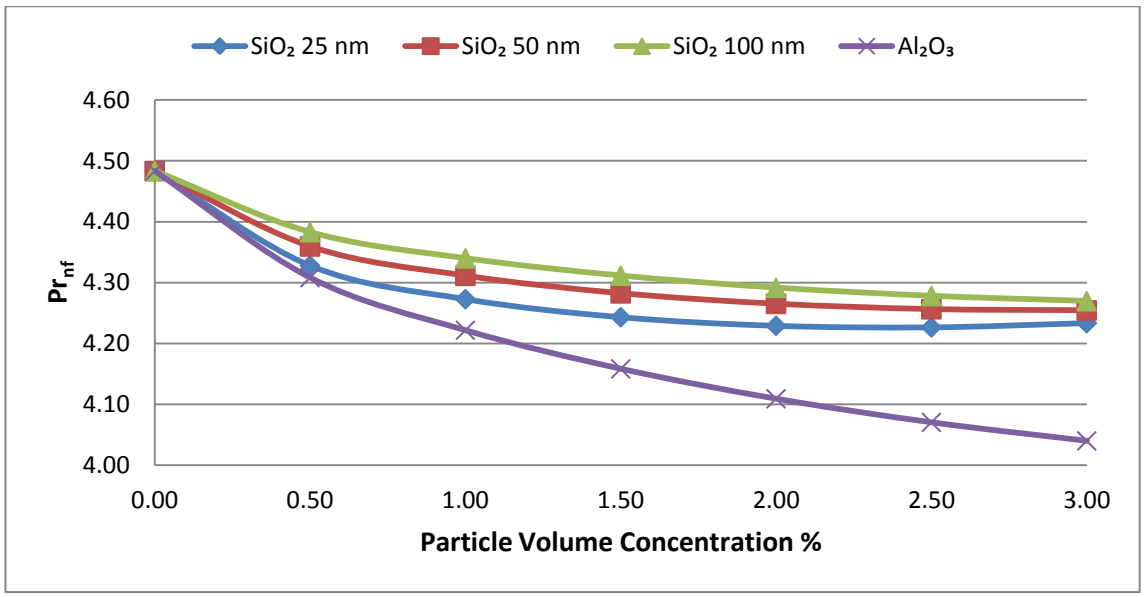

Figure 4.5: Prandtl Number of Nanofluids at Different Particle Volume Concentration

4.3 Thermal and Hydrodynamic Performance of Existing PHE System Operating With Nanofluids as Hot Side Working Fluid

4.3.1 Thermal Performance Analysis

The original volumetric flow rate of hot side fluid calculated from Equation 3.9 is 0.02239 m^3/s. This value was treated as constant throughout the whole analysis as the pump system does not change. Hence, total mass flow rate of the nanofluids supplied to the PHE can be calculated using Equation 3.10. Due to the increase in density of nanofluids with respect to the particle volume concentration, the mass flow rate of nanofluids increased with particle volume concentration. At 3% particles volume concentration, 9% increment on mass flow rate is observed for Al_2O_3 nanofluids while for SiO_2 nanofluids the increment is 3.71% independent of nanoparticle size. An explanation to this occurrence is that when volume concentration increases, the amount of the particles inside the fluids increase and resulting the rise of nanofluids density.

From Figure 4.6, it is observed that the trend of mass flow rate is similar to that of density shown in Figure 4.3; this is mainly due to the mass flow rate that is only dependent to density when the volumetric flow rate is kept constant.

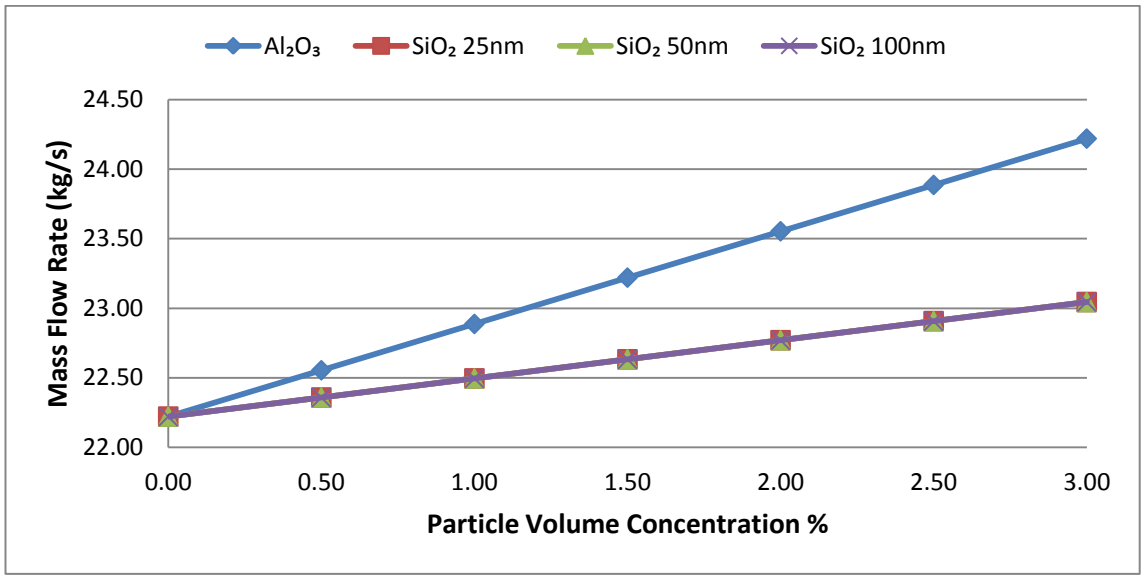

Figure 4.6: Mass Flow Rate of Nanofluids with Respect to Particle Volume Concentration.

The calculated Reynolds number for nanofluids flow in each channel is plotted in graph as shown in Figure 4.7. With the equivalent diameter and the cross sectional area of flow channel remain constant, the Reynolds number is only dependent on the mass flow rate and the nanofluids viscosity. Figure 4.7 shows that Reynolds number for nanofluids is decreasing with particle volume concentration. Analysis on the relationship between the parameters revealed that the increase of viscosity over particle volume concentration is greater than the increased of density thus the Reynolds number drop. At 3% particles volume concentration, the decrease of nanofluids Reynolds number compare to the original fluid (water) is 3.34% for Al_2O_3 and 10.29%, 7.67% and 5.53% for SiO_2 with particle size of 25 nm, 50 nm and 100 nm respectively. Therefore, it shows

that for the same nanoparticles material, the smaller particle size will have lower Reynolds number.

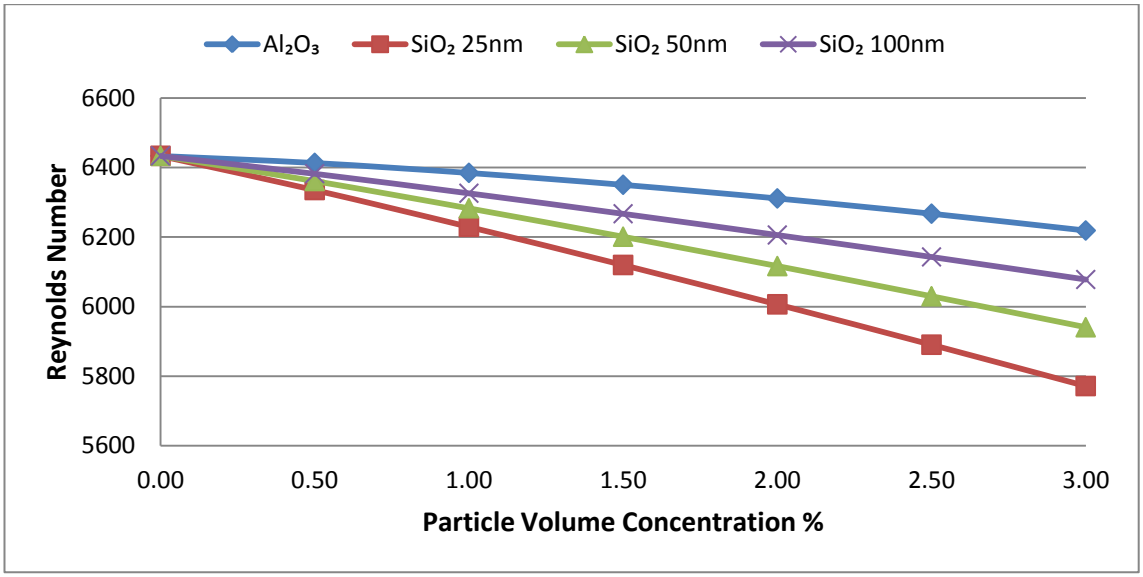

Figure 4.7: Reynolds Number for Different Particle Volume Concentration.

With the available of Reynolds number, Prandtl number and viscosity of nanofluids at fluid temperature and thermal plate temperature, the calculated Nusselt number are plotted in the graph as Figure 4.8.

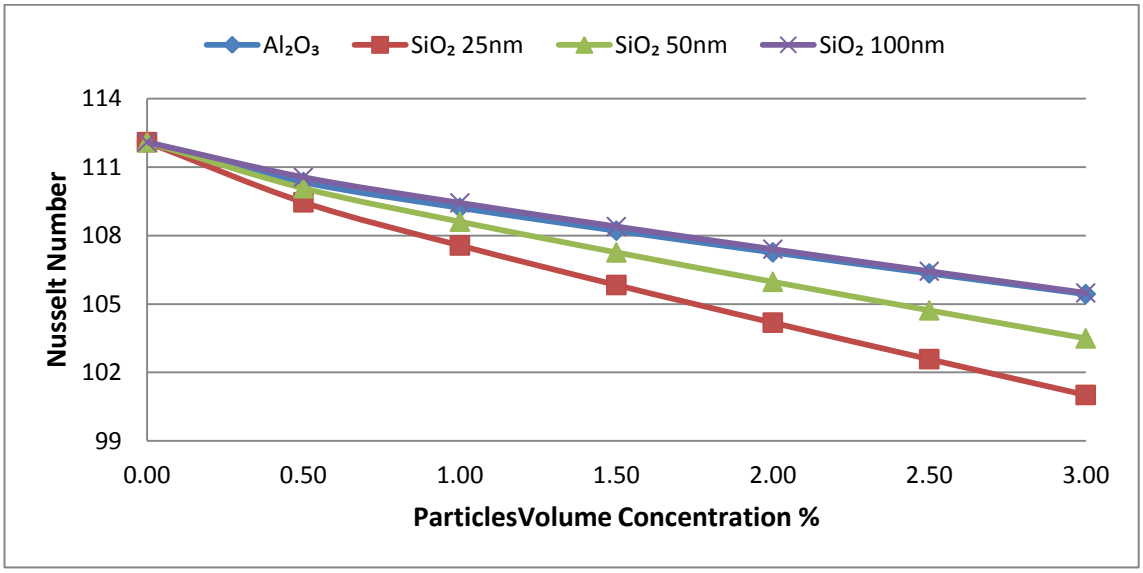

Figure 4.8: Nusselt Number of Nanofluids at Various Particle Volume Concentration.

It is observed that the SiO_2 nanofluids with 100 nm in particle size have Nusselt number similar to the Al_2O_3 while SiO_2 nanofluids made of 25 nm particle size has the lowest Nusselt number. At 3% particle volume concentration, comparison between Al_2O_3 and SiO_2 nanofluids with 100 nm particle size shows that the Reynolds number for Al_2O_3 is higher by about 2.3% while the Prandtl number is 5.68% lower. However, the tradeoff between these two parameters consequently made them to have similar value of Nusselt number. Meanwhile, for SiO_2 nanofluids with particles size of 25 nm, it has lowest Reynolds number which is cause by high viscosity value. The Reynolds number is 7.2% lower than Al_2O_3 nanofluids. Although it has about 5% higher Prandtl number compare to the former, the calculated Nusselt number still lower than Al_2O_3 nanofluids. Thus, it shows that Reynolds number is an important factor in Nusselt number estimation. An investigation on the Nusselt number correlation shows that, with the geometrical characteristic of PHE unchanged, the Reynolds number with exponent value of 0.782 has the highest impact on the Nusselt number followed by Prandtl number with value of 0.333 and lastly the ratio of nanofuids viscosity at bulk fluid temperature and thermal plate temperature with value of 0.14. It is also notice that the viscosity ratio is a constant with a value of 0.96 regardless of type and size of nanoparticles. This can be explained by the correlation of viscosity that is only dependent on particles size and the effect of temperature only shows on the viscosity of base fluid. With this, the ratio of nanofluids viscosity at two different temperatures is same as the viscosity ratio of water. In comparison to water, the drop in Nusselt number cause by nanofluids is 5.94% for Al_2O_3, 9.89%, 7.67% and 5.90% for SiO_2 nanofluids with 25 nm, 50 nm and 100 nm particle size respectively.

The convective heat transfer coefficient for the nanofluids is estimated by using Equation 3.17 and the results are plotted in graph as shown in Figure 4.9. It shows that the convective heat transfer coefficient for Al_2O_3 is the highest follow by SiO_2 nanofluids with particle size of 25 nm, 50 nm and 100 nm respectively. Compare to water, Al_2O_3 nanofluids posses 2.63% enhancement at 0.5% particles volume concentration, while 7.11% enhancement is observed at 3% particle volume concentration. At low particle volume fraction, the enhancement in convective heat transfer coefficient due to types of nanofluids is not obvious. However, at high particle volume concentration, the effect from types of nanofluids is significant. Take for example, at 0.5% particle volume concentration, the difference between Al_2O_3 nanofluids and SiO_2 nanofluid at 25 nm particle size is 24.86 W/m^{2}K, while the difference become 311.80 W/m^{2}K at 3% particle volume concentration.

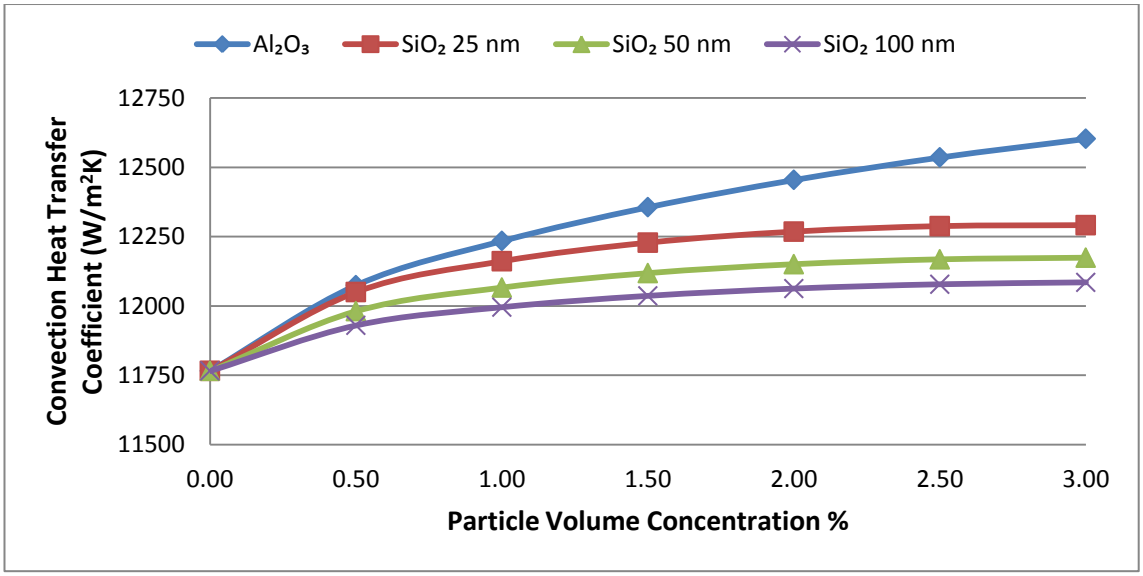

Figure 4.9 Convective Heat Transfer Coefficient of Nanofluids at Different Particle Volume Concentration.

Investigation on Equation 3.17 found that, with constant in equivalent diameter, the convective heat transfer coefficient is dependent on both Nusselt number and thermal conductivity of nanofluids. Hence, the thermal conductivity plays the essential role in determine the enhancement of convection heat transfer coefficient, when the Nusselt number decrease with particle volume concentration. Meanwhile, the effect of particle size to the convective heat transfer coefficient is also noticeable. For SiO_2 nanofluids with particles size of 100 nm, although the Nusselt number is higher than both 25nm and 50 nm one, the calculated results is lowest at every particle volume concentration. This indicates that, SiO_2 nanofluids with smaller particle size which has greater thermal conductivity posses greater convective heat transfer coefficient. Similar finding was reported by Nguyen et al. (2007).

The aforementioned findings demonstrated that the thermal conductivity of nanofluids dominate the enhancement of convective heat transfer coefficient.

To obtain the overall heat transfer coefficient, the thermal plate wall resistance and convection heat transfer coefficient for cold side working fluids was calculated. The wall resistance of the titanium thermal plate is 0.00002283 m^2K/W, while the cold side convection heat transfer coefficient is 12945.64 W/m^2K. Noted that the thickness of the thermal plate is fix and the cold side condition unchanged, these two values will remain constant throughout the calculation. Therefore, the only parameter affecting the overall heat transfer coefficient is hot side convection heat transfer coefficient. Base on Equation 3.18, the calculated results are plotted in graph as Figure 4.10. The results shows that maximum enhancement of heat transfer coefficient occur at 3% particle volume concentration for all nanofluids. Al_2O_3 nanofluids has heat transfer coefficient enhancement of 170.02 W/m^2K or 3.15% increment over original

value, while for SiO_2 nanofluids, the enhancement are 108.18 W/m^{2}K (2%), 84.49 W/m^{2}K (1.56%) and 66.30 W/m^{2}K (1.23%) for particle size of 25 nm, 50 nm and 100 nm respectively. Figure 4.10 also shows that the slop of Al_2O_3 nanofluids is steeper than SiO_2 nanofluids at 3% particle volume concentration; this indicated that higher overall heat transfer coefficient can be expected beyond this limit. However, for SiO_2 nanofluid there will be little or no further enhancement after 3% particle volume concentration.

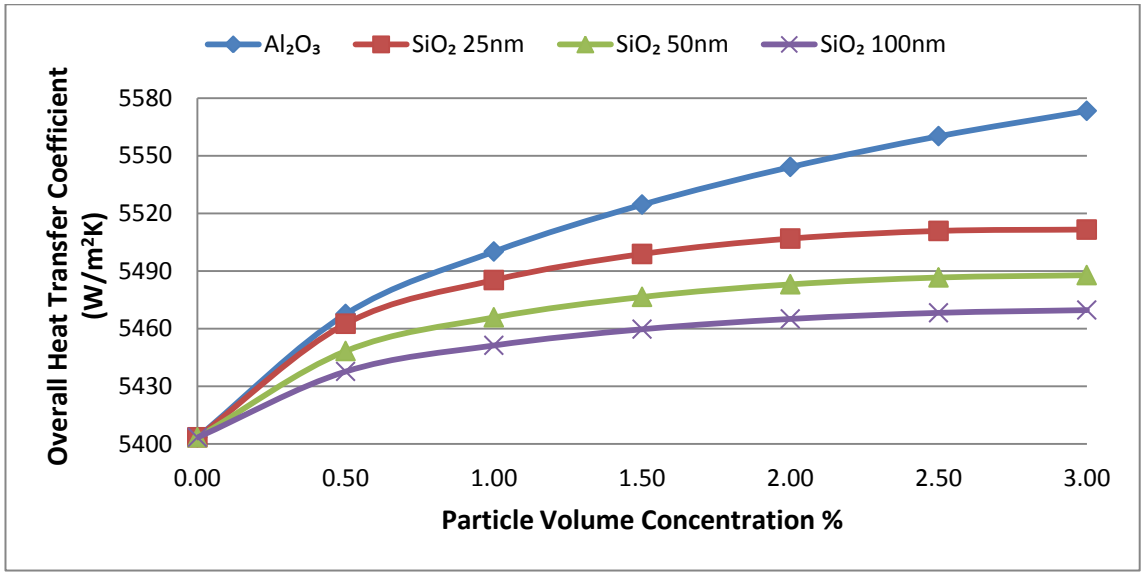

Figure 4.10: Overall Heat Transfer Coefficient of Nanofluids at Different Particle Volume Concentration

Nanofluids heat capacity rate is calculated base on Equation 3.19, the results are plotted in graph as shown in Figure 4.11. The value of heat capacity rate is dependent on both mass flow rate and specific heat of nanofluids. From the figure, it shows that the heat capacity rate decrease with addition nanoparticles into base fluid. This is logic since the increase of particle volume fraction causes increase of thermal conductivity and decrease of thermal resistivity. For 3% Al_2O_3 nanofluids, the heat capacity rate decreased by 0.8% compare to water, while 1.80% drops of heat capacity rate for SiO_2 nanofluids is

observed at the same particle volume concentration. Meanwhile, the calculated heat capacity rate for cold side is 112,802.27 W/K and it remains constant throughout the calculation. Therefore, the minimum heat capacity rate will always belong to the nanofluids side and this will in turn affect the heat transfer rate of PHE.

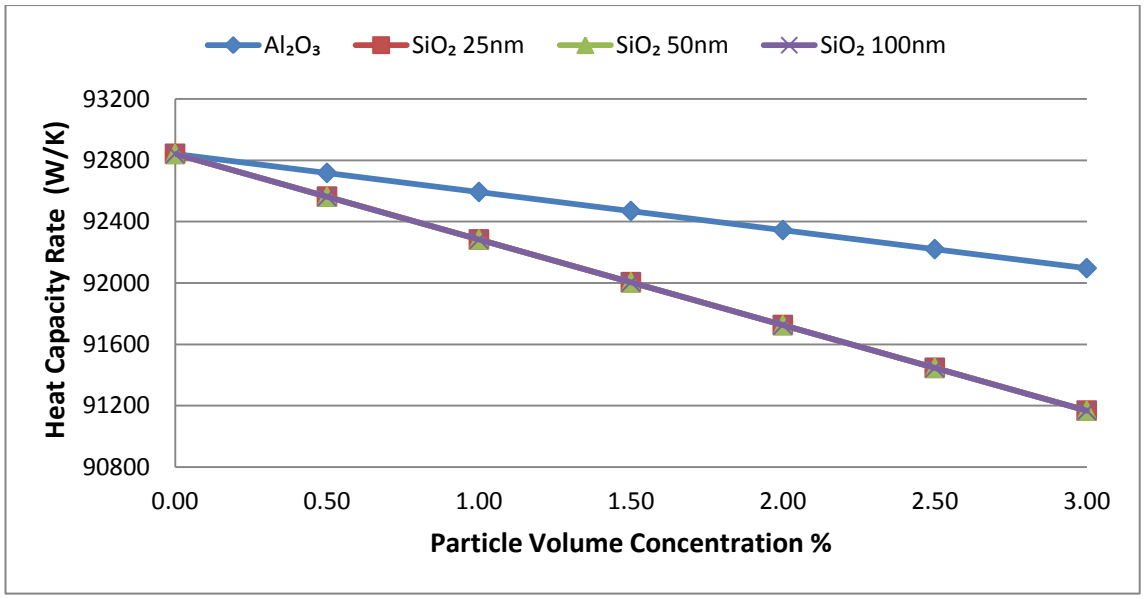

Figure 4.11: Heat Capacity Rate of Nanofluids at Various Particle Volume Concentration

The abovementioned condition is clearly shown in the calculation for maximum heat transfer rate of the PHE. As shown in Figure 4.12, the maximum heat transfer rate of PHE is decreasing with increased of particle volume concentration. It is found that, the magnitude of decrease for maximum heat transfer rate is same to that of heat capacity rate for nanofluids.

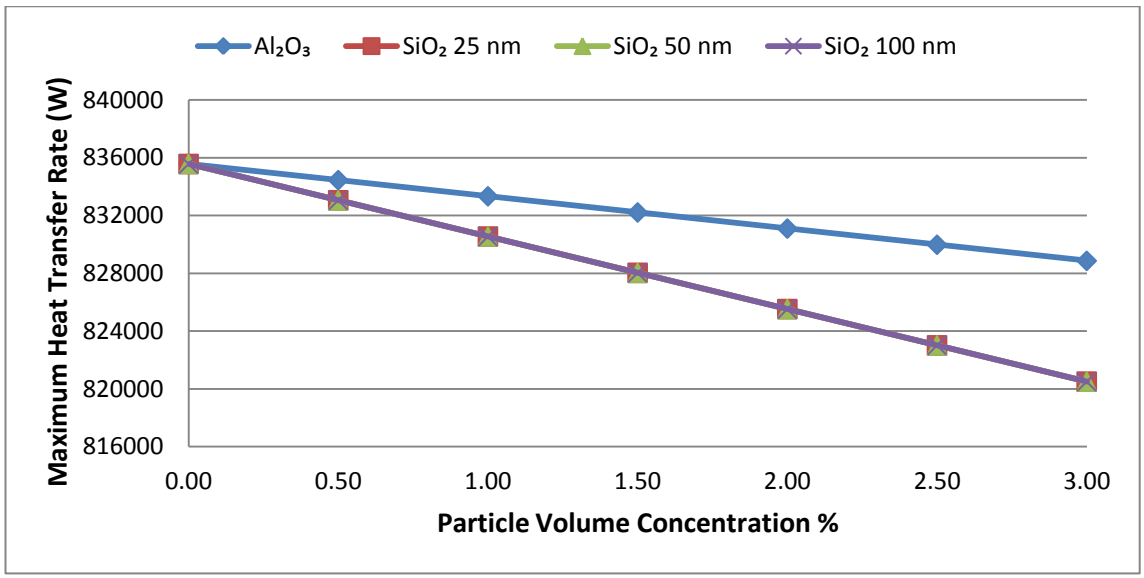

Figure 4.12: Maximum Heat Transfer Rate at Various Particle Volume Concentration

NTU is calculated base on Equation 3.22, with total heat transfer area remains constant, the NTU is dependent on both the overall heat transfer coefficient and the minimum heat capacity rate. The estimated NTU with respect to particle volume fraction is shown in Figure 4.13. It is found that the trend of Al_2O_3 and SiO_2-25 nm nanofluids are almost similar, both at the higher edge on graph followed by SiO_2-50 nm and SiO_2-100 nm nanofluids. At 3% volume concentration, the NTU for Al_2O_3 increase by 8.03% followed by SiO_2-25 nm 7.82%, 6.92%, and 6.22% for SiO_2 nanofluids with 50 nm and 100 nm particle size respectively. This situation further indicated the importance of enhancement on thermal conductivity by nanofluids.

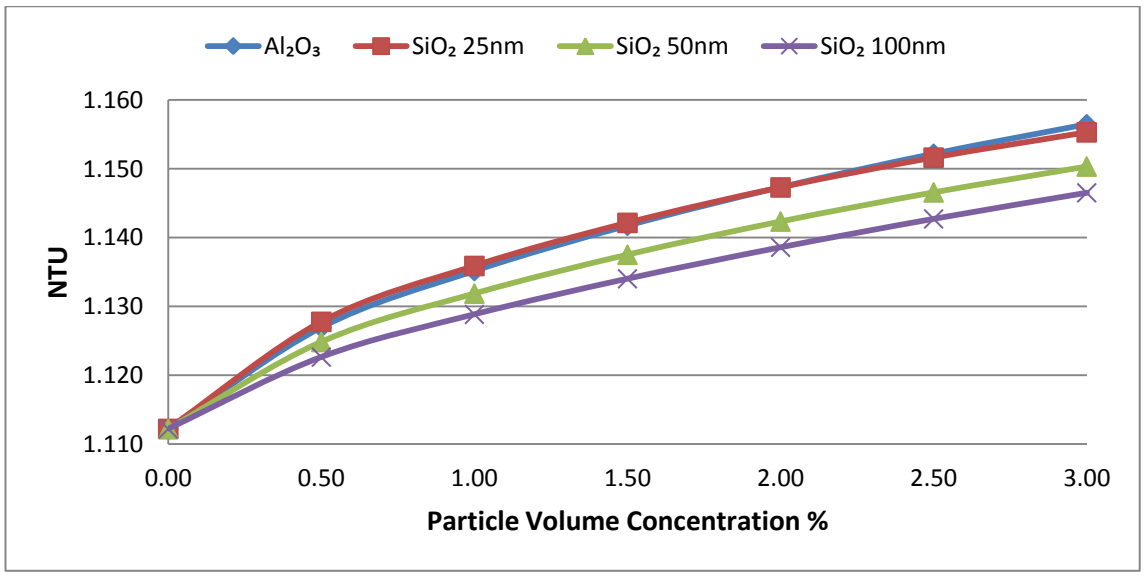

Figure 4.13: NTU of PHE at Different Nanofluids Particle Volume Concentration

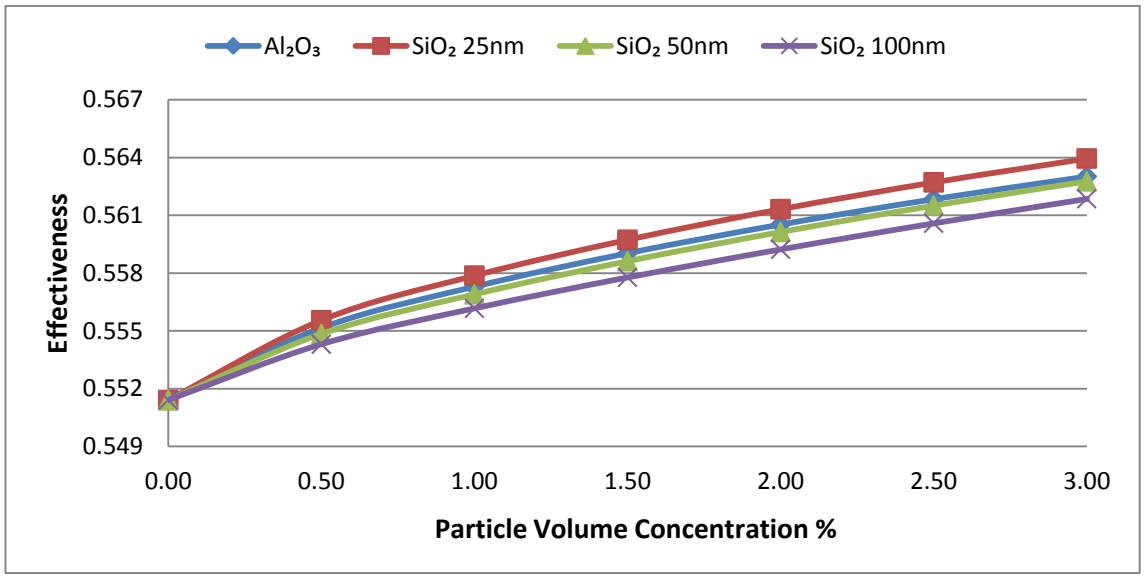

Figure 4.14: Effectiveness of PHE at Different Nanofluids Particle Volume Concentration

The effectiveness of PHE is calculated base on Equation 3.24, since the heat capacity rate ratio is always lesser than 1. The estimated effectiveness is plotted in graph as shown in Figure 4.14. It is noticed that SiO_2-25 nm nanofluids augmented the effectiveness of PHE the most. At 3% particle volume concentration, the SiO_2-25 nm increase the effectiveness by 2.27% followed by Al_2O_3 2.10% and 2.06%, 1.89% for SiO_2 nanofluids with 50 nm and 100 nm particle size respectively. The analysis on the results shows that, the minimum heat capacity rate plays a key role in the effectiveness, which is why the enhancement of effectiveness due to Al_2O_3 is smaller than SiO_2-25 nm nanofluids. Take for example, at 2% particle volume concentration, where both nanofluids has the similar NTU value, the higher heat capacity rate value of Al_2O_3 nanofluids result in high heat capacity rate ratio hence causing lower effectiveness. This phenomenon is clearly shown in Figure 2.3.

The actual heat transfer rate of the PHE system is calculated by Equation 3.27 and shown in Figure 4.15. The results show that Al_2O_3 nanofluids at 3% particle volume concentration has heat transfer rate of 466,664.45 W which represent 1.29% enhancement over original heat transfer rate. Reverse calculation shows that, this amount of enhancement will reduce the hot side volumetric flow rate by 2.66% if the PHE is operated to handle the original heat duty. Moreover, the improvement of heat transfer rate by Al_2O_3 nanofluids beyond 3% particle volume concentration is expected as it has not reach the maximum achievable value. Meanwhile, for SiO_2 nanofluids, the maximum enhancement occur at 1.5% particle volume concentration for nanofluids with 25 nm and 50 nm particle size, while for 100 nm one the heat transfer enhancement stop at 1% particle volume fraction. Beyond these limit, the heat transfer rate begins to drop. The enhancement posses by SiO_2 nanofluids at abovementioned

limit is 0.59%, 0.39%, and 0.26% respectively. The reason for this situation is the rate of decrease in heat capacity rate for SiO_2 nanofluids overcomes the increase of effectiveness beyond the mentioned particle volume fraction.

Therefore, for heat transfer devices where turbulent flow occur, the enhancement of heat transfer rate due to nanofluids is not solely dependent on the thermal conductivity while other thermophysical properties such as specific heat, viscosity and density also shows their contributions and this was also concluded by Lee and Mudawar (2007).

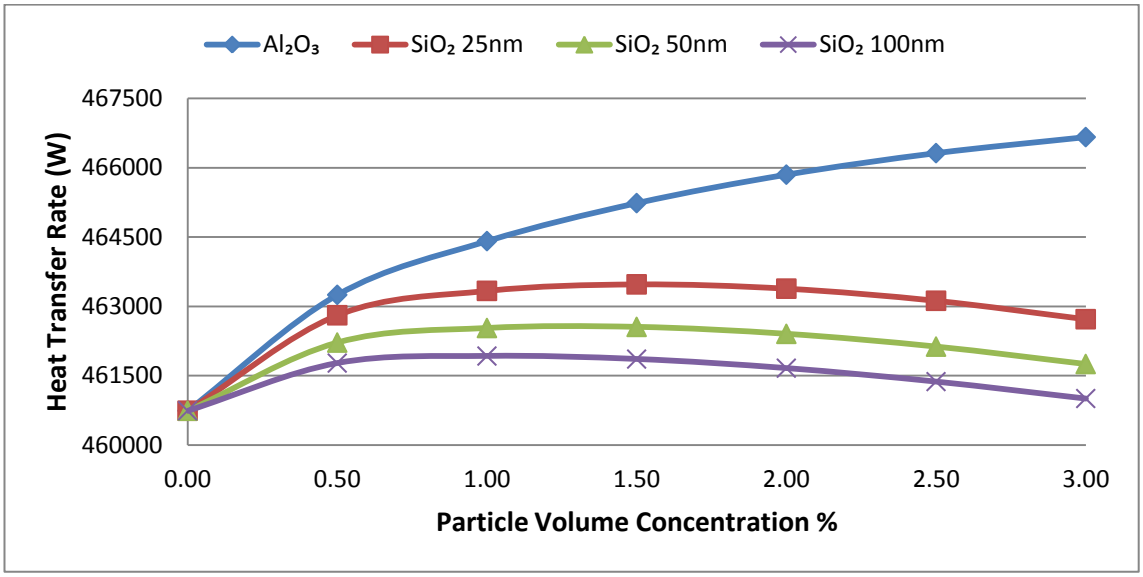

Figure 4.15 Actual Heat Transfer Rate of PHE at Various Particle Volume Concentration.

4.3.2 Hydrodynamic Performance (Pressure Drop) Analysis

Total pressure drop of the PHE consist of three elements as mentioned in section 3.6.2. The calculated friction factor and channel/core pressure drop is plotted in graph as shown in Figure 4.16 and 4.17 respectively. It is found that the friction factor increased with particle volume concentration increase.

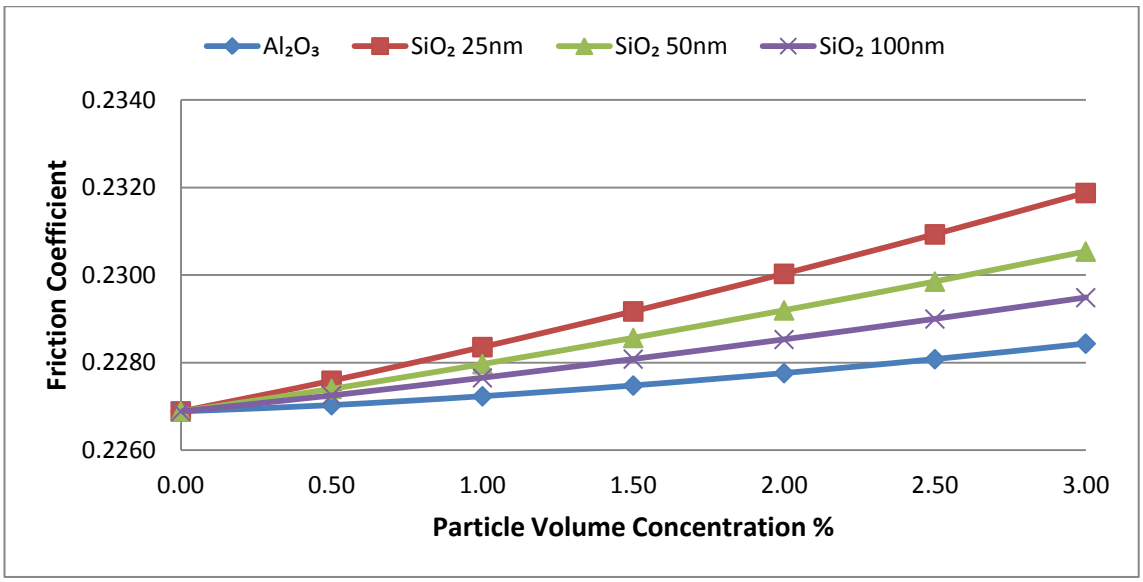

Figure 4.16: Friction Coefficient of Nanofluids at Different Particle Volume Concentration.

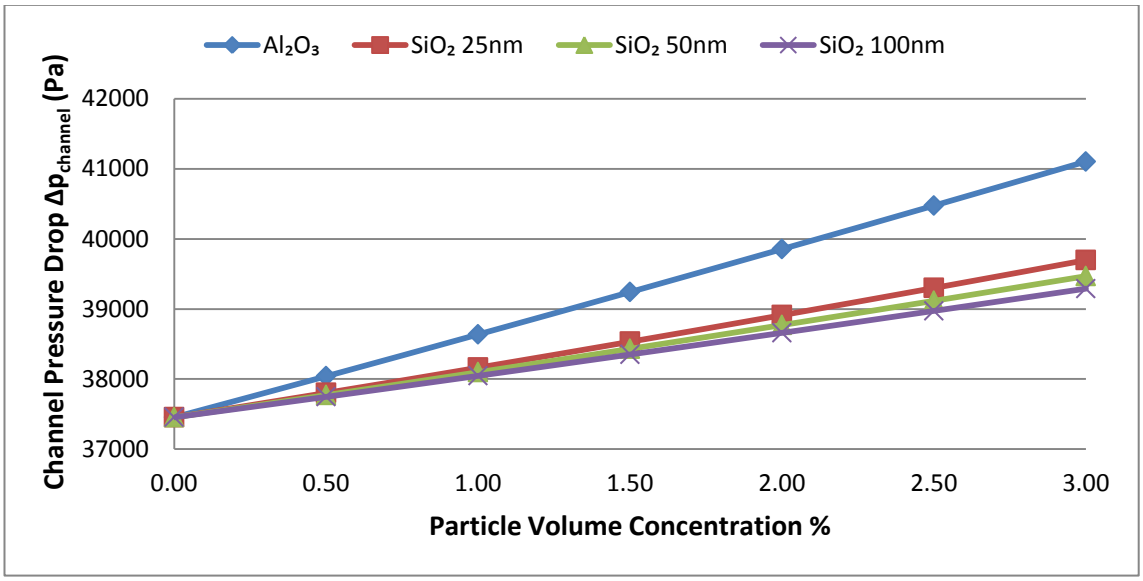

Figure 4.17: Channel Pressure Drop at Various Particle Volume Concentration

Unlike the Nusselt number correlations, the friction factor correlation is only dependent on the Reynolds number in the flow channel. At the given thermal plate geometry, the drop of Reynolds number as in Figure 4.7 resulted the increase of friction factor, because the exponent value of Reynolds number in the correlation has the value of -0.20028. At 3% particle volume

concentration, the rise of friction factor for Al_2O_3 nanofluids is the lowest (0.68%), while the SiO_2-25 nm nanofluids has the highest increased (2.20%).

Figure 4.17 shows Al_2O_3 nanofluids has the highest channel pressure drop at every particle volume concentration, while for SiO_2 nanofluids the value decreased as the particle size increase. Examination on the Equation 3.29 revealed that, the main contributor to the channel pressure drop is the mass flow rate of nanoparticles which is a function of density and volumetric flow rate, while the effect of viscosity only pronounce when the density of nanoparticles is same.

The ports pressure drop and pressure drop due to elevation change is calculated and plotted in Figure 4.18 and 4.19. With the geometry of PHE unchanged, both type of pressure drop is a function of nanoparticles density. Hence, Al_2O_3 nanofluids having higher density shows greater pressure drop than SiO_2.

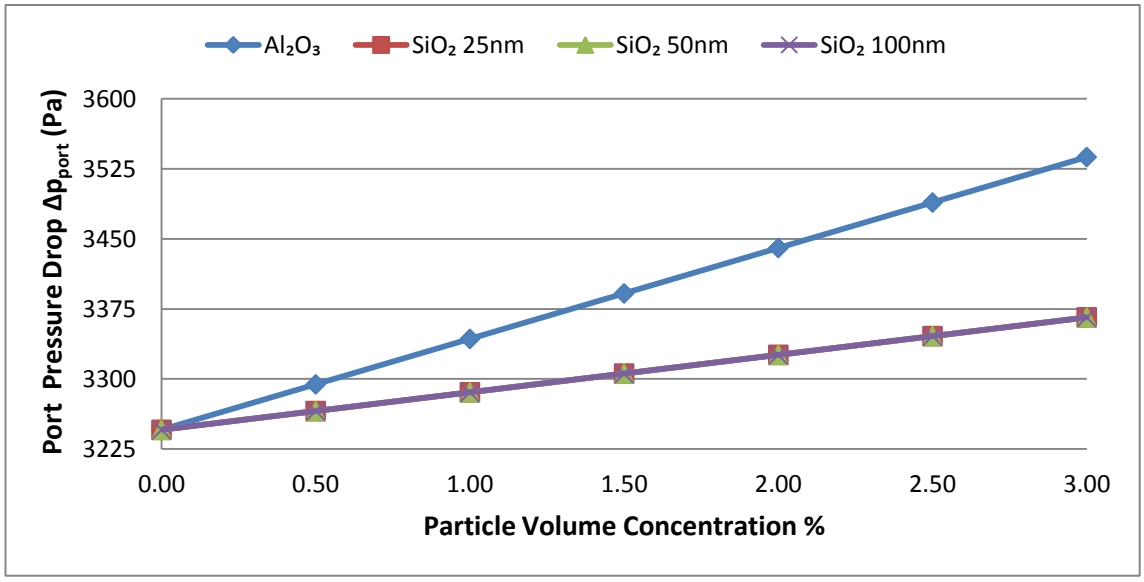

Figure 4.18: Port Pressure Drop at Various Particle Volume Concentration

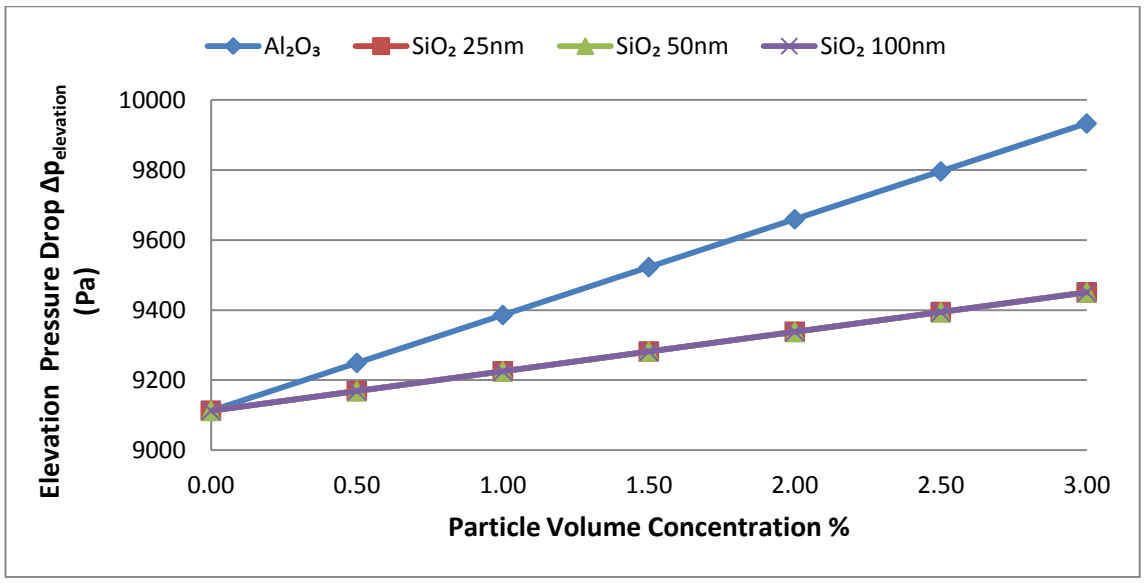

Figure 4.19: Pressure Drop Due to Elevation Change at Various Particle Volume Concentration

The total pressure drop in PHE is plotted in graph as shown in Figure 4.20. Al_2O_3 nanofluids has the highest total pressure drop among others. At 3% particle volume concentration, the total pressure drop increase by 9.88% for Al_2O_3 nanofluids followed by SiO_2-25 nm 6.42%, SiO_2-50 nm 5.69% and lastly SiO_2- 100 nm 5.12%.

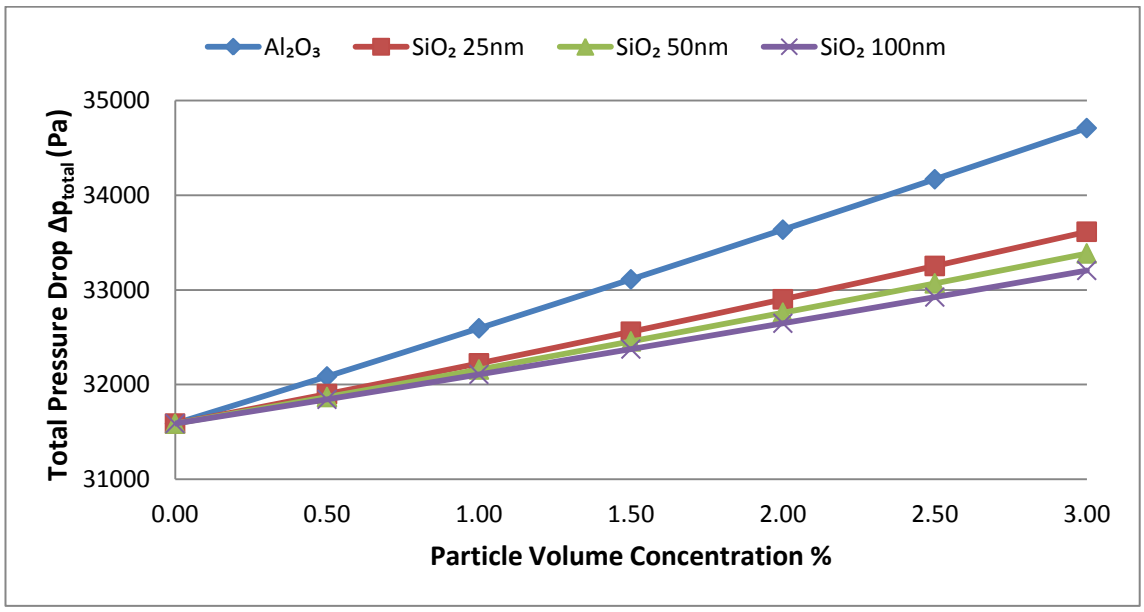

Figure 4.20: Total Pressure Drop of PHE at Various Particle Volume Concentration

To monitor the contribution from types of pressure drop, the amount and types of pressure drop from Al_2O_3 nanofluids is plotted in Figure 4.21. It is found that, with relatively large value compare to the others, channel pressure drop is the main contributor.

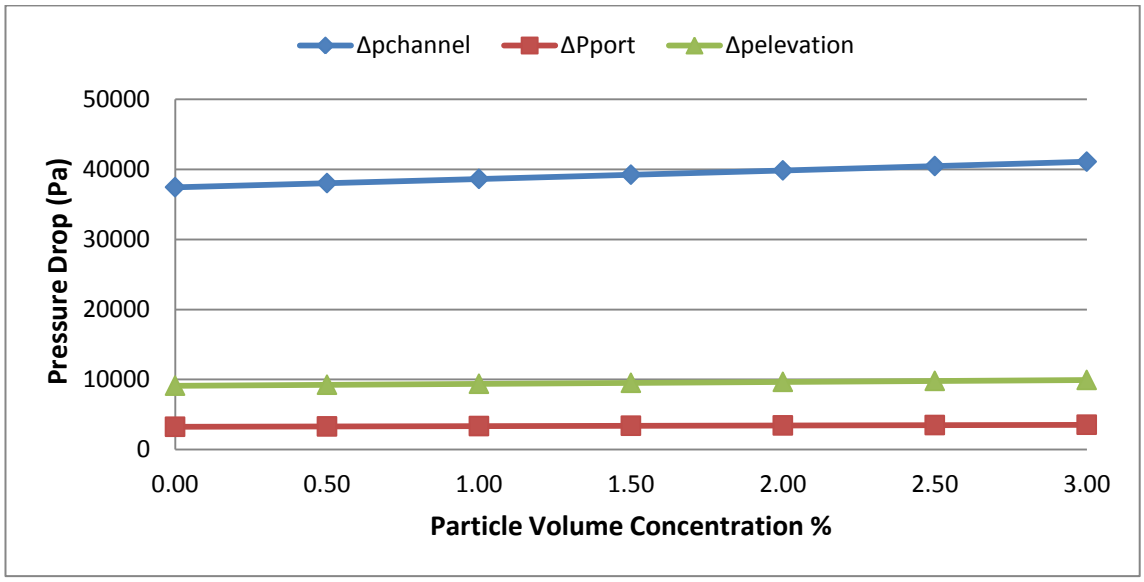

Figure 4.21: Pressure Drop of PHE for Al_2O_3 Nanofluids

In force convection heat transfer system, pumping power is an important parameter that system designers need to pay attention on, because pumping power directly reflect the operating cost of the system. To obtain pumping power, the value of total pressure drop is multiply with the volumetric flow rate of nanofluids. The calculated pumping power is shown in Figure 4.22. The trend of pumping power is similar to the total pressure drop due to the fix volumetric flow rate value. Therefore, it is found that for Al_2O_3 and SiO_2 nanofluids, the increment of pumping power has the same magnitude to the rise of total pressure drop. A reverse calculation is done on the Al_2O_3 nanofluids, it is found that application of Al_2O_3 nanofluids in the existing PHE system does not help in decreasing the energy consumption in sense of pumping power. The pumping

power required for Al_2O_3 nanofluids to handle the same heat duty has rise by 3.13% compare to the original pumping power required. However, the reduction of pump size is possible when the required volumetric flow rate drop. Hence the load on the drive may be reduce and consequently make the system more energy efficient.

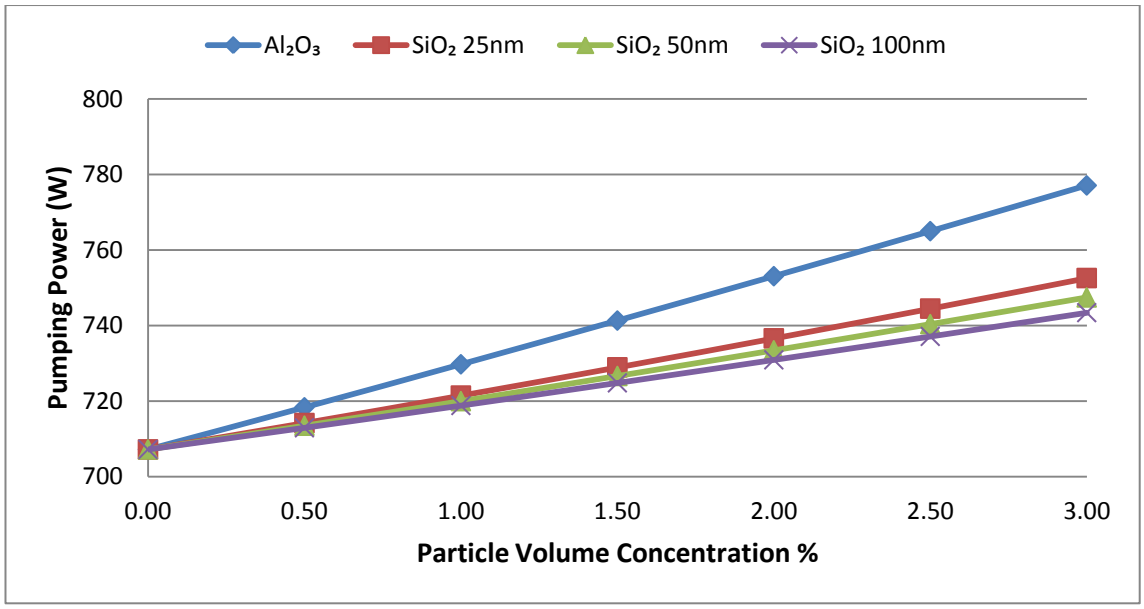

Figure 4.22: Pumping Power Required at Different Particles Volume Concentration

4.4 Application of Nanofluids at PHE Design Stage

4.4.1 Heat Transfer Area Reduction Analysis

The calculated heat transfer area required base on desire NTU are plotted in graphs as in Figure 4.23 to Figure 4.27. It is found that require heat transfer area reduce as the particle volume concentration increase. For every NTU, the Al_2O_3 nanofluids shows greater area reduction compare to SiO_2 nanofluids. Take into account that the calculation is based on equal heat capacity rate of hot and cold working fluid and the heat capacity rate is a fixed value. The mass flow rate supply to PHE is directly dependent on the specific heat of nanofluids. Therefore,

lower specific heat value of Al_2O_3 particles results the increased of mass flow rate supply to the PHE. The combination of higher Reynolds number and thermal conductivity make Al_2O_3 has higher overall heat transfer coefficient and consequently lower heat transfer area required.

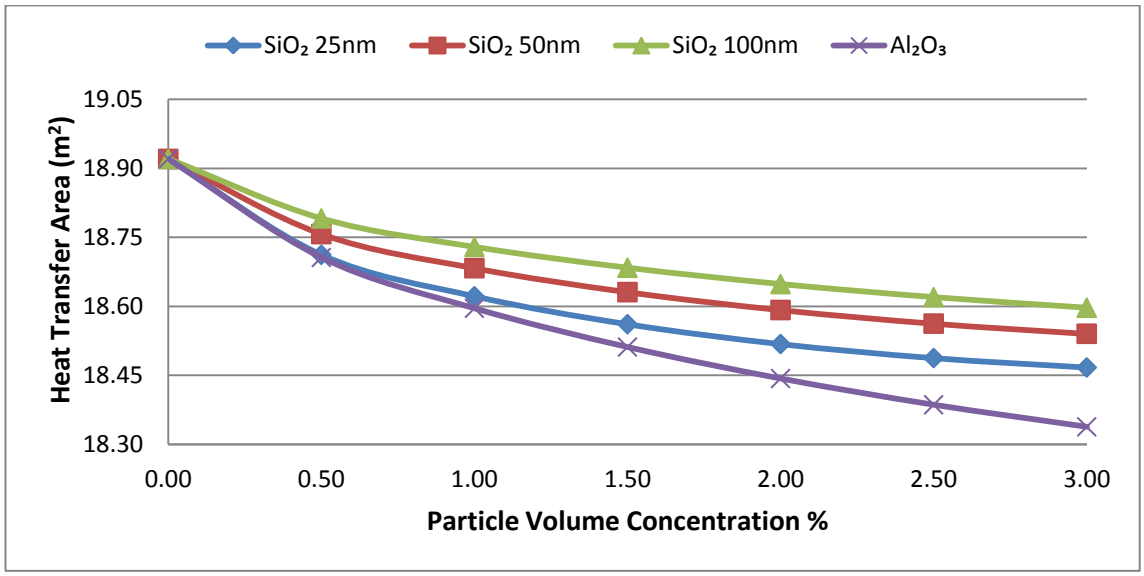

Figure 4.23: Required Heat Transfer Area at NTU = 1

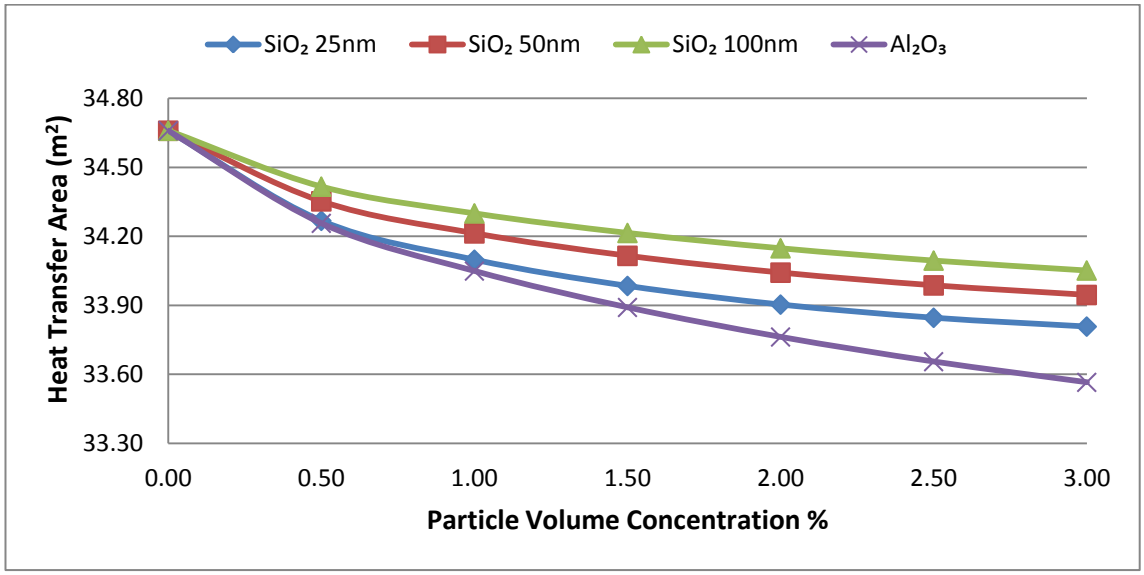

Figure 4.24: Required Heat Transfer Area at NTU = 2

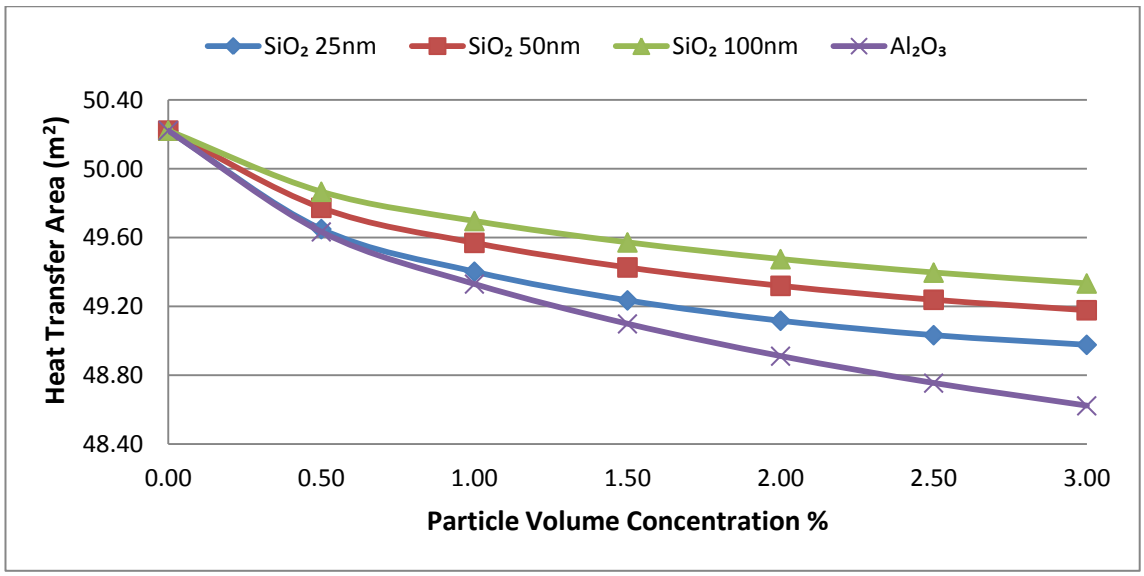

Figure 4.25: Required Heat Transfer Area at NTU = 3

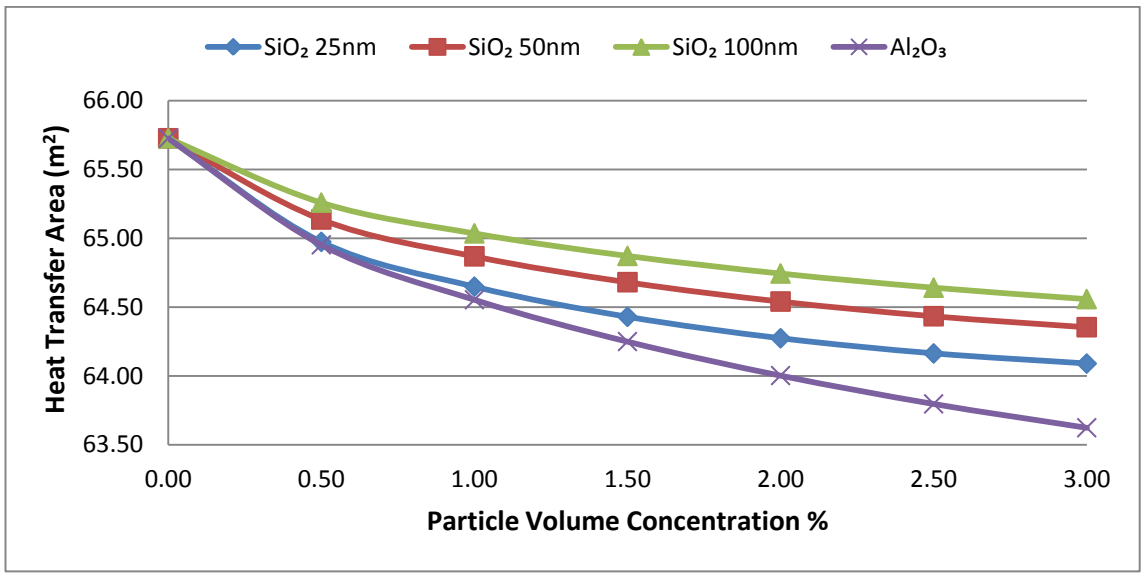

Figure 4.26: Required Heat Transfer Area at NTU = 4

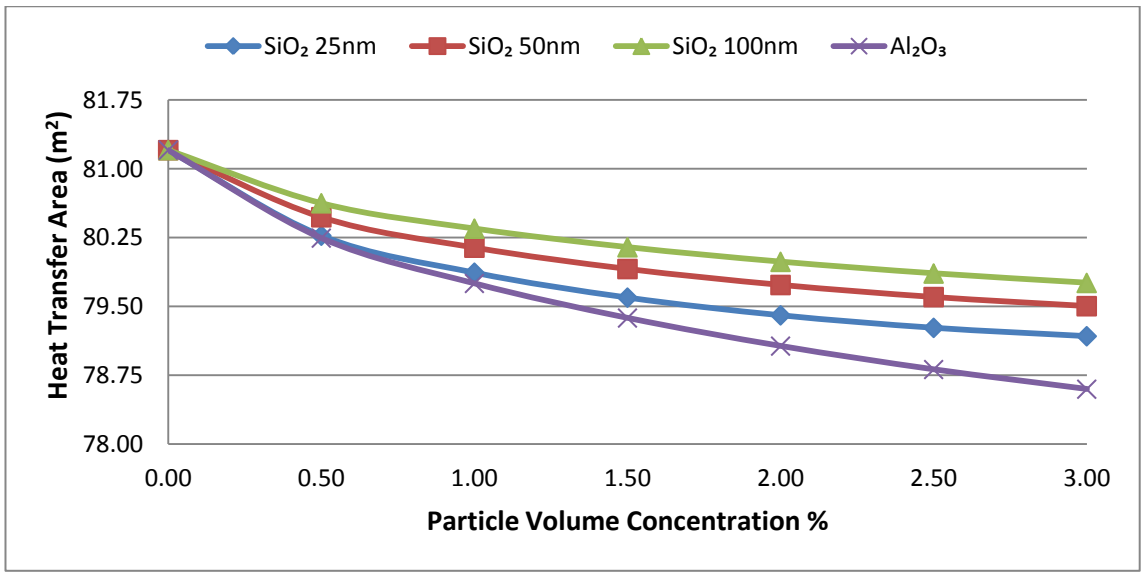

Figure 4.27: Required Heat Transfer Area at NTU = 5

Meanwhile, for SiO_2 nanofluids, the specific heat is independent of particle size, thus the mass flow rate require is same for all types of SiO_2 nanofluids. The dynamic viscosity hence shows its importance in Reynolds number estimation, SiO_2-25 nm with highest dynamic viscosity has lowest Reynolds number and consequently lowest in Nusselt number. However, the high thermal conductivity of SiO_2-25 nm resulted it to have higher overall heat transfer coefficient than both SiO_2-50 nm and SiO_2-100 nm nanofluids. As a result, heat transfer area required at a given NTU for SiO_2-25 nm is lower than SiO_2-50 nm and SiO_2-100 nm nanofluids. Therefore, it can be concluded that when the specific heat is equal and particle volume concentration is fixed, require heat transfer area at a given NTU can be reduce by using smaller nanoparticles size.

The highest percentage of heat transfer area reduction for Al_2O_3 is 3.21%, while for SiO_2, the percent area reduction decreased as nanoparticles size increases i.e. 2.50% for 25 nm, 2.10% for 50 nm and 1.78% for 100 nm nanofluids. Figure 4.28 shows the heat transfer area reduction in percentage for nanofluids at 3% particle volume concentration. In addition, this figure shows

that area reduction cause by nanofluids become greater at higher NTU as clearly shown by Al_2O_3 nanofluids.

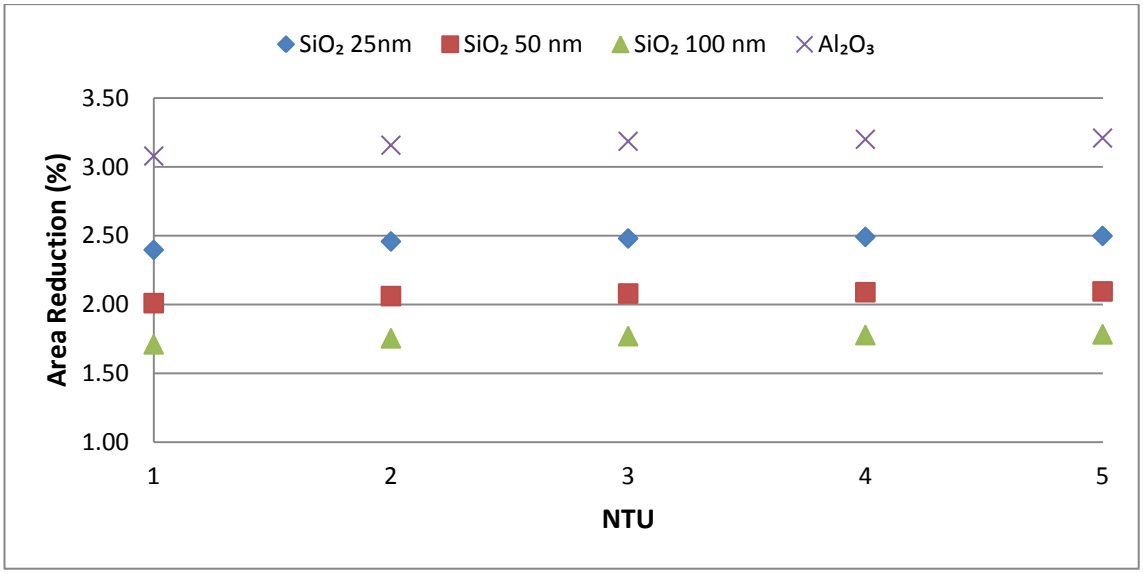

Figure 4.28: Heat Transfer Area Reduction Due to 3% Particle Volume Concentration of Nanofluids

4.4.2 Pressure Drop Analysis

The total pressure drop with respect to NTU is plotted in graphs as shown in Figure 4.29 to Figure 4.33. It is found that, total pressure drop increased as particle volume concentration increase and the difference of pressure drop between types of nanoparticles become significant at high NTU. This is mainly due to the increase of required heat transfer surface area that makes the influences of dynamic viscosity significant. The highest increase of pressure drop occurs at NTU = 5 where 3% particle volume concentration nanofluids is used.

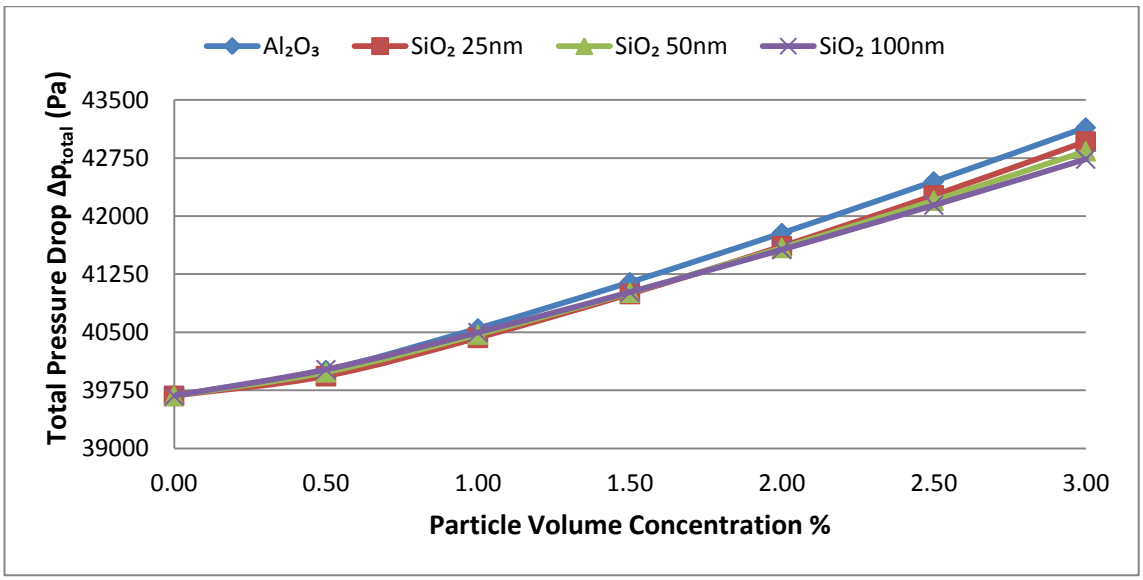

Figure 4.29: Total Pressure Drop of PHE at NTU = 1

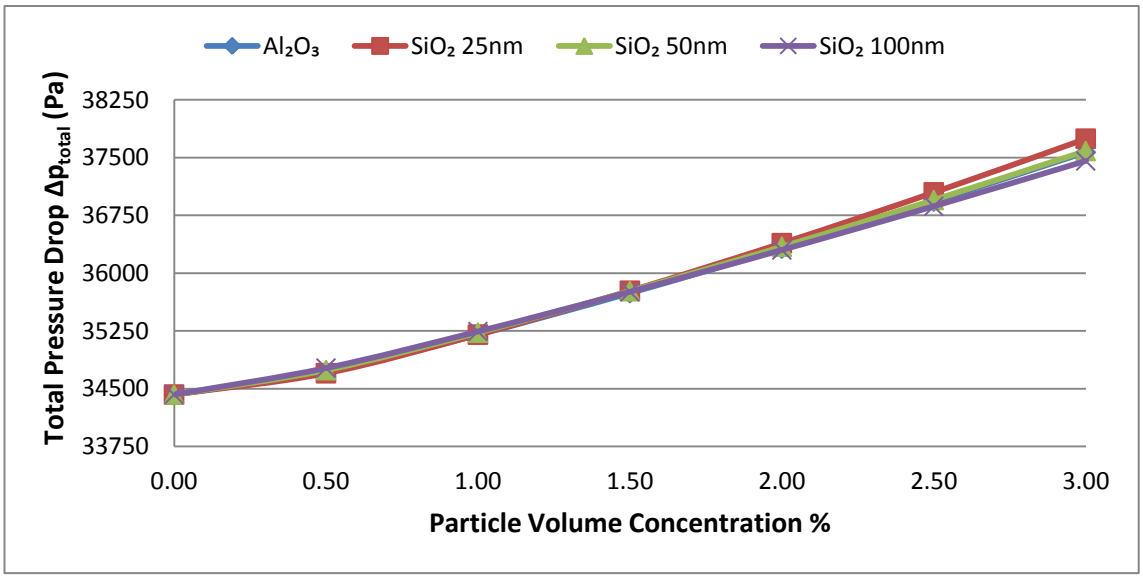

Figure 4.30: Total Pressure Drop of PHE at NTU = 2

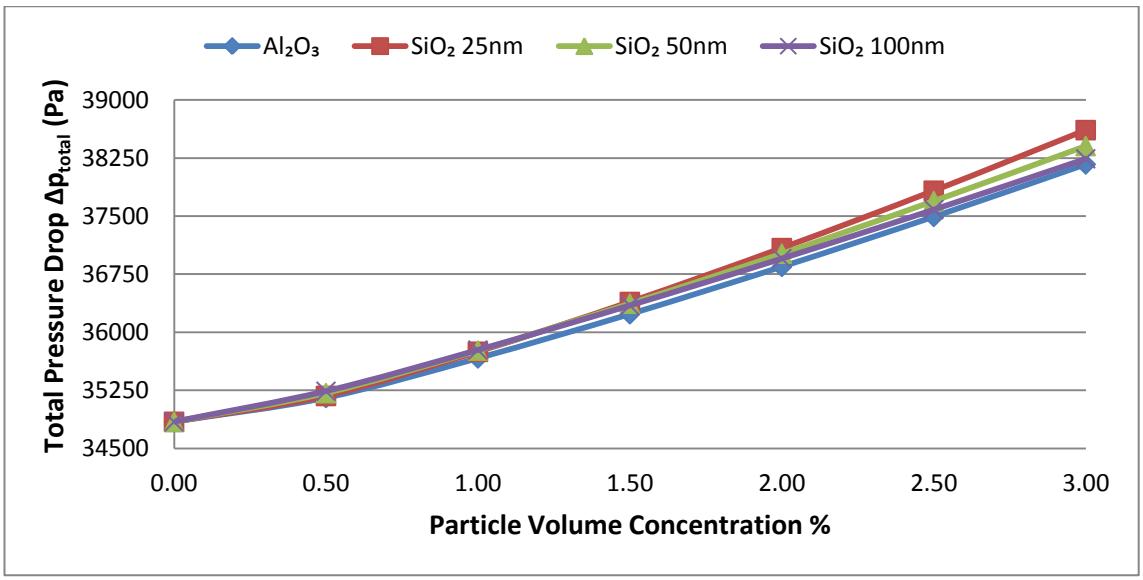

Figure 4.31: Total Pressure Drop of PHE at NTU = 3

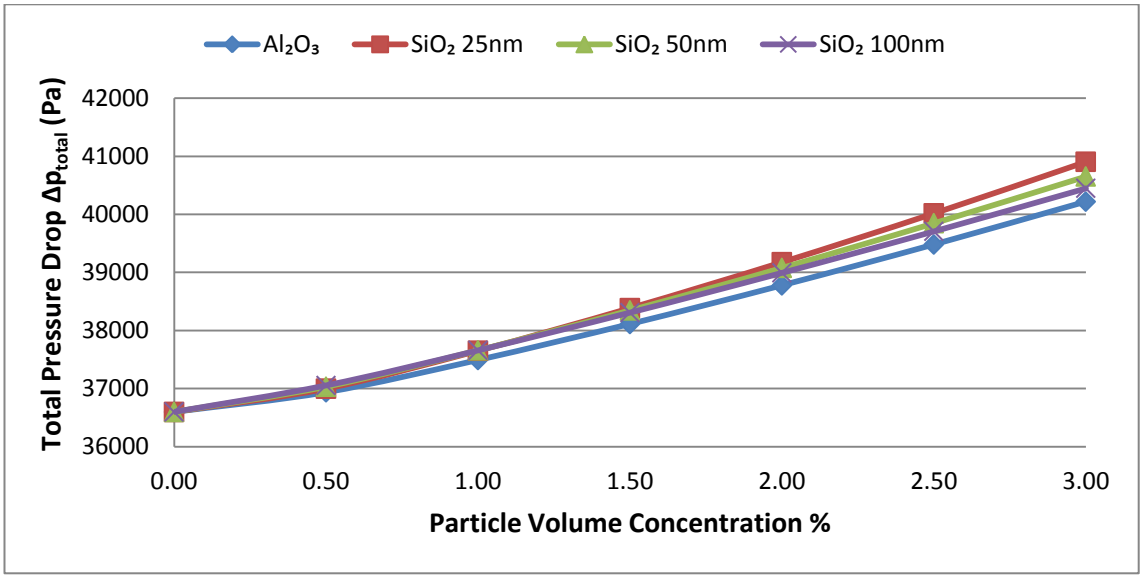

Figure 4.32: Total Pressure Drop of PHE at NTU = 4

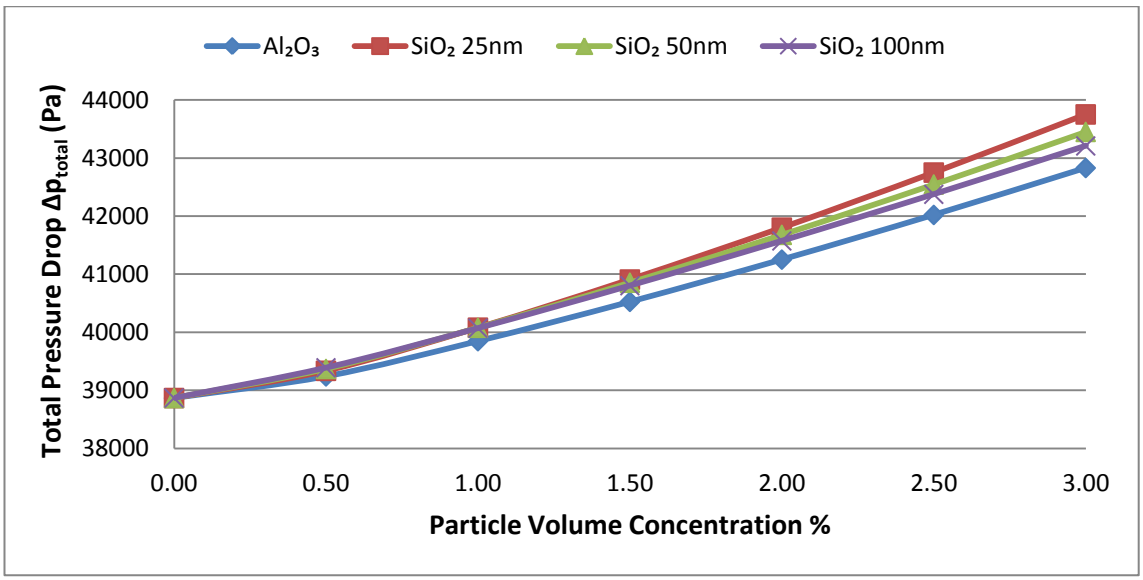

Figure 4.33: Total Pressure Drop of PHE at NTU = 5

Figure 4.34 shows the percent increase of total pressure drop at NTU = 5, the SiO_2-25 nm has raised the total pressure drop by 12.57% followed by SiO_2-50 nm 11.79%, SiO_2-100 nm 11.17% and finally Al_2O_3 10.19%.

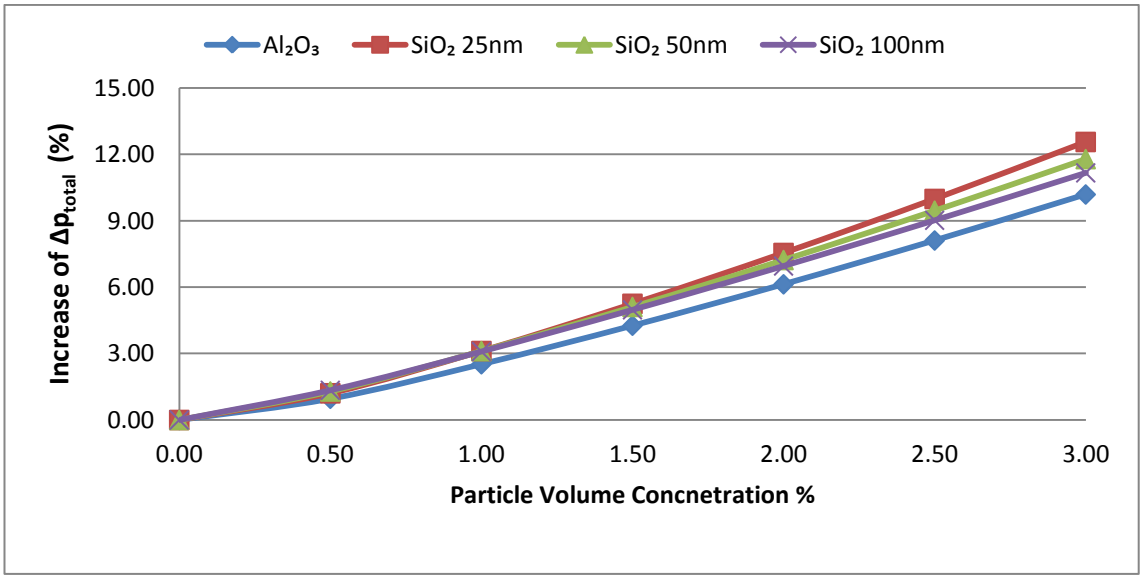

Figure 4.34: Percentage of Pressure Drop Increase at NTU = 5

The total pressure drop as a function of NTU is shown in Figure 4.35. It is observed that the total pressure drop amount for NTU = 1 is similar to NTU = 5, while total pressure drop of PHE is lowest at NTU = 2. Analysis shows that at

NTU = 1, the effectiveness of PHE is lowest and higher minimum heat capacity rate is needed, hence the mass flow rate supply to PHE must be increased. Although the increase of mass flow rate increases the Reynolds number and lowering the friction factor, that lead to lower channel pressure drop. The increased of mass flow rate causes the rise of port pressure drop.

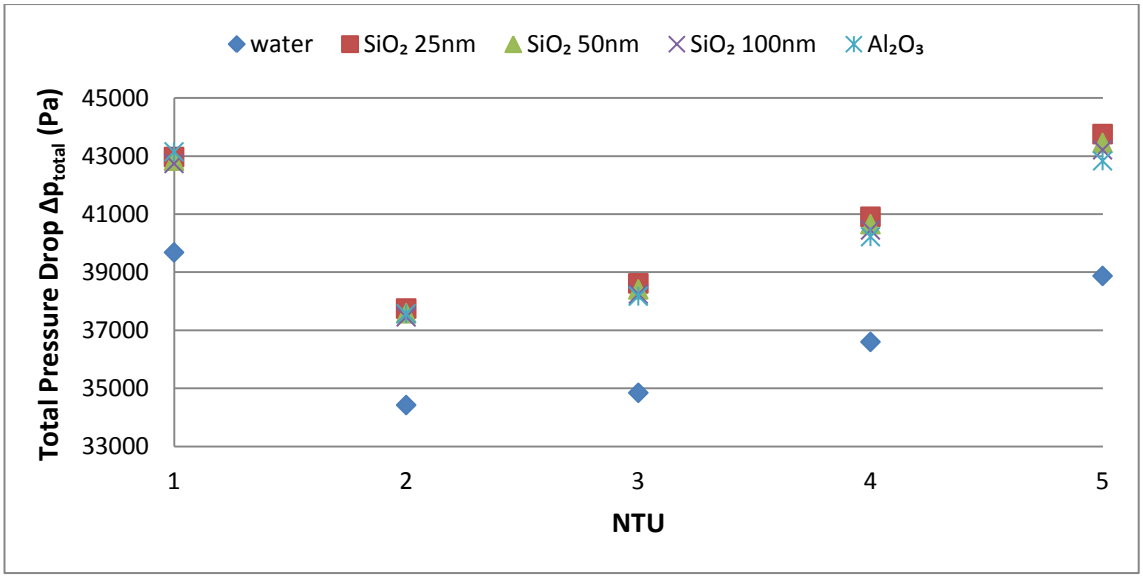

Figure 4.35: Total Pressure Drop for 3% Particle Volume Concentration Nanofluids

Meanwhile, converting the require heat transfer area to the length/height of the plate by assuming the width of plate remain constant shows that the height of plates for NTU = 1 is shortest; as a result smaller elevation pressure drop is obtained. However, due to the flow configuration of PHE as shown in Figure 3.3, the pressure drop by elevation need to be subtracted from the total pressure drop. Thus, less elevation pressure drop means lesser pressure drop deducted from total pressure drop and consequently the total pressure drop is higher than that of NTU = 2 to 4. The influence from type of pressure drop on the amount of total pressure drop is shown in Figure 4.36.

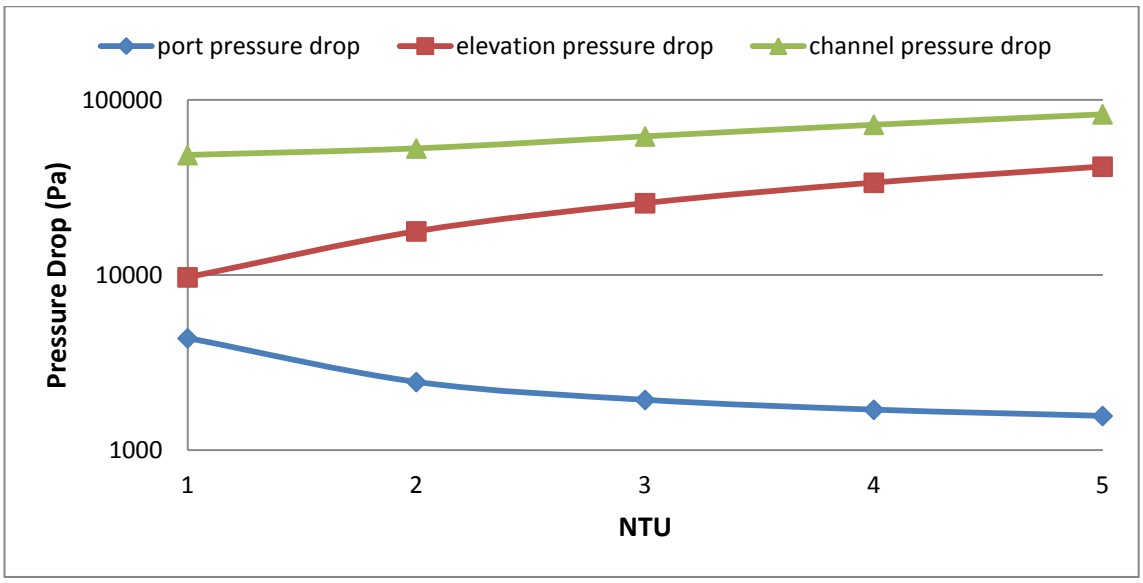

Figure 4.36: Pressure Drop for Al_2O_3 Nanofluids at 3% Particle Volume Concentration

As summary, the investigation on application of nanofluids at PHE designing stage revealed that nanofluids helps in reduction of require heat transfer area at a desire NTU value. Reduction in heat transfer area means PHE now can be more compact and have lighter weight. In term of economy, the reduction on raw material and logistic cost can be expected. It should be noted that, the calculation is based on heat capacity rate ratio value of 1, the effectiveness calculated from NTU-effectiveness relation is the lowest as shown in Figure 2.3. Therefore, more heat transfer area reduction can be expected for actual PHE system where heat capacity rate ratio less than 1 is commonly used. Meanwhile, it is also found that, Al_2O_3 nanofluids shows better result in area reduction and total pressure drop consideration compare to SiO_2 nanofluids. Specific heat and thermal conductivity of nanofluids are essential parameters in heat transfer area reduction estimation, while density is an important factor in pressure drop estimation in addition of two aforementioned parameters.

5.0 CONCLUSION

In this study, the application of nanofluids as hot side working fluids in existing PHE system has been investigated. The thermal performance analysis on PHE running with nanofluids shows positive results and conclusions drawn from the thermal analysis are:

a) The enhancement of heat transfer performance increase as particle volume concentration increase and particle size decrease. Al_2O_3 nanofluids showed better thermal performance compare to SiO_2 nanofluids.
b) Al_2O_3 nanofluids with 3% particle volume concentration enhance the heat transfer rate by 1.29%. For SiO_2 nanofluids, the maximum enhancement occurred at 1.5% for SiO_2-25nm and SiO_2-50nm while SiO_2-100nm nanofluids the enhancement stops at 1% particle volume concentration. Their percent of enhancement is 0.59%, 0.39%, and 0.26% respectively.
c) The amount of heat transfer rate enhancement provided by Al_2O_3 nanofluids may help to decrease the volumetric flow rate of hot side working fluid by 2.66%.

Meanwhile, investigation on pressure drop of existing PHE system that runs with nanofluids showed that:

a) The friction factor and pressure drop increased as nanofluids particle volume concentration increase. At equal density, the nanofluids with smaller particle size that has higher dynamic viscosity result in higher increase in pressure drop.
b) The total pressure drop increase by 9.88% for Al_2O_3 nanofluids followed by SiO_2-25 nm 6.42%, SiO_2-50 nm 5.69% and lastly SiO_2- 100 nm 5.12%.

c) The pumping power required for Al_2O_3 nanofluids to handle the same heat duty has risen by 3.13% compare to the original pumping power. However, the reduction of pump size is possible when the required volumetric flow rate drop.

The application of nanofluids in PHE design stage shows encouraging results in heat transfer area reduction. It can be concluded that:

a) Increase of particle volume concentration reduce the require heat transfer area to achieve a desire NTU.
b) In the situation where specific heat is equal and particle volume concentration is fixed, higher reduction of require heat transfer area at a given NTU can be achieve by using smaller nanoparticles size.
c) Al_2O_3 nanofluids reduce the heat transfer area by approximately 3% for every NTU value in the investigation. Highest percentage of heat transfer area reduction for Al_2O_3 is 3.21%. For SiO_2 nanofluids, 2.50%, 2.10% and 1.78% of area reduction was obtained with 25 nm, 50 nm and 100 nm particle size respectively.
d) The pressure drop increase as particles volume concentration increase.
e) Al_2O_3 nanofluids show better performance in heat transfer area reduction and its corresponding pressure drop compare to SiO_2 nanofluids.

BIBLIOGRAPHY

Brinkman, H. C. (1952). The viscosity of concentrated suspensions and solutions. *Journal Chemistry Physics, 20*, 571-581.

Choi, S. U. S., & Eastman, J. A. (1995). *Enhancing thermal conductivity of fluids with nanoparticles*. Paper presented at the ASME International Mechanical Engineering Congress & Exposition, San Francisco, CA.

Chrisholm, D., & Wanniarachchi, A. S. (1992). Maldistribution in single-pass mixed channel plate heat exchanger. *Compact Heat Exchangers for Power and Process Industries, HTD, 201*, 95-99.

Corcione, M. (2011). Empirical correlating equations for predicting the effective thermal conductivity and dynamic viscosity of nanofluids. *Energy Conversion and Management, 52*, 789-793.

Das, S. K., Putra, N., Thiesen, P., & Roetzel, W. (2003). Temperature dependence of thermal conductivity enhancement for nanofluids. *Journal of Heat Transfer, 125*, 567-574.

DHP Engineering. *Manual: Plate Type Heat Exchangers*.

Duangthongsuk, W., & Wongwises, S. (2008). Effect of thermophysical properties models on the predicting of the convective heat transfer coefficient for low concentration nanofluid. *International Communications in Heat and Mass Transfer, 35*, 1320-1326.

Eastman, J. A., Choi, S. U. S., Li, S., Yu, W., & Thompson, L. J. (2001). Anomalously increased effective thermal conductivities of ethylene glycol-based nanofluids containing copper nanoparticles. *Applied Physics Letters, 78*(6), 718-720.

Focke, W. W., Zachariades, J., & Olivier, I. (1985). The effect of the corrugation inclination angle on the thermohydraulic performance of plate heat exchangers. *International Journal of Heat and Mass Transfer, 28*(8), 1469-1479.

Godson, L., Raja, B., Lal, D. M., & Wongwises, S. (2010). Enhancement of heat transfer using nanofluids—An overview. *Renewable and Sustainable Energy Reviews, 14*, 629-641.

Gut, J. A. W., & Pinto, J. M. (2004). Optimal configuration design for plate heat exchangers. *International Journal of Heat and Mass Transfer, 47*, 4833–4848.

Hamilton, R. L., & Crosser, O. K. (1962). Thermal conductivity of heterogeneous two component system. *I & E C Fundamentals, 1*(3), 187-191.

Heavner, R. L., Kumar, H., & Wanniarachchi, A. S. (1993). Performance of an industrial plate heat exchanger: effect of chevron angle. *AIChE Symposium Series, 89*(295), 262-267.

Hosseini, M. S., Mohebbi, A., & Ghader, S. (2011). Prediction of thermal conductivity and convective heat transfer coefficient of nanofluid by local composition theory. *Journal of Heat Transfer, 133*, 0524011-0524019.

Hwang, Y. J., Ahn, Y. C., Shin, H. S., Lee, C. G., Kim, G. T., Park, H. S., & Lee, J. K. (2006). Investigation on characteristic of thermal conductivity enhancement of nanofluids. *Current Applied Physics, 6*, 1068-1071.

Incropera, F. P., & DeWitt, D. P. (2002). *Fundamentals of Heat and Mass Transfer* (5 ed.): John Wiley & Sons, Inc.

Jang, S. P., & Choi, S. U. S. (2007). Effect of various parameters on nanofluid thermal conductivity. *Journal of Heat Transfer, 129*, 617-623.

Kandlikar, S. G., & Shah, R. K. (1989). Multipass plate heat exchangers—effectiveness-NTU results and guidelines for selecting pass arrangements. *Journal of Heat Transfer, 111*, 300-313.

Kays, W. M. (1950). Loss coefficients for abrupt changes in flow cross section with low Reynolds number flow in single and multiple tube system. *Transactions of ASME, 72*, 1067-1074.

Kays, W. M., & London, A. L. (1984). *Compact Heat Exchangers* (3 ed.): McGraw-Hill.

Keblinski, P., Phillpot, S. R., Choi, S. U. S., & Eastman, J. A. (2002). Mechanisms of heat flow in suspensions of nano-sized particles (nanofluids). *International Journal of Heat and Mass Transfer, 45*, 855-863.

Khan, T. S., Khan, M. S., Chyu, M.-C., & Ayub, Z. H. (2010). Experimental investigation of single phase convective heat transfer coefficient in a corrugated plate heat exchanger for multiple plate configurations. *Applied Thermal Engineering, 30*, 1058-1065.

Koo, J., & Kleinstreuer, C. (2004). A new thermal conductivity model for nanofluids. *Journal of Nanoparticle Research, 6*, 577-588.

Lee, J., & Mudawar, I. (2007). Assessment of the effectiveness of nanofluids for singler-phase and two-phase heat transfer in micro-channel. *International Journal of Heat and Mass Transfer, 50*, 452-463.

Lee, S., Choi, S. U. S., Li, S., & Eastman, J. A. (1999). Measuring thermal conductivity of fluids containing oxide nanoparticles. *Journal of Heat Transfer, 121*, 280-289.

Leong, K. Y., Saidur, R., Kazi, S. N., & Mamun, A. H. (2010). Performance investigation of an automotive car radiator operated with nanofluid-based coolants (Nanofluid as a coolant in a radiator). *Applied Thermal Engineering, 30*, 2685-2692.

Li, C. H., & Peterson, G. P. (2007). The effect of particle size on the effective thermal conductivity of Al_2O_3-water nanofluids. *Journal of Applied Physics, 101*, 0443121-0443125.

Liu, H., Wang, X., Zhang, M., Zhang, W., & Liu, J. (2008). *Heat transfer simulation of nanofluids in micro channel cooler*. Paper presented at the International Conference on Electronic Packaging Technology & High Density Packaging (ICEPT-HDP 2008).

Lotfi, R., Saboohi, Y., & Rashidi, A. M. (2010). Numerical study of forced convective heat transfer of Nanofluids: Comparison of different approaches. *International Communications in Heat and Mass Transfer, 37*, 74-78.

Maxwell, J. C. (1904). A treatis on electricity and magnetism. *Oxford University Press*.

Muley, A., & Manglik, R. M. (1999). Experimental study of turbulent flow heat transfer and pressure drop in a plate heat exchanger with chevron plates. *Journal of Heat Transfer, 121*, 110-117.

Muley, A., Manglik, R. M., & Metwally, H. M. (1999). Enhanced heat transfer characteristic of viscous liquid flows in a chevron plate heat exchanger. *Journal of Heat Transfer, 121*, 1011-1017.

Namburu, P. K., Kulkarni, D. P., Misra, D., & Das, D. K. (2007). Viscosity of copper oxide nanoparticles dispersed in ethylene glycol and water mixture. *Experimental Thermal and Fluid Science, 32*, 397-402.

Nguyen, C. T., Desgranges, F., Galanis, N., Roy, G., Mare, T., Boucher, S., & Mintsa, H. A. (2008). Viscosity data for Al_2O_3 water nanofluid hysteresis: is heat transfer enhancement using nanofluid reliable? *International Journal of Thermal Sciences, 47*, 103-111.

Nguyen, C. T., Roy, G., Gauthier, C., & Galanis, N. (2007). Heat transfer enhancement using Al_2O_3–water nanofluid for an electronic liquid cooling system. *Applied Thermal Engineering, 27*, 1501-1506.

Okada, K., Ono, M., Tominura, T., Okuma, T., Konno, H., & Ohtani, S. (1972). Design and heat transfer characteristics of new plate heat exchanger. *Heat Transfer-Japanese Research, 1*(1), 90-95.

Pak, B. C., & Cho, Y. I. (1998). Hydrodynamic and heat transfer study of dispersed fluids with submicron metallic oxide particles. *Experimental Heat Transfer, 11*(2), 151-170.

Pantzali, M. N., Mouza, A. A., & Paras, S. V. (2009). Investigating the efficacy of nanofluids as coolants in plate heat exchanger (PHE). *Chemical Engineering Science 64*, 3290-3300.

Saidur, R., Leong, K. Y., & Mohammad, H. A. (2011). A review on applications and challenges of nanofluids. *Renewable and Sustainable Energy Reviews, 15*, 1646-1668.

Schlunder, E. U. (1983). *Heat Exchanger Design Handbook*: Hemisphere Publishing Corporation.

Shah, R. K., & Focke, W. W. (1988). *Heat Transfer Equipment Design*: Hemisphere Publishing Corporation

Shah, R. K., & Kandlikar, S. G. (1988). The influence of the number of thermal plates on plate heat exchanger performance.

Shah, R. K., & Sekulic, D. P. (2003). *Fundamentals of Heat Exchanger Design*: John Wiley & Sons, Inc.

Sharqawy, M. H., Lienhard, J. H., & Zubair, S. M. (2010). Thermophysical properties of seawater: A review of existing correlations and data. *Desalination and Water Treatment, 16*, 354-380.

Teng, T. P., Hung, Y. H., Teng, T. C., Mo, H. E., & Hsu, H. G. (2010). The effect of alumina/water nanofluid particle size on thermal conductivity. *Applied Thermal Engineering, 30*, 2213-2218.

Tsai, T. H., & Chein, R. (2007). Performance analysis of nanofluid-cooled microchannel heat sinks. *International Journal of Heat and Fluid Flow, 28*, 1013-1026.

Vajjha, R. S., & Das, D. K. (2009a). Experimental determination of thermal conductivity of three nanofluids and development of new correlations. *International Journal of Heat and Mass Transfer, 52*, 4675-4682.

Vajjha, R. S., & Das, D. K. (2009b). Specific heat measurement of three nanofluids and development of new correlations. *Journal of Heat Transfer, 131*, 0716011-0716017.

Vajjha, R. S., Das, D. K., & Kulkarni, D. P. (2010). Development of new correlations for convective heat transfer and friction factor in turbulent regime for nanofluids. *International Journal of Heat and Mass Transfer, 53*, 4607-4618.

Vajjha, R. S., Das, D. K., & Mahagaonkar, B. M. (2009). Density measurement of different nanofluids and their comparison with theory. *Petroleum Science and Technology, 27*(6), 612-624.

Wang, L., Sunden, B., & Manglik, R. M. (2007). *Plate Heat Exchanger: Design, Applications and Performance*: WIT Press.

Wang, X. Q., & Mujumdar, A. S. (2007). Heat transfer characteristics of nanofluids: a review. *International Journal of Thermal Sciences, 46*, 1-19.

White, F. M. (1999). *Fluid Mechanics* (4 ed.): McGraw-Hill.

Xuan, Y., & Roetzel, W. (2000). Conceptions for heat transfer correlation of nanofluids. *International Journal of Heat and Mass Transfer, 43*, 3701-3707.

Yu, W., Xie, H., Chen, L., & Li, Y. (2010). Investigation on the thermal transport properties of ethylene glycol-based nanofluids containing copper nanoparticles. *Powder Technology, 197*, 218-221.

Zaleski, T., & Klepacka, K. (1992). Plate Heat Exchangers—method of calculation, charts and guidelines for selecting plate heat exchanger configurations. *Chemical Engineering and Processing, 31*, 49-56.

Zamzamian, A., Oskouie, S. N., Doosthoseini, A., Joneidi, A., & Pazouki, M. (2011). Experimental investigation of forced convective heat transfer coefficient in nanofluids of Al_2O_3/EG and CuO/EG in a double pipe and plate heat exchangers under turbulent flow. *Experimental Thermal and Fluid Science, 35*, 495-502.

APPENDIX A

Sample Calculation for Thermal and Hydrodynamic Analysis on Existing PHE

Volumetric Flow Rate

$$\dot{\forall} = \frac{\dot{m}_{total}}{\rho_{water}} = \frac{22.22}{992.46} = 0.02238881 \ \frac{m^3}{s}$$

Mass Flow Rate for Hot Side (Water)

$$\dot{m}_{water} = \dot{\forall} \times \ \rho_{water} = 22.22 \ \frac{kg}{s}$$

Reynolds number at Hot Side (Water)

$$Re = \frac{\dot{m}_{total} \ \times D_e}{N \times \ A_c \ \times \mu}$$

$$= \frac{22.22 \times 2 \times 0.003}{25 \times (0.003 \times 0.40884) \times 0.0006758}$$

$$= 6433.73$$

Nusselt number at Hot Side (Water)

$$Nu = \ [0.2668 - 0.006967\beta + 7.244 \times 10^{-5}\beta^2]$$
$$\times [20.78 - 50.94\phi + 41.16\phi^2 - 10.51\phi^3]$$
$$\times Re^{\left[0.728+0.0543sin\left[\left(\pi\beta/45\right)+3.7\right]\right]} Pr^{1/3} \left(\frac{\mu}{\mu_{wall}}\right)^{0.14}$$

$$= \ [0.2668 - 0.006967(60) + 7.244 \times 10^{-5}(60)^2]$$

$$\times [20.78 - 50.94(1.153) + 41.16(1.153)^2 - 10.51(1.153)^3]$$

$$\times 6433.73^{\left[0.728+0.0543sin\left[\left(\pi(60)/45\right)+3.7\right]\right]} 4.4835^{1/3} \left(\frac{0.0006758}{0.0007061}\right)^{0.14}$$

$$= 112.09$$

Convection heat transfer coefficient at Hot Side (Water)

$$h = \frac{Nuk}{D_e}$$

$$= \frac{112.09 \times 0.62980}{0.006}$$

$$= 11{,}765.71 \ \frac{W}{m^2K}$$

Re, Nu and h for Cold Side Working Fluid (Sea Water 4% Salinity)

$$Re = \frac{28.34 \times 2 \times 0.003}{25 \times (0.003 \times 0.40884) \times 0.000809}$$

$$= 6854.69$$

$$Nu$$

$$= \ [0.2668 - 0.006967(60) + 7.244 \times 10^{-5}(60)^2]$$

$$\times [20.78 - 50.94(1.153) + 41.16(1.153)^2 - 10.51(1.153)^3]$$

$$\times 6854.69^{\left[0.728+0.0543sin\left[\left(\pi(60)/45\right)+3.7\right]\right]} 5.194^{1/3} \left(\frac{0.000809}{0.000774}\right)^{0.14}$$

$$Nu = 125.24$$

$$h = \frac{125.24 \times 0.6202}{0.006}$$

$$= 12{,}945.64 \ \frac{W}{m^2K}$$

Overall Heat Transfer Coefficient

$$U = \frac{1}{\left(\frac{1}{h_{cold}} + \frac{1}{h_{hot}} + \frac{\delta_{plate}}{k_{plate}}\right)}$$

$$= \frac{1}{\left(\frac{1}{12{,}945.64} + \frac{1}{11765.71} + \frac{0.0005}{21.9}\right)}$$

$$= 5403.41 \ \frac{W}{m^2K}$$

Heat Capacity

$$C_h = \ c_{p,nf} \times \dot{m}_{total,nf}$$

$$= 4178.3 \times 22.22$$

$$= 92{,}841.83 \ W/K$$

$$C_c = \ c_{p,cold} \times \dot{m}_{\ total,cold}$$

$$= 3980.32 \times 28.34$$

$$= 112{,}802.27 \ W/K$$

Heat Capacity Ratio

$$C^* = \frac{C_{min}}{C_{max}}$$

$$= \frac{92{,}841.826}{112{,}802.269}$$

$$= 0.823049$$

Number of Transfer Unit (NTU)

$$NTU = \frac{UA_{total}}{C_{min}}$$

$$= \frac{5403.42 \times 19.11}{92{,}841.826}$$

$$= 1.112207$$

Effectiveness of PHE

$$\varepsilon = \frac{1 - \exp[-NTU(1 - C^*)]}{1 - C^* \exp[-NTU(1 - C^*)]}$$

$$= \frac{1 - \exp[-1.112207(1 - 0.823049)]}{1 - 0.823049 \exp[-1.112207(1 - 0.823049)]}$$

$$= 0.551408$$

Maximum Heat Transfer Rate

$$q_{max} = C_{min}(T_{hot,i} - T_{cold,i})$$

$$= 92{,}841.826 \times (314 - 305)$$

$$= 835{,}576.43\ W$$

Actual Heat Transfer Rate of PHE

$$q = \varepsilon q_{max}$$

$$= 0.551408 \times 835{,}576.434$$

$$= 460{,}743.57\ W$$

Pressure Drop Analysis for Hot Side Working Fluid (Water)

Friction Factor

$$f = [2.917 - 0.1277\beta + 2.016 \times 10^{-3}\beta^2] \times [5.474 - 19.02\phi + 18.93\phi^2 - 5.341\phi^3] \times Re^{-\left[0.2+0.0577sin\left[\left(\pi\beta/45\right)+2.1\right]\right]}$$

$$f = [2.917 - 0.1277(60) + 2.016 \times 10^{-3}(60)^2] \times [5.474 - 19.02(1.153) + 18.93(1.153)^2 - 5.341(1.153)^3] \times 6433.73^{-\left[0.2+0.0577sin\left[\left(\pi(60)/45\right)+2.1\right]\right]}$$

$$f = 0.226887$$

Channels Pressure Drop

$$\Delta p_{channel} = \frac{2fL\left(\frac{\dot{m}_{total}}{NA_c}\right)^2}{D_e\rho}$$

$$= \frac{2 \times 0.226887 \times 0.936\left(\frac{22.22}{25 \times (0.003 \times 0.40884)}\right)^2}{0.006 \times 992.46}$$

$$= 37{,}455.02\ Pa$$

Ports and Manifolds Pressure Drop

$$\Delta p_{port} = \frac{1.5\left(\frac{4\dot{m}_{total}}{\pi D_{port}^2}\right)^2}{2\rho}$$

$$= \frac{1.5\left(\frac{4 \times 22.22}{\pi(0.11684^2)}\right)^2}{2 \times 992.46}$$

$$= 3245.57\ Pa$$

Pressure Drop due to Elevation Change

$$\Delta p_{elevation} = -\rho g L$$

$$= -992.46 \times 9.81 \times 0.936$$

$$= -9112.93\ Pa$$

Negative value is taken since the direction of flow is downward

Total Pressure Drop

$$\Delta p_{total} = \Delta p_{channel} + \Delta p_{port} + \Delta p_{elevation}$$

$$= 37{,}455.022 + 3245.566 - 9112.926$$

$$= 31{,}587.65\ Pa$$

$$\boldsymbol{Pumping\ Power} = \Delta p_{total} \times \dot{V}$$

$$= 31{,}587.653 \times 0.02238881 = 707.21W$$

APPENDIX B

Calculated Thermophysical Properties of Nanofluids

Table B1: Thermophysical Properties for Al_2O_3 Nanofluids

φ	0%	0.5%	1.0%	1.5%	2.0%	2.5%	3.0%
$\mathbf{k_{nf}}$	0.629800	0.656598	0.672144	0.685136	0.696706	0.707322	0.717235
$\mathbf{\mu_{nf}}$	0.000676	0.000688	0.000701	0.000715	0.000730	0.000746	0.000762
$\mathbf{\mu_{nf,wall}}$	0.000706	0.000719	0.000733	0.000748	0.000763	0.000779	0.000796
$\mathbf{\rho}$	992.46	1007.35	1022.24	1037.12	1052.01	1066.90	1081.79
$\mathbf{c_{p,nf}}$	4178.30	4111.04	4045.74	3982.31	3920.68	3860.77	3802.51
$\mathbf{Pr_{nf}}$	4.483	4.308	4.222	4.159	4.109	4.071	4.040

Table B2: Thermophysical Properties for SiO_2 25 nm Nanofluids

φ	0%	0.5%	1.0%	1.5%	2.0%	2.5%	3.0%
$\mathbf{k_{nf}}$	0.629800	0.660541	0.678374	0.693278	0.706551	0.718729	0.730101
$\mathbf{\mu_{nf}}$	0.000676	0.000691	0.000707	0.000724	0.000742	0.000761	0.000781
$\mathbf{\mu_{nf,wall}}$	0.000706	0.000721	0.000738	0.000756	0.000775	0.000795	0.000816
$\mathbf{\rho}$	992.46	998.60	1004.74	1010.87	1017.01	1023.15	1029.29
$\mathbf{c_{p,nf}}$	4178.30	4140.14	4102.44	4065.20	4028.41	3992.06	3956.15
$\mathbf{Pr_{nf}}$	4.483	4.328	4.273	4.243	4.229	4.227	4.234

Table B3: Thermophysical Properties for SiO_2 50 nm Nanofluids

φ	0%	0.5%	1.0%	1.5%	2.0%	2.5%	3.0%
$\mathbf{k_{nf}}$	0.629800	0.653098	0.666612	0.677907	0.687966	0.697196	0.705814
$\mathbf{\mu_{nf}}$	0.000676	0.000688	0.000701	0.000714	0.000728	0.000743	0.000759
$\mathbf{\mu_{nf,wall}}$	0.000706	0.000719	0.000732	0.000746	0.000761	0.000777	0.000793
$\mathbf{\rho}$	992.46	998.60	1004.74	1010.87	1017.01	1023.15	1029.29
$\mathbf{c_{p,nf}}$	4178.30	4140.14	4102.44	4065.20	4028.41	3992.06	3956.15
$\mathbf{Pr_{nf}}$	4.483	4.360	4.312	4.283	4.265	4.257	4.255

Table B4: Thermophysical Properties for SiO_2 100 nm Nanofluids

φ	0%	0.5%	1.0%	1.5%	2.0%	2.5%	3.0%
$\mathbf{k_{nf}}$	0.629800	0.647456	0.657698	0.666259	0.673882	0.680876	0.687408
$\mathbf{\mu_{nf}}$	0.000676	0.000685	0.000696	0.000707	0.000718	0.000730	0.000742
$\mathbf{\mu_{nf,wall}}$	0.000706	0.000716	0.000727	0.000738	0.000750	0.000762	0.000775
$\mathbf{\rho}$	992.46	998.60	1004.74	1010.87	1017.01	1023.15	1029.29
$\mathbf{c_{p,nf}}$	4178.30	4140.14	4102.44	4065.20	4028.41	3992.06	3956.15
$\mathbf{Pr_{nf}}$	4.483	4.383	4.340	4.312	4.292	4.278	4.270

APPENDIX C

Thermal and Hydrodynamic Performance of Existing PHE System Operating With Nanofluids

Table C1: Convection Heat Transfer Coefficient and Heat Capacity Rate at Cold Side

Re	6854.69
Nu	125.24
h_{cold}	12,945.64
C_{cold}	112,802.27

Table C2: Thermal and Hydrodynamic Performances for Al_2O_3 Nanofluids

$\dot{V}$	0.022389				
φ	**0%**	**0.5%**	**1.0%**	**1.5%**	**2.0%**
$\dot{m}_{total}$	22.22	22.55	22.89	23.22	23.55
Re	6433.73	6413.47	6384.78	6350.52	6311.28
Thermal Performance					
Nu	112.09	110.34	109.21	108.21	107.26
h	11,765.86	12,074.80	12,234.51	12,356.24	12,454.66
1/U	0.0001851	0.0001829	0.0001818	0.0001810	0.0001804
U	5403.41	5467.66	5500.17	5524.64	5544.23
C_{hot}	92,841.83	92,717.60	92,593.37	92,469.14	92,344.91
C*	0.823	0.822	0.821	0.820	0.819
NTU	1.112	1.127	1.135	1.142	1.147
ε	0.551	0.555	0.557	0.559	0.561
q_{max}	835,576.43	834,458.37	833,340.30	832,222.24	831,104.18
q	460,743.58	463,250.84	464,414.01	465,236.02	465,851.82
Hydrodynamic Performance					
f	0.2269	0.2270	0.2272	0.2275	0.2278
$\Delta p_{channel}$	37,455.01	38,040.89	38,637.77	39,242.76	39,855.53
ΔP_{port}	3245.57	3294.25	3342.94	3391.62	3440.31
$\Delta p_{elevation}$	9112.93	9249.63	9386.33	9523.03	9659.73
Δp_{total}	31,587.65	32,085.51	32,594.38	33,111.35	33,636.10
PP	707.21	718.36	729.75	741.32	753.07

‘Table C2: Continue’

φ	**2.5%**	**3.0%**
$\dot{m}_{total}$	23.89	24.22
Re	6267.34	6218.86
Thermal Performance		
Nu	106.34	105.43
h	12,535.84	12,603.00
1/U	0.0001798	0.0001794
U	5560.25	5573.43
C_{hot}	92,220.68	92,096.45
C*	0.818	0.816
NTU	1.152	1.156
ε	0.562	0.563
q_{max}	829,986.11	828,868.05
q	466,317.86	466,664.45
Hydrodynamic Performance		
f	0.2281	0.2284
$\Delta p_{channel}$	40,476.14	41,104.82
ΔP_{port}	3489.00	3537.68
$\Delta p_{elevation}$	9796.433	9933.134
Δp_{total}	34,168.70	34,709.37
PP	765.00	777.10

Table C3: Thermal and Hydrodynamic Performances for SiO_2 25 nm Nanofluids

$\dot{V}$	0.022389				
φ	**0%**	**0.5%**	**1.0%**	**1.5%**	**2.0%**
$\dot{m}_{total}$	22.22	22.36	22.50	22.63	22.77
Re	6433.73	6335.44	6229.62	6119.72	6006.51
Thermal Performance					
Nu	112.09	109.46	107.56	105.83	104.18
h	11,765.86	12,049.94	12,161.19	12,228.13	12,267.90
1/U	0.0001851	0.0001831	0.0001823	0.0001819	0.0001816
U	5403.41	5462.55	5485.30	5498.88	5506.91
C_{hot}	92,841.83	92,562.76	92,283.70	92,004.63	91,725.57
C*	0.823	0.821	0.818	0.816	0.813
NTU	1.112	1.128	1.136	1.142	1.147
ε	0.551	0.556	0.558	0.560	0.561
q_{max}	835,576.43	833,064.85	830,553.27	828,041.68	825,530.10
q	460,743.57	462,809.26	463,336.88	463,477.48	463,384.83
Hydrodynamic Performance					
f	0.2269	0.2276	0.2284	0.2292	0.2300
$\Delta p_{channel}$	37,455.01	37,803.02	38,163.90	38,534.15	38,913.38
ΔP_{port}	3245.57	3265.64	3285.71	3305.78	3325.85
$\Delta p_{elevation}$	9112.93	9169.28	9225.64	9282.00	9338.36
Δp_{total}	31,587.65	31,899.38	32,223.97	32,557.93	32,900.87
PP	707.21	714.19	721.46	728.93	736.61

‘Table C3: Continue’

φ	**2.5%**	**3.0%**
$\dot{m}_{total}$	22.91	23.04
Re	5890.33	5771.39
Thermal Performance		
Nu	102.58	101.01
h	12,287.65	12,291.20
1/U	0.0001815	0.0001814
U	5510.88	5511.60
C_{hot}	91,446.50	91,167.44
C*	0.811	0.808
NTU	1.152	1.155
ε	0.563	0.564
q_{max}	823,018.52	820,506.93
q	463,122.48	462,723.97
Hydrodynamic Performance		
f	0.2309	0.2319
$\Delta p_{channel}$	39,301.66	39,699.28
ΔP_{port}	3345.92	3366.00
$\Delta p_{elevation}$	9394.71	9451.07
Δp_{total}	33,252.87	33,614.21
PP	744.49	752.58

Table C4: Thermal and Hydrodynamic Performances for SiO_2 50 nm Nanofluids

$\dot{V}$	0.022389				
φ	**0%**	**0.5%**	**1.0%**	**1.5%**	**2.0%**
$\dot{m}_{total}$	22.22	22.36	22.50	22.63	22.77
Re	6433.73	6361.36	6282.88	6201.09	6116.60
Thermal Performance					
Nu	112.09	110.07	108.61	107.26	105.97
h	11,765.86	11,981.18	12,066.25	12,118.35	12,150.49
1/U	0.0001851	0.0001835	0.0001830	0.0001826	0.0001824
U	5403.41	5448.38	5465.90	5476.57	5483.12
C_{hot}	92,841.83	92,562.76	92,283.70	92,004.63	91,725.57
C*	0.823	0.821	0.818	0.816	0.813
NTU	1.112	1.125	1.132	1.138	1.142
ε	0.551	0.555	0.557	0.559	0.560
q_{max}	835,576.43	833,064.85	830,553.27	828,041.68	825,530.10
q	460,743.57	462,218.93	462,533.46	462,557.49	462,407.27
Hydrodynamic Performance					
f	0.2269	0.2274	0.2280	0.2286	0.2292
$\Delta p_{channel}$	37,455.01	37,772.12	38,098.89	38,432.35	38,772.08
ΔP_{port}	3245.57	3265.64	3285.71	3305.78	3325.85
$\Delta p_{elevation}$	9112.93	9169.28	9225.64	9282.00	9338.36
Δp_{total}	31,587.65	31,868.47	32,158.96	32,456.14	32,759.58
PP	707.21	713.50	720.00	726.65	733.45

‘Table C4: Continue’

φ	**2.5%**	**3.0%**
$\dot{m}_{total}$	22.91	23.04
Re	6029.70	5940.56
Thermal Performance		
Nu	104.72	103.49
h	12,168.06	12,173.96
1/U	0.0001823	0.0001822
U	5486.70	5487.90
C_{hot}	91,446.50	91,167.44
C*	0.811	0.808
NTU	1.147	1.150
ε	0.562	0.563
q_{max}	823,018.52	820,506.93
q	462,131.07	461,754.59
Hydrodynamic Performance		
f	0.2299	0.2305
$\Delta p_{channel}$	39,118.02	39,470.24
ΔP_{port}	3345.92	3366.00
$\Delta p_{elevation}$	9394.71	9451.07
Δp_{total}	33,069.23	33,385.16
PP	740.38	747.45

Table C5: Thermal and Hydrodynamic Performances for SiO_2 100 nm Nanofluids

$\dot{V}$	0.02239				
φ	**0%**	**0.5%**	**1.0%**	**1.5%**	**2.0%**
$\dot{m}_{total}$	22.22	22.36	22.50	22.63	22.77
Re	6433.73	6382.42	6326.14	6267.17	6206.02
Thermal Performance					
Nu	112.09	110.55	109.43	108.39	107.40
h	11,765.86	11,929.77	11,995.34	12,036.28	12,062.42
1/U	0.0001851	0.0001839	0.0001834	0.0001832	0.0001830
U	5403.41	5437.72	5451.31	5459.75	5465.12
C_{hot}	92,841.83	92,562.76	92,283.70	92,004.63	91,725.57
C*	0.823	0.821	0.818	0.816	0.813
NTU	1.112	1.123	1.129	1.134	1.139
ε	0.551	0.554	0.556	0.558	0.559
q_{max}	835,576.43	833,064.85	830,553.27	828,041.68	825,530.10
q	460,743.57	461,774.08	461,927.00	461,861.06	461,664.26
Hydrodynamic Performance					
f	0.2269	0.2273	0.2277	0.2281	0.2285
$\Delta p_{channel}$	37,455.01	37,747.13	38,046.57	38,350.84	38,659.55
ΔP_{port}	3245.57	3265.64	3285.71	3305.78	3325.85
$\Delta p_{elevation}$	9112.93	9169.28	9225.64	9282.00	9338.36
Δp_{total}	31,587.65	31,843.48	32,106.63	32,374.63	32,647.04
PP	707.21	712.94	718.83	724.83	730.93

‘Table C5: Continue’

φ	**2.5%**	**3.0%**
$\dot{m}_{total}$	22.91	23.04
Re	6142.90	6077.97
Thermal Performance		
Nu	106.43	105.48
h	12,077.86	12,084.81
1/U	0.0001829	0.0001828
U	5468.29	5469.71
C_{hot}	91,446.50	91,167.44
C*	0.811	0.808
NTU	1.143	1.147
ε	0.561	0.562
q_{max}	823,018.52	820,506.93
q	461,373.24	461,007.62
Hydrodynamic Performance		
f	0.2290	0.2295
$\Delta p_{channel}$	38,972.56	39,289.88
ΔP_{port}	3345.92	3366.00
$\Delta p_{elevation}$	9394.71	9451.07
Δp_{total}	32,923.77	33,204.81
PP	737.12	743.42

APPENDIX D

Require Heat Transfer Area at a Given NTU Value and Its Corresponding Pressure Drop for Al_2O_3 Nanofluids

Table D1: Effectiveness, Minimum Heat Capacity Rate, Mass Flow Rate and Convective Heat Transfer Coefficient for Cold Side Working Fluid

NTU	**1**	**2**	**3**	**4**	**5**
ε	0.500	0.667	0.750	0.800	0.833
C_{min}	102,222.22	76,666.67	68,148.15	63,888.89	61,333.33
$\dot{m}_{total,\ cold}$	25.68	19.26	17.12	16.05	15.41
$\dot{m}_{channel,\ cold}$	1.027	0.770	0.685	0.642	0.616
Re	6211.77	4658.83	4141.18	3882.36	3727.06
Nu	115.95	92.59	84.44	80.28	77.76
h_{cold}	11,985.80	9570.44	8728.04	8298.33	8037.52

Table D2: Hot Side Channel Mass Flow Rate, $\dot{m}_{channel,\ hot}$

	NTU				
φ	**1**	**2**	**3**	**4**	**5**
0%	0.979	0.734	0.652	0.612	0.587
0.5%	0.995	0.746	0.663	0.622	0.597
1.0%	1.011	0.758	0.674	0.632	0.606
1.5%	1.027	0.770	0.685	0.642	0.616
2.0%	1.043	0.782	0.695	0.652	0.626
2.5%	1.059	0.794	0.706	0.662	0.635
3.0%	1.075	0.806	0.717	0.672	0.645

Table D3: Hot Side Reynolds Number, Re_{nf}

	NTU				
φ	**1**	**2**	**3**	**4**	**5**
0%	7083.76	5312.82	4722.51	4427.35	4250.26
0.5%	7070.92	5303.19	4713.95	4419.33	4242.55
1.0%	7048.74	5286.55	4699.16	4405.46	4229.24
1.5%	7020.33	5265.25	4680.22	4387.71	4212.20
2.0%	6986.34	5239.75	4657.56	4366.46	4191.80
2.5%	6947.05	5210.28	4631.36	4341.90	4168.23
3.0%	6902.61	5176.96	4601.74	4314.13	4141.57

Table D4: Hot Side Nusselt Number, Nu_{nf}

	NTU				
φ	**1**	**2**	**3**	**4**	**5**
0%	120.86	96.50	88.01	83.68	81.05
0.5%	119.09	95.09	86.72	82.45	79.86
1.0%	118.00	94.22	85.93	81.70	79.13
1.5%	117.04	93.45	85.23	81.03	78.48
2.0%	116.13	92.73	84.57	80.40	77.88
2.5%	115.26	92.03	83.93	79.80	77.29
3.0%	114.39	91.34	83.30	79.20	76.71

Table D5: Hot Side Convective Heat Transfer Coefficient, h_{nf}

	NTU				
φ	**1**	**2**	**3**	**4**	**5**
0%	12,685.97	10,129.51	9237.90	8783.09	8507.05
0.5%	13,032.71	10,406.37	9490.40	9023.16	8739.57
1.0%	13,218.95	10,555.08	9626.02	9152.10	8864.46
1.5%	13,364.50	10,671.30	9732.01	9252.87	8962.06
2.0%	13,485.13	10,767.62	9819.85	9336.38	9042.95
2.5%	13,587.32	10,849.22	9894.27	9407.14	9111.48
3.0%	13,674.53	10,918.85	9957.77	9467.52	9169.96

Table D6: Overall Heat Transfer Coefficient, U

	NTU				
φ	**1**	**2**	**3**	**4**	**5**
0%	5402.77	4423.98	4070.77	3888.14	3776.48
0.5%	5464.69	4475.99	4119.06	3934.48	3821.61
1.0%	5497.16	4503.28	4144.40	3958.80	3845.30
1.5%	5522.17	4524.30	4163.93	3977.54	3863.56
2.0%	5542.66	4541.52	4179.92	3992.89	3878.51
2.5%	5559.85	4555.97	4193.35	4005.78	3891.06
3.0%	5574.39	4568.21	4204.71	4016.69	3901.69

Table D7: Heat Transfer Area Required, $A_{required}$

	NTU				
φ	**1**	**2**	**3**	**4**	**5**
0%	18.92	34.66	50.22	65.73	81.20
0.5%	18.71	34.26	49.63	64.95	80.25
1.0%	18.60	34.05	49.33	64.55	79.75
1.5%	18.51	33.89	49.10	64.25	79.37
2.0%	18.44	33.76	48.91	64.00	79.07
2.5%	18.39	33.66	48.75	63.80	78.81
3.0%	18.34	33.57	48.62	63.62	78.60

Table D8: Friction Factor for Hot Side Fluid, f

	NTU				
φ	**1**	**2**	**3**	**4**	**5**
0%	0.2226	0.2358	0.2414	0.2445	0.2465
0.5%	0.2226	0.2358	0.2415	0.2446	0.2466
1.0%	0.2228	0.2360	0.2416	0.2448	0.2468
1.5%	0.2230	0.2362	0.2418	0.2450	0.2470
2.0%	0.2232	0.2364	0.2421	0.2452	0.2472
2.5%	0.2234	0.2367	0.2423	0.2455	0.2475
3.0%	0.2237	0.2370	0.2426	0.2458	0.2478

Table D9: Estimated Port to Port Vertical Length, L

	NTU				
φ	**1**	**2**	**3**	**4**	**5**
0%	0.944	1.730	2.507	3.281	4.054
0.5%	0.934	1.710	2.478	3.242	4.006
1.0%	0.928	1.700	2.462	3.222	3.981
1.5%	0.924	1.692	2.451	3.207	3.962
2.0%	0.921	1.685	2.442	3.195	3.947
2.5%	0.918	1.680	2.434	3.185	3.934
3.0%	0.915	1.675	2.427	3.176	3.923

Table D10: Channel Pressure Drop, $\Delta p_{channel}$

	NTU				
φ	**1**	**2**	**3**	**4**	**5**
0%	44,941.23	49,055.16	57,504.22	67,003.88	76,918.29
0.5%	45,235.90	49,362.38	57,858.25	67,412.72	77,385.04
1.0%	45,784.60	49,953.48	58,547.84	68,214.24	78,303.76
1.5%	46,402.87	50,622.06	59,328.93	69,122.76	79,345.59
2.0%	47,067.00	51,341.61	60,170.13	70,101.56	80,468.26
2.5%	47,767.72	52,101.75	61,059.19	71,136.28	81,655.24
3.0%	48,500.59	52,897.48	61,990.18	72,220.00	82,898.56

Table D11: Port Pressure Drop, Δp_{port}

	NTU				
φ	**1**	**2**	**3**	**4**	**5**
0%	3934.54	2213.18	1748.68	1536.93	1416.43
0.5%	4004.27	2252.40	1779.67	1564.17	1441.54
1.0%	4074.36	2291.83	1810.83	1591.55	1466.77
1.5%	4144.81	2331.46	1842.14	1619.07	1492.13
2.0%	4215.63	2371.29	1873.61	1646.73	1517.63
2.5%	4286.81	2411.33	1905.25	1674.54	1543.25
3.0%	4358.37	2451.58	1937.05	1702.49	1569.01

Table D12: Pressure Drop Due to Elevation Change, $\Delta p_{elevation}$

	NTU				
φ	**1**	**2**	**3**	**4**	**5**
0%	9195.21	16,844.43	24,407.97	31,943.01	39,465.02
0.5%	9227.39	16,898.45	24,483.66	32,040.32	39,583.92
1.0%	9308.45	17,044.28	24,693.58	32,314.10	39,921.47
1.5%	9401.24	17,212.16	24,935.74	32,630.28	40,311.53
2.0%	9500.95	17,393.02	25,196.88	32,971.41	40,732.52
2.5%	9605.62	17,583.20	25,471.65	33,330.45	41,175.69
3.0%	9714.24	17,780.82	25,757.28	33,703.77	41,636.56

Table D13: Total Pressure Drop, Δp_{total}

	NTU				
φ	**1**	**2**	**3**	**4**	**5**
0%	39,680.56	34,423.91	34,844.93	36,597.80	38,869.71
0.5%	40,012.78	34,716.33	35,154.26	36,936.57	39,242.65
1.0%	40,550.51	35,201.03	35,665.09	37,491.68	39,849.05
1.5%	41,146.44	35,741.36	36,235.33	38,111.55	40,526.19
2.0%	41,781.68	36,319.88	36,846.86	38,776.88	41,253.37
2.5%	42,448.92	36,929.87	37,492.79	39,480.37	42,022.80
3.0%	43,144.72	37,568.24	38,169.95	40,218.72	42,831.01

APPENDIX E

Require Heat Transfer Area at a Given NTU Value and Its Corresponding Pressure Drop for SiO_2-25nm Nanofluids

Table E1: Effectiveness, Minimum Heat Capacity Rate, Mass Flow Rate and Convective Heat Transfer Coefficient for Cold Side Working Fluid

NTU	**1**	**2**	**3**	**4**	**5**
ε	0.500	0.667	0.750	0.800	0.833
C_{min}	102,222.22	76,666.67	68,148.15	63,888.89	61,333.33
$\dot{m}_{total,\ cold}$	25.68	19.26	17.12	16.05	15.41
$\dot{m}_{channel,\ cold}$	1.027	0.770	0.685	0.642	0.616
Re	6211.77	4658.83	4141.18	3882.36	3727.06
Nu	115.95	92.59	84.44	80.28	77.76
h_{cold}	11,985.80	9570.44	8728.04	8298.33	8037.52

Table E2: Hot Side Channel Mass Flow Rate, $\dot{m}_{channel,\ hot}$

	NTU				
φ	**1**	**2**	**3**	**4**	**5**
0%	0.979	0.734	0.652	0.612	0.587
0.5%	0.988	0.741	0.658	0.617	0.593
1.0%	0.997	0.748	0.664	0.623	0.598
1.5%	1.006	0.754	0.671	0.629	0.603
2.0%	1.015	0.761	0.677	0.634	0.609
2.5%	1.024	0.768	0.683	0.640	0.615
3.0%	1.034	0.775	0.689	0.646	0.620

Table E3: Hot Side Reynolds Number, Re_{nf}

	NTU				
φ	**1**	**2**	**3**	**4**	**5**
0%	7083.76	5312.82	4722.51	4427.35	4250.26
0.5%	6996.58	5247.43	4664.38	4372.86	4197.95
1.0%	6900.52	5175.39	4600.34	4312.82	4140.31
1.5%	6799.35	5099.51	4532.90	4249.59	4079.61
2.0%	6693.86	5020.40	4462.58	4183.66	4016.32
2.5%	6584.42	4938.32	4389.61	4115.26	3950.65
3.0%	6471.21	4853.41	4314.14	4044.51	3882.73

Table E4: Hot Side Nusselt Number, Nu_{nf}

	NTU				
φ	**1**	**2**	**3**	**4**	**5**
0%	120.86	96.50	88.01	83.68	81.05
0.5%	118.29	94.45	86.14	81.90	79.33
1.0%	116.52	93.04	84.85	80.67	78.14
1.5%	114.92	91.76	83.68	79.56	77.06
2.0%	113.39	90.54	82.57	78.51	76.04
2.5%	111.92	89.36	81.50	77.49	75.05
3.0%	110.47	88.21	80.44	76.48	74.08

Table E5: Hot Side Convective Heat Transfer Coefficient, h_{nf}

	NTU				
φ	**1**	**2**	**3**	**4**	**5**
0%	12,685.97	10,129.51	9237.90	8783.09	8507.05
0.5%	13,022.89	10,398.53	9483.25	9016.36	8732.98
1.0%	13,174.22	10,519.36	9593.44	9121.13	8834.46
1.5%	13,278.14	10,602.35	9669.12	9193.08	8904.15
2.0%	13,353.02	10,662.14	9723.65	9244.92	8954.36
2.5%	13,406.44	10,704.79	9762.55	9281.91	8990.18
3.0%	13,442.41	10,733.51	9788.74	9306.81	9014.30

Table E6: Overall Heat Transfer Coefficient, U

	NTU				
φ	**1**	**2**	**3**	**4**	**5**
0%	5402.77	4423.98	4070.77	3888.14	3776.48
0.5%	5462.96	4474.54	4117.71	3933.19	3820.35
1.0%	5489.41	4496.76	4138.35	3953.00	3839.65
1.5%	5507.37	4511.86	4152.37	3966.45	3852.75
2.0%	5520.21	4522.65	4162.39	3976.07	3862.12
2.5%	5529.32	4530.31	4169.51	3982.89	3868.77
3.0%	5535.43	4535.44	4174.28	3987.47	3873.23

Table E7: Heat Transfer Area Required, $A_{required}$

	NTU				
φ	**1**	**2**	**3**	**4**	**5**
0%	18.92	34.66	50.22	65.73	81.20
0.5%	18.71	34.27	49.65	64.97	80.27
1.0%	18.62	34.10	49.40	64.65	79.87
1.5%	18.56	33.98	49.24	64.43	79.60
2.0%	18.52	33.90	49.12	64.27	79.40
2.5%	18.49	33.85	49.03	64.16	79.27
3.0%	18.47	33.81	48.98	64.09	79.18

Table E8: Friction Factor for Hot Side fluid, f

	NTU				
φ	**1**	**2**	**3**	**4**	**5**
0%	0.2226	0.2358	0.2414	0.2445	0.2465
0.5%	0.2231	0.2363	0.2420	0.2451	0.2471
1.0%	0.2237	0.2370	0.2427	0.2458	0.2478
1.5%	0.2244	0.2377	0.2434	0.2465	0.2486
2.0%	0.2251	0.2384	0.2441	0.2473	0.2493
2.5%	0.2258	0.2392	0.2449	0.2481	0.2502
3.0%	0.2266	0.2401	0.2458	0.2490	0.2510

Table E9: Estimated Port to Port Vertical Length, L

	NTU				
φ	**1**	**2**	**3**	**4**	**5**
0%	0.944	1.730	2.507	3.281	4.054
0.5%	0.934	1.711	2.478	3.243	4.007
1.0%	0.930	1.702	2.466	3.227	3.987
1.5%	0.927	1.696	2.458	3.216	3.973
2.0%	0.924	1.692	2.452	3.208	3.964
2.5%	0.923	1.690	2.448	3.203	3.957
3.0%	0.922	1.688	2.445	3.199	3.952

Table E10: Channel Pressure Drop, $\Delta p_{channel}$

	NTU				
φ	**1**	**2**	**3**	**4**	**5**
0%	44,941.23	49,055.16	57,504.22	67,003.88	76,918.29
0.5%	45,102.72	49,217.45	57,688.55	67,215.10	77,158.26
1.0%	45,560.80	49,711.12	58,264.55	67,884.64	77,925.74
1.5%	46,103.39	50,298.86	58,951.62	68,684.07	78,842.64
2.0%	46,703.46	50,950.45	59,713.99	69,571.51	79,860.79
2.5%	47,350.73	51,654.36	60,538.04	70,531.02	80,961.81
3.0%	48,040.52	52,405.34	61,417.53	71,555.31	82,137.30

Table E11: Port Pressure Drop, Δp_{port}

	NTU				
φ	**1**	**2**	**3**	**4**	**5**
0%	3934.54	2213.18	1748.68	1536.93	1416.43
0.5%	3982.78	2240.31	1770.12	1555.77	1433.80
1.0%	4031.53	2267.73	1791.79	1574.82	1451.35
1.5%	4080.80	2295.45	1813.69	1594.06	1469.09
2.0%	4130.60	2323.46	1835.82	1613.51	1487.01
2.5%	4180.93	2351.77	1858.19	1633.17	1505.13
3.0%	4231.80	2380.39	1880.80	1653.05	1523.45

Table E12: Pressure Drop Due to Elevation Change, $\Delta p_{elevation}$

	NTU				
φ	**1**	**2**	**3**	**4**	**5**
0%	9195.21	16,844.43	24,407.97	31,943.01	39,465.02
0.5%	9150.13	16,757.10	24,278.93	31,772.45	39,253.03
1.0%	9162.01	16,776.76	24,306.32	31,807.56	39,295.84
1.5%	9187.92	16,822.77	24,372.24	31,893.31	39,401.39
2.0%	9222.20	16,884.52	24,461.17	32,009.32	39,544.44
2.5%	9262.58	16,957.71	24,566.82	32,147.32	39,714.73
3.0%	9307.86	17,040.12	24,685.95	32,303.03	39,906.96

Table E13: Total Pressure Drop, Δp_{total}

	NTU				
φ	**1**	**2**	**3**	**4**	**5**
0%	39,680.56	34,423.91	34,844.93	36,597.80	38,869.71
0.5%	39,935.37	34,700.67	35,179.74	36,998.42	39,339.03
1.0%	40,430.32	35,202.09	35,750.02	37,651.90	40,081.25
1.5%	40,996.27	35,771.54	36,393.07	38,384.82	40,910.34
2.0%	41,611.85	36,389.39	37,088.65	39,175.71	41,803.36
2.5%	42,269.08	37,048.42	37,829.41	40,016.88	42,752.22
3.0%	42,964.46	37,745.60	38,612.38	40,905.32	43,753.79

APPENDIX F

Require Heat Transfer Area at a Given NTU Value and Its Corresponding Pressure Drop for SiO_2-50nm Nanofluids

Table F1: Effectiveness, Minimum Heat Capacity Rate, Mass Flow Rate and Convective Heat Transfer Coefficient for Cold Side Working Fluid

NTU	**1**	**2**	**3**	**4**	**5**
ε	0.500	0.667	0.750	0.800	0.833
$\mathbf{C_{min}}$	102,222.22	76,666.67	68,148.15	63,888.89	61,333.33
$\mathbf{\dot{m}_{total,\ Cold}}$	25.68	19.26	17.12	16.05	15.41
$\mathbf{\dot{m}_{channel,\ Cold}}$	1.027	0.770	0.685	0.642	0.616
Re	6211.77	4658.83	4141.18	3882.36	3727.06
Nu	115.95	92.59	84.44	80.28	77.76
$\mathbf{h_{Cold}}$	11,985.80	9570.44	8728.04	8298.33	8037.52

Table F2: Hot Side Channel Mass Flow Rate, $\dot{m}_{channel,\ Hot}$

	NTU				
φ	**1**	**2**	**3**	**4**	**5**
0%	0.979	0.734	0.652	0.612	0.587
0.5%	0.988	0.741	0.658	0.617	0.593
1.0%	0.997	0.748	0.664	0.623	0.598
1.5%	1.006	0.754	0.671	0.629	0.603
2.0%	1.015	0.761	0.677	0.634	0.609
2.5%	1.024	0.768	0.683	0.640	0.615
3.0%	1.034	0.775	0.689	0.646	0.620

Table F3: Hot Side Reynolds Number, Re_{nf}

	NTU				
φ	**1**	**2**	**3**	**4**	**5**
0%	7083.76	5312.82	4722.51	4427.35	4250.26
0.5%	7025.21	5268.90	4683.47	4390.75	4215.12
1.0%	6959.51	5219.63	4639.68	4349.70	4175.71
1.5%	6889.75	5167.31	4593.17	4306.09	4133.85
2.0%	6816.55	5112.41	4544.37	4260.34	4089.93
2.5%	6740.22	5055.16	4493.48	4212.63	4044.13
3.0%	6660.90	4995.68	4440.60	4163.06	3996.54

Table F4: Hot Side Nusselt Number, Nu_{nf}

	NTU				
φ	**1**	**2**	**3**	**4**	**5**
0%	120.86	96.50	88.01	83.68	81.05
0.5%	118.96	94.99	86.63	82.36	79.77
1.0%	117.65	93.94	85.67	81.46	78.90
1.5%	116.47	93.00	84.81	80.64	78.10
2.0%	115.34	92.10	83.99	79.86	77.35
2.5%	114.25	91.23	83.20	79.10	76.62
3.0%	113.18	90.37	82.42	78.36	75.90

Table F5: Hot Side Convective Heat Transfer Coefficient, h_{nf}

	NTU				
φ	**1**	**2**	**3**	**4**	**5**
0%	12,685.97	10,129.51	9237.90	8783.09	8507.05
0.5%	12,948.59	10,339.20	9429.14	8964.91	8683.15
1.0%	13,071.36	10,437.23	9518.54	9049.91	8765.48
1.5%	13,158.95	10,507.17	9582.32	9110.56	8824.22
2.0%	13,225.23	10,560.09	9630.59	9156.45	8868.67
2.5%	13,275.96	10,600.60	9667.53	9191.57	8902.68
3.0%	13,314.19	10,631.13	9695.37	9218.04	8928.32

Table F6: Overall Heat Transfer Coefficient, U

	NTU				
φ	**1**	**2**	**3**	**4**	**5**
0%	5402.77	4423.98	4070.77	3888.14	3776.48
0.5%	5449.84	4463.51	4107.48	3923.37	3810.79
1.0%	5471.47	4481.69	4124.35	3939.56	3826.56
1.5%	5486.76	4494.53	4136.28	3951.01	3837.71
2.0%	5498.25	4504.19	4145.25	3959.61	3846.09
2.5%	5507.00	4511.54	4152.08	3966.17	3852.48
3.0%	5513.56	4517.06	4157.20	3971.09	3857.27

Table F7: Heat Transfer Area Required, $A_{required}$

	NTU				
φ	**1**	**2**	**3**	**4**	**5**
0%	18.92	34.66	50.22	65.73	81.20
0.5%	18.76	34.35	49.77	65.14	80.47
1.0%	18.68	34.21	49.57	64.87	80.14
1.5%	18.63	34.12	49.43	64.68	79.91
2.0%	18.59	34.04	49.32	64.54	79.73
2.5%	18.56	33.99	49.24	64.43	79.60
3.0%	18.54	33.95	49.18	64.35	79.50

Table F8: Friction Factor for Hot Side Fluid, f

	NTU				
φ	**1**	**2**	**3**	**4**	**5**
0%	0.2226	0.2358	0.2414	0.2445	0.2465
0.5%	0.2229	0.2361	0.2418	0.2449	0.2469
1.0%	0.2233	0.2366	0.2422	0.2454	0.2474
1.5%	0.2238	0.2371	0.2427	0.2459	0.2479
2.0%	0.2243	0.2376	0.2432	0.2464	0.2484
2.5%	0.2248	0.2381	0.2438	0.2470	0.2490
3.0%	0.2253	0.2387	0.2444	0.2476	0.2496

Table F9: Estimated Port to Port Vertical Length, L

	NTU				
φ	**1**	**2**	**3**	**4**	**5**
0%	0.944	1.730	2.507	3.281	4.054
0.5%	0.936	1.715	2.485	3.251	4.017
1.0%	0.933	1.708	2.474	3.238	4.000
1.5%	0.930	1.703	2.467	3.229	3.989
2.0%	0.928	1.699	2.462	3.222	3.980
2.5%	0.927	1.697	2.458	3.216	3.974
3.0%	0.925	1.694	2.455	3.212	3.969

Table F10: Channel Pressure Drop, $\Delta p_{channel}$

	NTU				
φ	**1**	**2**	**3**	**4**	**5**
0%	44,941.23	49,055.16	57,504.22	67,003.88	76,918.29
0.5%	45,174.34	49,298.65	57,785.02	67,328.28	77,288.73
1.0%	45,632.32	49,793.36	58,362.74	68,000.11	78,059.04
1.5%	46,154.35	50,359.37	59,024.61	68,770.35	78,942.57
2.0%	46,719.77	50,973.53	59,743.28	69,606.98	79,902.45
2.5%	47,320.52	51,626.84	60,508.09	70,497.52	80,924.33
3.0%	47,952.76	52,315.00	61,313.94	71,436.00	82,001.32

Table F11: Port Pressure Drop, Δp_{port}

	NTU				
φ	**1**	**2**	**3**	**4**	**5**
0%	3934.54	2213.18	1748.68	1536.93	1416.43
0.5%	3982.78	2240.31	1770.12	1555.77	1433.80
1.0%	4031.53	2267.73	1791.79	1574.82	1451.35
1.5%	4080.80	2295.45	1813.69	1594.06	1469.09
2.0%	4130.60	2323.46	1835.82	1613.51	1487.01
2.5%	4180.93	2351.77	1858.19	1633.17	1505.13
3.0%	4231.80	2380.39	1880.80	1653.05	1523.45

Table F12: Pressure Drop Due to Elevation Change, $\Delta p_{elevation}$

	NTU				
φ	**1**	**2**	**3**	**4**	**5**
0%	9195.21	16,844.43	24,407.97	31,943.01	39,465.02
0.5%	9172.16	16,798.48	24,339.43	31,851.99	39,351.57
1.0%	9192.05	16,833.19	24,388.83	31,916.03	39,430.23
1.5%	9222.44	16,887.62	24,467.05	32,017.96	39,555.83
2.0%	9259.04	16,953.73	24,562.35	32,142.34	39,709.25
2.5%	9300.13	17,028.25	24,669.94	32,282.89	39,882.70
3.0%	9344.77	17,109.46	24,787.32	32,436.31	40,072.09

Table F13: Total Pressure Drop, Δp_{total}

	NTU				
φ	**1**	**2**	**3**	**4**	**5**
0%	39,680.56	34,423.91	34,844.93	36,597.80	38,869.71
0.5%	39,984.96	34,740.49	35,215.71	37,032.06	39,370.96
1.0%	40,471.80	35,227.91	35,765.70	37,658.90	40,080.16
1.5%	41,012.72	35,767.20	36,371.25	38,346.46	40,855.83
2.0%	41,591.32	36,343.26	37,016.75	39,078.15	41,680.21
2.5%	42,201.32	36,950.37	37,696.34	39,847.80	42,546.76
3.0%	42,839.78	37,585.92	38,407.42	40,652.73	43,452.67

APPENDIX G

Require Heat Transfer Area at a Given NTU Value and Its Corresponding Pressure Drop for SiO_2-100nm Nanofluids

Table G1: Effectiveness, Minimum Heat Capacity Rate, Mass Flow Rate and Convective Heat Transfer Coefficient for Cold Side Working Fluid

NTU	**1**	**2**	**3**	**4**	**5**
ε	0.500	0.667	0.750	0.800	0.833
$\mathbf{C_{min}}$	102,222.22	76,666.67	68,148.15	63,888.89	61,333.33
$\mathbf{\dot{m}_{total,\ cold}}$	25.68	19.26	17.12	16.05	15.41
$\mathbf{\dot{m}_{channel,\ cold}}$	1.027	0.770	0.685	0.642	0.616
Re	6211.77	4658.83	4141.18	3882.36	3727.06
Nu	115.95	92.59	84.44	80.28	77.76
$\mathbf{h_{cold}}$	11,985.80	9570.44	8728.04	8298.33	8037.52

Table G2: Hot Side Channel Mass Flow Rate, $\dot{m}_{channel,\ Hot}$

	NTU				
φ	**1**	**2**	**3**	**4**	**5**
0%	0.979	0.734	0.652	0.612	0.587
0.5%	0.988	0.741	0.658	0.617	0.593
1.0%	0.997	0.748	0.664	0.623	0.598
1.5%	1.006	0.754	0.671	0.629	0.603
2.0%	1.015	0.761	0.677	0.634	0.609
2.5%	1.024	0.768	0.683	0.640	0.615
3.0%	1.034	0.775	0.689	0.646	0.620

Table G3: Hot Side Reynolds Number, Re_{nf}

	NTU				
φ	**1**	**2**	**3**	**4**	**5**
0%	7083.76	5312.82	4722.51	4427.35	4250.26
0.5%	7048.46	5286.34	4698.97	4405.29	4229.08
1.0%	7007.43	5255.58	4671.62	4379.65	4204.46
1.5%	6963.18	5222.38	4642.12	4351.98	4177.91
2.0%	6916.21	5187.15	4610.80	4322.63	4149.72
2.5%	6866.76	5150.07	4577.84	4291.73	4120.06
3.0%	6814.97	5111.23	4543.32	4259.36	4088.98

Table G4: Hot Side Nusselt Number, Nu_{nf}

	NTU				
φ	**1**	**2**	**3**	**4**	**5**
0%	120.86	96.50	88.01	83.68	81.05
0.5%	119.48	95.40	87.01	82.72	80.12
1.0%	118.55	94.66	86.32	82.07	79.50
1.5%	117.70	93.98	85.71	81.49	78.93
2.0%	116.90	93.34	85.13	80.93	78.39
2.5%	116.12	92.72	84.56	80.40	77.87
3.0%	115.36	92.11	84.01	79.87	77.36

Table G5: Hot Side Convective Heat Transfer Coefficient, h_{nf}

	NTU				
φ	**1**	**2**	**3**	**4**	**5**
0%	12,685.97	10,129.51	9237.90	8783.09	8507.05
0.5%	12,893.03	10,294.84	9388.68	8926.45	8645.90
1.0%	12,994.54	10,375.89	9462.60	8996.73	8713.97
1.5%	13,069.82	10,436.00	9517.42	9048.85	8764.45
2.0%	13,129.37	10,483.55	9560.79	9090.08	8804.39
2.5%	13,177.55	10,522.03	9595.87	9123.44	8836.70
3.0%	13,216.69	10,553.28	9624.37	9150.54	8862.94

Table G6: Overall Heat Transfer Coefficient, U

	NTU				
φ	**1**	**2**	**3**	**4**	**5**
0%	5402.77	4423.98	4070.77	3888.14	3776.48
0.5%	5439.97	4455.22	4099.78	3915.98	3803.59
1.0%	5457.96	4470.34	4113.81	3929.45	3816.71
1.5%	5471.20	4481.46	4124.14	3939.36	3826.36
2.0%	5481.61	4490.20	4132.26	3947.15	3833.96
2.5%	5489.99	4497.25	4138.80	3953.43	3840.07
3.0%	5496.77	4502.95	4144.10	3958.51	3845.02

Table G7: Heat Transfer Area Required, $A_{required}$

	NTU				
φ	**1**	**2**	**3**	**4**	**5**
0%	18.92	34.66	50.22	65.73	81.20
0.5%	18.79	34.42	49.87	65.26	80.63
1.0%	18.73	34.30	49.70	65.04	80.35
1.5%	18.68	34.22	49.57	64.87	80.15
2.0%	18.65	34.15	49.48	64.74	79.99
2.5%	18.62	34.09	49.40	64.64	79.86
3.0%	18.60	34.05	49.33	64.56	79.76

Table G8: Friction Factor for Hot Side Fluid, f

	NTU				
φ	**1**	**2**	**3**	**4**	**5**
0%	0.2226	0.2358	0.2414	0.2445	0.2465
0.5%	0.2228	0.2360	0.2416	0.2448	0.2468
1.0%	0.2230	0.2363	0.2419	0.2451	0.2471
1.5%	0.2233	0.2366	0.2422	0.2454	0.2474
2.0%	0.2236	0.2369	0.2425	0.2457	0.2477
2.5%	0.2239	0.2372	0.2429	0.2461	0.2481
3.0%	0.2243	0.2376	0.2433	0.2464	0.2484

Table G9: Estimated Port to Port Vertical Length, L

	NTU				
φ	**1**	**2**	**3**	**4**	**5**
0%	0.944	1.730	2.507	3.281	4.054
0.5%	0.938	1.718	2.489	3.258	4.025
1.0%	0.935	1.712	2.481	3.246	4.011
1.5%	0.933	1.708	2.475	3.238	4.001
2.0%	0.931	1.705	2.470	3.232	3.993
2.5%	0.929	1.702	2.466	3.227	3.986
3.0%	0.928	1.700	2.463	3.223	3.981

Table G10: Channel Pressure Drop, $\Delta p_{channel}$

	NTU				
φ	**1**	**2**	**3**	**4**	**5**
0%	44,941.23	49,055.16	57,504.22	67,003.88	76,918.29
0.5%	45,226.33	49,357.69	57,855.19	67,410.62	77,383.66
1.0%	45,682.41	49,851.20	58,431.87	68,081.47	78,153.00
1.5%	46,187.42	50,399.14	59,072.80	68,827.44	79,008.76
2.0%	46,725.56	50,983.85	59,757.07	69,624.07	79,922.79
2.5%	47,290.60	51,598.34	60,476.44	70,461.70	80,883.95
3.0%	47,879.46	52,239.18	61,226.83	71,335.56	81,886.77

Table G11: Port Pressure Drop, Δp_{port}

	NTU				
φ	**1**	**2**	**3**	**4**	**5**
0%	3934.54	2213.18	1748.68	1536.93	1416.43
0.5%	3982.78	2240.31	1770.12	1555.77	1433.80
1.0%	4031.53	2267.73	1791.79	1574.82	1451.35
1.5%	4080.80	2295.45	1813.69	1594.06	1469.09
2.0%	4130.60	2323.46	1835.82	1613.51	1487.01
2.5%	4180.93	2351.77	1858.19	1633.17	1505.13
3.0%	4231.80	2380.39	1880.80	1653.05	1523.45

Table G12: Pressure Drop Due to Elevation Change, $\Delta p_{elevation}$

	NTU				
φ	**1**	**2**	**3**	**4**	**5**
0%	9195.21	16,844.43	24,407.97	31,943.01	39,465.02
0.5%	9188.80	16,829.73	24,385.12	31,912.06	39,425.99
1.0%	9214.80	16,875.92	24,451.30	31,998.16	39,531.99
1.5%	9248.66	16,936.88	24,539.07	32,112.64	39,673.14
2.0%	9287.15	17,006.52	24,639.54	32,243.83	39,834.98
2.5%	9328.93	17,082.36	24,749.06	32,386.92	40,011.58
3.0%	9373.32	17,163.09	24,865.73	32,539.39	40,199.80

Table G13: Total Pressure Drop, Δp_{total}

	NTU				
φ	**1**	**2**	**3**	**4**	**5**
0%	39,680.56	34,423.91	34,844.93	36,597.80	38,869.71
0.5%	40,020.31	34,768.27	35,240.19	37,054.34	39,391.47
1.0%	40,499.14	35,243.01	35,772.36	37,658.12	40,072.37
1.5%	41,019.56	35,757.72	36,347.42	38,308.86	40,804.71
2.0%	41,569.01	36,300.79	36,953.36	38,993.76	41,574.82
2.5%	42,142.59	36,867.75	37,585.57	39,707.96	42,377.51
3.0%	42,737.94	37,456.47	38,241.90	40,449.22	43,210.41